The Elastic Properties of Interpenetrating Phase Composites Reinforced by Regular Lattice and Voronoi Fibre Networks

by

Zhengyang Zhang

Thesis submitted for the degree of Doctor of Philosophy

School of Engineering

Cardiff University

2019

Acknowledgement

I would like to express my sincere appreciation to my supervisors, Dr. Hanxing Zhu and Prof. Yacine Rezgui for their patience and enthusiasm to guide my research over the past four years. Many thanks to Dr. Hanxing Zhu for his detailed guidance and fresh inspirations to my work. His analogy between research and mining gave the first impression of academic research and have been leading the way of my study ever since. The patience and encouragement that he showed to my work during the past four years makes a big difference to my work. His devotion as well as attitude toward work and research have also become my goal to pursuit.

I would like to thank Prof. David Kennedy who has been internal examiner of my annual reviews during my PhD study. I would like to thank Prof. Ru Yuan and Prof. Sanmin Wang from Northwestern Polytechnical University for recommending me to study in Cardiff University. I would like to thank Dr. Yanhui Ma and Dr. Xiude Lin who have shared valuable ideas in the application of boundary conditions in my research. Great appreciation to my colleagues in our team for their helpful discussions and continuous support in my research.

I am thankful to China Scholarship Council and Cardiff University School of Engineering for the sponsorship who sponsored me to finish my research.

Finally, I would like to thank my family for encouraging me to pursue a doctorate. Love you all.

Abstract

Interpenetrating phase composites (IPCs) are a class of composites in which two or more constituent phases are continuous in their geometry and each phase is a self-connected network in its architecture or microstructure. The reinforcement phase of the IPCs has a cellular network structure, and the lattice structured reinforcement IPCs can be fabricated by different methods. Although the prediction of the mechanical properties of IPCs has long been a research hotspot in composite materials, the effects of the geometrical structures and mechanical properties of the constituent materials on the mechanical properties of the composite are less known. This thesis provides a numerical approach to predict the elastic properties of IPCs reinforced by different types of lattice structures and Voronoi fibre networks, and by different combinations of the constituent materials using finite element method (FEM).

Four different types of regular lattice reinforced IPCs are constructed via Boolean operations and modelled using solid elements. The simulation shows that the Young's modulus of the composites strongly depends on the Poisson's ratios of the two constituent materials, and it can exceed the Voigt limit when the Poisson's ratio of the matrix is negative.

In order to achieve a negative Poisson's ratio for the composite materials, three types of auxetic lattice structured IPCs are constructed. The simulation results of the IPCs reinforced by auxetic lattice structures shows that they all could have either a positive, or a negative, or a zero Poisson's ratio. The magnitude of the Poisson's ratio depends on the combination between the fibre angle, the type of the fibre-network, the fibre volume fraction, and the mechanical properties of the component materials.

To represent the reinforcement of random fibre network structure, IPCs reinforced by a 3D Voronoi open-cell foam are constructed, and their elastic properties are simulated. Their results show elastic properties similar to those of IPCs reinforced by regular lattice structures. Different types of structures are compared to find which is the best in

given conditions. This study could provide a good guide for designing the architecture and microstructure of interpenetrating phase composites.

Table of Contents

Table of Contents

Table of Contents

List of Figures

List of Figures

List of Figures

List of Figures

List of Figures

List of Tables

List of Tables

List of abbreviations

ASC	Automatic searching & coupling
BCC	Body-centred cubic
C^4	Co-continuous ceramic-metal composite
TPM	Composite spheres model
CAD	Computer aided design
CLP	Crossed layers of parallels
EMA	Effective medium approximation
FCC	Face-centred cubic
FRC	Fibre reinforced composite
FE	Finite element
GFRP	Glass-fibre reinforced plastic
GRP	Glass-reinforced plastic
H–T	Halpin–tsai
HS	Hashin-shtrikman
IWP	I-graph and wrapped package-graph

List of abbreviations

IPC	Interpenetrating phase composite
IPN	Interpenetrating polymer network
MFSS	Metal fibre sintered sheets
MMC	Metal matrix composite
NFC	Natural fibre composites
PBC	Periodic boundary condition
PP	Polypropylene
PTFE	Polytetrafluoroethylene
PU	Polyurethane
RSA	Random sequential adsorption
RMP	Reactive metal penetration
RVE	Representative volume element
RAE	Royal aircraft establishment
SEM	Scanning electron micrograph
SEBM	Selective electron-beam melting
STIT	Stable under iterations
TPMS	Triply periodic minimal surfaces

Nomenclature

A	Area of cross section
cor	Coefficient of regularity
$d, d_I, d_{II}, d_{III}, d_f, d_{fe}$	Fibre diameter
d_0	Minimum distance between any two adjacent points to construct a regular lattice with n identical tetrakaidekahedral cells
E	Young's modulus
E_C	Young's modulus of composite
$(E_c)_{Hs\_Upper}$	Upper limits of Young's modulus in Hashin-Shtrikman bound
$(E_c)_{Hs\_Lower}$	Lower limits of Young's modulus in Hashin-Shtrikman bound
E_f	Young's modulus of fibre
$\overline{E}_f$	Modified Young's modulus of fibre
E_m	Young's modulus of matrix
E_N	Normalized Young's modulus
E_x, E_{cx}, E_y, E_z	Young's modulus in the *x*, *y*, or *z* directions
E_1, E_{12}	Groups of nodes on the edges (except the vertices) of an RVE
$E_{1\,i}, E_{12\,j}$	A node on the edges (except the vertices) of an RVE

es, es_f, es_m	Element size
f	Volume fraction
f_A	Volume fraction of constituent material A
f_B	Volume fraction of constituent material B
f_f	Volume fraction of the fibre
f_m	Volume fraction of the matrix
F_r	Reaction force of the reference node
F_{xn}, F_{yn}, F_{zn}	Groups of nodes on the facets on the *YZ, XZ, or XY* plane of coordinates *oxyz*, separately, of an RVE
F_{xp}, F_{yp}, F_{zp}	Groups of nodes on the facets opposite to *YZ, XZ, or XY* plane, separately, of an RVE
$F_{xn\,i}, F_{xp\,j}$	A node in group F_{xn}
$G_{,}\,\mu$	Shear modulus
G_{12}, G_{23}, G_{13}	Shear modulus in the *xy*, *yz*, or *xz* directions, separately
H	Edge length of RVE
K	Bulk modulus
k_{avg}	Averaged conductivity
l, l_i	Fibre length
L	Edge length of an RVE
l_t	Total fibre length

N_f	A node on a fibre of a 3D Voronoi fibre network
$N_m, N_{m'}$	A pair of corresponding nodes on the matrix of a 3D Voronoi fibre network composite RVE
n	Number of Voronoi points
$\mathbf{P}, \{p_1, \dots, p_n\}$	A given set of discrete points
$\mathbf{P}_\mathrm{r}$	A random set of discrete points
R, R_i	Voronoi cell
St_{Var}	Standard variance
T	Shape-dependent strain relation tensor
u_x, u_y, u_z	Translation of an FE node in *x*, *y* or *z* directions, separately
U	Translations of an FE node in *x*, *y* and *z* directions.
$U_j, U_{j'}$	Translational degree of freedoms of a pair of nodes
U_f	Translational degree of freedoms on the node of a fibre of a 3D Voronoi fibre network
$U_{V1\,i}, U_{E1\,i}, U_{Fxn\,i}$	Translations of a node among the nodes in V_1, E_1 or F_{xn} of the RVE
V_1, V_i	A node on a vertex of a cubic RVE
$\boldsymbol{X}$	A metric space with distance function *dist*
ν, ν_c, ν_{cxy}	Poisson's ratio
ψ	Shape factor

δ	Minimum allowable distance between the points seeded for Voronoi tessellation
δ_{max}	Maximum of δ
ξ	Aspect Ratio

Chapter 1 Introduction

1.1 Research Background and Objectives

Interpenetrating phase composites (IPCs) are a class of composite in which two or more constituent phases are continuous in their geometry and each phase is interconnected in its architecture or microstructure [1]. When crack or other type of failures occur from one phase of the IPCs, the structural completeness and loading capacity will still be maintained by the other phase or phases. The co-continuous structure of all the phases provides the IPCs with many advantages compared to its conventional, discretely reinforced counterparts, such as particle, whisker or unidirectional fibre reinforced composites. IPCs attract the attentions of both academic and industrial researchers in different disciplines. Aviation, aerospace and other weight-sensitive industries employ IPCs for its good stiffness/weight ratio. The characteristic of no significant directional dependency or distinct weak planes makes IPCs ideal for structural applications. High temperature and high cycling fatigue applications utilize IPCs as they are more resistant to thermal and fatigue damage. Each phase of an IPC contributes its own property to the overall composite. Thus, it is possible to tune IPCs to get satisfiable mechanical, thermal or conductive properties at the same time by retaining those properties of the constituent phases. This character attracts the attention of functional material researchers and manufacturers. However, IPCs were relatively difficult to fabricate. Long processing time and extensive manufacturing conditions resulted in high costs as well. Besides, the microstructures of IPCs were not easily controllable during fabrication. How to get an expected, homogeneous microstructure was also an obstacle for IPC applications.

The advancement of metal manufacturing processes such as metallurgy, moulding and casting takes down the cost of IPC production. Different types of IPCs are fabricated and experimentally investigated. It is hard to describe the microstructure of an IPC, especially a metal-metal IPC via 3D models, as their microstructures are highly

irregular and cannot be represented by simple 2D and 3D shapes like lines or cubes. Tetradecahedrons was widely used to equivalently illustrate many different IPC structures. Recently, the rise and maturating of additive manufacturing enables the fabrication of precisely designed architecture or microstructure in IPCs.

The underlying relation between microstructure of the composite, mechanical properties of constituent materials and the mechanical properties of composites remains unclear. Therefore, it is obliged to investigate the mechanical properties of different types of interpenetrating composites. This thesis attempts to give a glance of how the mechanical properties of constituent materials affect those properties of the composites with different microstructures. To predict the effect of structures and mechanical properties of constituent materials on the mechanical properties of the composite, we aim to construct different types of 3D, lattice structure reinforced interpenetrating composites and compare their elastic properties. Four different types of regular lattice reinforced structures, three different types of regular auxetic lattice reinforced structures are considered. 3D Voronoi fibre reinforced structure is also taken into account.

The main contributions are organized into four chapters as follows:

1. Four types of regular three-dimensional isotropic lattice structured representative volume element (RVE) models to describe IPCs with different types of regular reinforcement structures are build. The models are prepared to be periodic and ready to analyse with finite element (FE) method. Periodic boundary conditions for solid cubic RVEs are presented and coded for automatically applying them to any cubic RVE. The elastic modulus of the composites is found to be determined by the combination of fibre volume fraction and the mechanical properties of the constituent materials. The elastic properties of these models are investigated and compared. Stiffness of all those IPC models are superior among composite structures and the capability to tune the mechanical properties by adjusting the corresponding mechanical properties of the constituent materials is appealing. Under some of the constituent

materials combinations, Young's moduli of all types of IPCs could exceed the Voigt limit, which has long been regarded as the upper limit of the Young's moduli of two-phase composites. The weight/stiffness ratio of regular lattice structured IPCs can be largely affected by the fibre volume fraction and a best range of fibre volume fractions can be found.

2. Models of three types of regular auxetic lattice network reinforced isotropic structures are created. The concavity of different types of auxetic structure is defined and considered as one of the crucial parameters that affect the Poisson's ratio of the composite. Elastic properties of the constituent materials are also considered. It is discovered that the Poisson's ratio of these kind of IPCs can be tuned to zero or negative figures while the Poisson's ratios of both the matrix and the reinforcement are positive. Meanwhile, these composite models also have good stiffness. They are desirable for functional materials in different applications such as impact resistant materials, artificial bones and other biomechanical uses.

3. 3D Voronoi fibre network reinforced IPC models are constructed. The process of generating periodic Voronoi fibre networks is specified and coded to generate Voronoi fibre networks with different Voronoi cell numbers. ASC technique enables the constraints of beam element fibres and solid element matrix, instead of full solid element mesh of the RVEs. The elastic properties of 3D Voronoi fibre network reinforced IPCs are predicted. The effect of the number of fibres, coefficient of regularity and fibre volume fractions on the stiffness of this kind of IPCs are revealed.

1.2 Thesis Outline

In relation to the major objectives, the thesis is organised as follows:

Chapter 1 introduces the background of this work, gives the key objectives and contributions, and outlines the framework of the thesis.

Chapter 2 presents a review in the domain of composite materials including the discontinuous reinforcement composites, unidirectional/aligned fibre reinforced composites, and interpenetrating phase composites. Furthermore, the microstructure behind the auxetic behaviour, related auxetic materials and their composites are also reviewed. In addition, a brief review of fibrous materials including cellular materials and stochastic fibrous materials is given.

Chapter 3 demonstrates the technique of constructing three-dimensional isotropic regular fibre networks composite models. An introduction of periodic boundary conditions (PBCs) and how to revise them in FE analysis to fit the solid RVE is included in this chapter. Four different types of regular lattice structured IPC models are constructed by volume Boolean operation. They are solved to obtain their elastic properties under the constraint of PBCs. Fibre volume fractions, Young's moduli, and Poisson's ratios of the constituent materials are considered as key parameters to affect the stiffness of the composites.

Chapter 4 introduces the way to construct solid and isotropic auxetic composite structures by embedding auxetic fibre networks into matrices. Three different regular auxetic lattice reinforced isotropic structures are constructed. They are investigated to show how structures affect the Poisson's ratio in the aspects of concavity, volume fraction and material combination of two constituent phases.

Chapter 5 explores the elastic property of 3D Voronoi fibre network reinforced composites. 3D Voronoi fibre networks are generated with different coefficient of regularity and different numbers of Voronoi cells to evaluate their effect on the stiffness of the composite. ASC technique and PBCs are applied to build RVEs of the 3D Voronoi fibre network reinforced composites. The mesh sensitivity of ASC coupling is investigated to ensure an accurate FE approach to the mechanical properties of this kind of composites. The influence of the Young's moduli and Poisson's ratio of the constituent material is also considered. A comparison between different IPC structures built in this work is given to determine which are the best structure at given conditions.

Chapter 6 summarises the main conclusions of this thesis. Furthermore, limitations regarding the current work and possible further works are stated.

Chapter 2 Literature Review

2.1 Composite materials

Composite material is a wide range of materials which includes all the materials that are formed from two or more constituent materials with different physical or chemical properties [2]. By combining those ingredients, a material with different characteristics could be produced. However, different from mixtures, the individual materials remain separate and distinct within composites. Composites received much attention as they have desirable combinations of properties which are hard to find in the individual components.

The concept of "composite" has existed since the Palaeolithic age. It was reported that the ancient Mesopotamians around 3400 B.C used clay mixed with finely chopped straw (mud and reed) to build a temple tower in the city centre of Babylon [3]. Moreover, it was stated that composite bricks were made by putting straw within mud bricks since the time of Pharaoh in Egypt [4]. In a historical review of the mechanics of composites, it was reported that Egyptians used fibre composites for laminated writing materials as well [5]. Civilizations throughout the world have used basic elements of their surrounding environment in the fabrication of dwellings including mud/straw and wood/clay.

In the late 1800s, canoe builders began experimenting different materials to make paper laminates. Layers of kraft paper were glued together with shellac. Those attempts failed because the available materials were not up to the task. However, that was the rudiments of resin-based composite. The first synthetic resins that could be converted from liquid to solid (using a chemical process called polymerization) were developed between 1870 and 1890. These polymer resins were transformed from the liquid state to the solid state by crosslinking the molecules [6].

Leo Baekeland brought composite materials to modern era with the invention of 'Bakelite', a practical synthetic resin. The procedure of synthesis, constitution, and

possible uses of Bakelite was well stated in his publication [7] in 1909. Military, planes and high end, luxury cars took the advantage of the composite material almost immediately regardless of cost. The first industrial application of Bakelite was for the Rolls Royce automobiles and then it was rapidly introduced to aviation industries. Polyester resin and glass fibre reinforcement were produced by chemical companies such as American Cyanamid and Dupont from 1920s to 1930s. The composite enjoyed a rapid increase of usage during the War when the manufacture technique improved fast. After the War, many industries, including warship, fighter, bomber in military and boats, pipes, ducts in civil engineering, embraced composite materials.

Carbon fibres with high strength and stiffness were developed by Royal Aircraft Establishment (RAE) in 1953 [8]. As it was easy to make carbon fibre to complicated geometrical shape with desirable elastic properties, carbon fibres were used as reinforcements in composites in 1960s, soon after its invention. In 1970s to 1980s, different economy alternatives of fibre reinforced composite (FRC) manufacturing were developed. The application of composites spread to the infrastructure, appliances, and other uses where cost matters for the product's competitiveness.

The recent four decades have witnessed how modern composite materials became ubiquitous and indispensable in various applications. Fibre reinforced composites have formed a well-developed system and gained popularity in various daily life products like clothing, bicycle frames, fishing rods, baseball bats and tennis rackets. Strong materials including glass fibres, carbon fibres, silicon carbide, alumina and alumina compounds are used as reinforcement. The matrix, polymeric, metallic or ceramic, binds the fibres together. The matrix mainly functions as a medium to transfer the load applied to the fibres, the principal load-bearing component. For discontinuous reinforcement composites such as particulate composites and unidirectional fibre reinforced composites, the matrix enabling the composite to withstand compression, flexural and shear forces as well as tensile loads [9]. For interpenetrating phase composite, matrix fill the porous fibres to make the composite geometrically solid. Composite materials also benefit much from novel materials and manufacturing

technologies. Carbon nanotubes are good reinforcements for their exceptional mechanical stiffness and tensile strength. Rapid prototyping and additive manufacturing, which produce shaped parts by gradual creation or addition of solid material, started in late 1980s and has enjoyed a rapid rise in the past three decades [10,11]. Additive manufacturing has become a popular alternative to fabricate composite materials. For example, as additive manufacturing shapes a component layer by layer, it is suitable to produce functional graded materials [12–14].

It is always a critical problem to obtain or predict the mechanical properties of the composite materials. It is difficult to figure out the distribution, the blending feature, the microstructure and the interface conditions of the matrix and reinforcement. Different empirical, analytical and experimental approaches were provided to predict the effective properties of the composite [15–18]. The Hashin-Shtrikman (HS) model, for example, treats the composite as an isotropic aggregate and the model is based on variational principles of linear elasticity [18]. HS bounds are widely considered as the tightest bounds in terms of composite moduli for a two-phase composite material. By specifying the volume fractions and the mechanical properties of the constituent, the upper and lower bounds for the elastic moduli of any composite material can be calculated. The Hashin-Shtrikman bounds for the Young's, *E*, bulk, *K*, and shear moduli μ are given by,

$$(E_c)_{HSUpper} = E_a + \frac{f_b}{\frac{1}{E_b - E_a} + \frac{f_a}{3E_a}} \tag{2.1}$$

$$(E_c)_{HSLower} = E_b + \frac{f_a}{\frac{1}{E_a - E_b} + \frac{f_b}{3E_b}} \tag{2.2}$$

$$(K_c)_{HSUpper} = K_a + \frac{f_b}{\frac{1}{K_b - K_a} + \frac{f_a}{\left(K_a + \frac{4}{3}\mu_a\right)}} \tag{2.3}$$

$$(K_c)_{HSLower} = K_b + \frac{f_a}{\frac{1}{K_a - K_b} + \frac{f_b}{\left(K_b + \frac{4}{3}\mu_b\right)}} \tag{2.4}$$

$$(\mu_c)_{HSpper} = \mu_a + \frac{f_b}{\frac{1}{\mu_b - \mu_a} + \frac{2f_a(K_a + 2\mu_a)}{5\mu_A\left(K_a + \frac{4}{3}\mu_a\right)}} \tag{2.5}$$

$$(\mu_c)_{HS_{Lower}} = \mu_b + \frac{f_a}{\frac{1}{\mu_a - \mu_b} + \frac{2f_b(K_b + 2\mu_b)}{5\mu_a\left(K_b + \frac{4}{3}\mu_b\right)}} \tag{2.6}$$

where subscript *c* represents for the properties of the composite while subscript *a*, *b* represents for two phases of the composite. Thus, f_a, f_b are volume fractions of the two constituent materials of the composite and obviously, $f_a + f_b = 1$.

There are also other bounding methods to estimate the effective mechanical properties of the composites. Reuss bounds is obtained by assuming the stress field remains constant throughout the material in an arbitrary average strain field. Reuss bounds was originally considered in the domain of mixed crystals, given a looser estimation of the bounds of the composites [19]. On the other hand, Voigt limit is obtained by assuming the strain field remains constant throughout the material in an arbitrary average stress field. Voigt limit has long been regarded as the upper limit of the stiffness of isotropic composite materials by researchers and textbooks. The Reuss and Voigt limit are as follows:

$$(E_c)_{Voigt} = E_a VF_a + E_b VF_b \tag{2.7}$$

$$(E_c)_{Reuss} = \frac{E_a E_b}{E_a VF_b + E_b VF_a} \tag{2.8}$$

In addition, Mori-Tanaka method also uses the average local stress and strain fields in the constituents of a composite to estimate the effective material properties of the composite, but in a more complicated way [17]. Benveniste [20] provided a more direct

and simplified derivation of the Mori-Tanaka method, predicting the effective shear and bulk moduli μ and K as follows:

$$\mu = \mu_a + f_b(\mu_b - \mu_a)\left[\frac{1 + f_b(\mu_b - \mu_a)}{\mu_a + \frac{\mu_a(9K_a + 8\mu_a)}{6(K_a + 2\mu_a)}}\right] \tag{2.9}$$

$$K = K_a + \frac{f_b(K_b - K_a)}{1 + f_a\left[\frac{K_b - K_a}{K_a + \frac{4}{3}\mu_a}\right]} \tag{2.10}$$

It can be seen that the prediction of bulk moduli by the Mori-Tanaka method above is the same as that of the Hashin-Shtrikman bounds. Once the above equations are evaluated, Young's modulus E and Poisson's ratio ν of the composite are given as follows:

$$E = \frac{9\mu K}{\mu + 3K'} \tag{2.11}$$

$$\nu = \frac{3K - 2\mu}{2(\mu + 3K)} \tag{2.12}$$

Some models are semi-empirical, such as the Halpin–Tsai (H–T) model, which is an approach modified from continuous fibbers to discontinuous reinforcement. However, although prediction approaches relist above such as Mori-Tanaka method, Voigt limit and Hashin-Shtrikman bounds could provide bounds of the mechanical and physical behaviour of the composites, they are not able to capture precisely the experimentally observed behaviour of the composites, because the microstructures of the composites are not considered.

The concept of composite materials is so general that no review paper can include all kind of composites materials. On the contrary, review papers often focus on a certain kind of composite materials, presenting a relatively complete scope of that kind of composite. There are different approaches to classify the composite materials, e.g. by structure type, by manufacturing alternatives, by applications, by matrix and material

types, etc. Under different categories of composite materials, there are plenty of reviews for reference. For example, Singhal *et al.* [21] gave a review of composite materials made by microwave sintering. Quan *et al.* [22] reviewed the multi-directional preforms for composites produced by additive manufacturing. Polymer-composite materials used in biomedical applications were also outlined [23]. Stankovich summarized the graphene based composite materials [24]. As a hot research spot, a critical review on nanotube and nanotube/nanoclay related polymer composite was given [25].

The following types of composites listed below in this Chapter are neither a full-scope review in every perspective of composite materials to cover all kinds of composite materials, nor a review which concentrates on a certain aspect of the composite material world. On the contrary, they present brief reviews of the composite material topics related to this research.

2.1.1 Discontinuous reinforcement composites

Discontinuous reinforcement composite is one of the most common composites. The most widely used and famous discontinuous reinforcement composite should be concrete, which are coarse to medium grained particulate aggregate bonded with fluid cements. Different types of particles, whiskers and short fibre reinforced composites are developed other than concrete for their strength, stiffness, good thermal and electrical conductivity, excellent high temperature performance and good wear resistance. Metal matrix composites (MMCs) is one of the important parts of discontinuous reinforcement composites. For metal matrix composites, the continuous fibres reinforced MMCs were confined to ultrahigh-performance applications for their cost, complex fabrication routes and limited fabricability. Therefore, discontinuous fibres (short fibres, whiskers) composites were developed for various applications. Particularly, Al, Mg, and Ti-based matrix, short staple Al_2O_3 fibre and SiC whisker reinforcements are popular. For example, Disc brake manufacturing for railway vehicles has become a popular field for assessing the possibilities of Al-based particulate MMC applications [26].

One of the problems encountered in the manufacturing of discontinuous reinforcement composite is the distribution of the reinforcement. Generally, the dispersibility of particles in the matrix is better in low volume fractions than high volume fractions. It was found that in 1% and 2% particle volume fractions (vol.%) of situ CaB_6/Al-Cu-Mn composites, nanoparticles were distributed in the matrix uniformly [27]. However, when it reached 3% particle volume fraction, the CaB_6 nanoparticles tended to aggregate into clusters [27]. Coincidentally, it was reported that the uniform dispersion of nano Al_2O_3 particles was achieved in A356 alloy (7Si-0.3Mg alloy with 0.2 Fe max and 0.1 Zn max) with 1.5% volume fraction of nano particles, while in the 3.5% or above nano particle volume fraction, the agglomeration of reinforcement powders occurred [28]. Figure 2-1 gave a microstructure of the Duralcan aluminium alloys, which provided a general sketch of the microstructure of MMCs [29]. The hardness, tensile, and compressive strength of the composites increased with decreasing particle size and increasing reinforcement content.

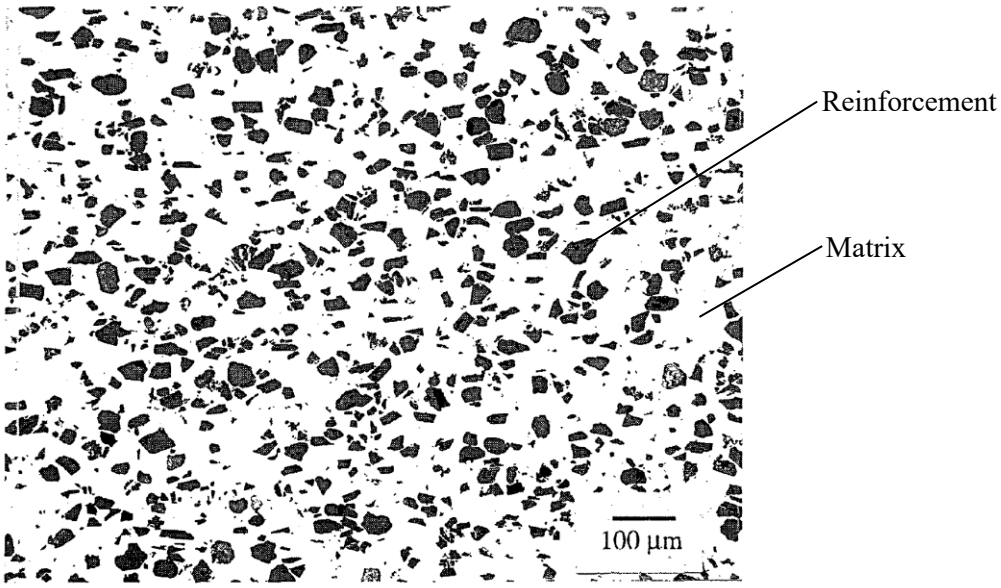

Figure 2-1. Microstructure of Duralcan 6061, 20% vol.% Al_2O_3 composite [29].

The mechanical properties of particle reinforced composites have long been a hotpot in research of material and mechanics. Theoretical approach of the effective elastic moduli of misoriented short-fibre composites was presented by Chen and Cheng [30]. They

found that the longitude elastic moduli E_{11} of a short-fibre-reinforced composite increases faster than linearly with reinforcement volume fraction f_1. Other than corresponding properties of the fibre and matrix, length-diameter aspect ratio of discrete fibres t, and the orientation distribution parameter λ also maters to the elastic moduli [30]. Furthermore, the fibre orientation distribution and aspect ratio have a more significant effect on composite longitudinal Young's modulus than the fibre volume fraction within the range examined [30].

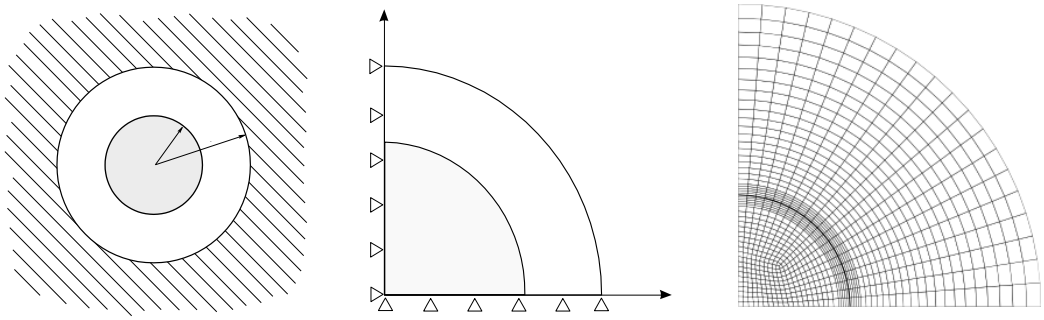

Figure 2-2. Illustration of unit cell models: (a) three phase model, (b) unit cell model and (c) finite element (FE) model mesh [31].

The particulate composite could be idealized as three-phase composite spheres model (TPM) following Fröhlich and Sack [31], as Figure 2-2 (a) shows. For simplicity, representative unit cell methods were also employed for evaluating the effective elastic properties of particulate composites, as Figure 2-2 (b) shows. The results showed that the elastic constants predicted by the axisymmetric spherical unit cell match closely with the experimental data on glass-epoxy composites [32]. At filler concentrations below 15 vol.%, the stress state at the inclusion interface determined using unit cell model agreed well with TPM. However, when the volume fraction is larger than 20%, the results of TPM, 3D unit cell, cylindrical unit cell, and spherical model differs much in both Young's modulus and Poisson's ratio [32].

Eshelby [33] considered the three-dimensional elasticity problem of the particle reinforced composites as a single ellipsoidal inclusion in an infinite matrix. This approach has been employed quite extensively in modified forms when analysing

discontinuously reinforced composite materials. Mura [34] provided estimations of shear and bulk moduli μ and K for finite concentrations of reinforcements. Taking the reinforcement geometry to be spherical, the Mura expressions for the effective moduli are:

$$\mu = \mu_m \left[1 + \frac{VF_r(\mu_m - \mu_r)}{\mu_m + 2(\mu_r - \mu_m)\frac{4 - 5\nu_m}{15(1 - \nu_m)}} \right]^{-1} \quad (2.13)$$

$$K = K_m \left[1 + \frac{VF_r(K_m - K_r)}{K_m + (K_r - K_m)\frac{1 + \nu_m}{3(1 - \nu_m)}} \right]^{-1} \quad (2.14)$$

where the subscript m stands for the matrix and the subscription r stand for the reinforcement. However, microstructural aspects of the composite, such as particle size, shape, and distribution are vital in determining the mechanical properties of the composite. Therefore, analytical models and numerical models which simplified the microstructure of the composite models are unable to accurately predict the properties of particle-reinforced composite material since these models do not include the microstructural factors that influence the mechanical behaviour of the material. To deal with this issue, Chawla *et al.* [35] presented a reconstructed 3D microstructure of SiC particle-reinforced aluminium composites utilizing a serial sectioning process. The localized stress and plasticity were observed due to the sharp and angular nature of irregular particles. The serial sectioning method, reconstruction, and 3D microstructure-based FEM used was considered a significant improvement over 2D and 3D unit cell and simple multiparticle models.

Furthermore, representative volume element (RVE) has been used to evaluate the effective material properties with periodic boundary conditions. Segurado and Llorca [36] and Böhm *et al.* [37] assessed the effective coefficients of randomly distributed spherical particles using the random sequential adsorption (RSA) algorithm and compared those with different analytical methods. Sreedhar Kari [38] modified the random sequential adsorption algorithm to generate 3D representative volume element

models of randomly distributed spherical particles, as Figure 2-3 shows. Hua and Gu [39] modelled composite with random distributed sphero-cylinder shaped particles, as Figure 2-4 shows.

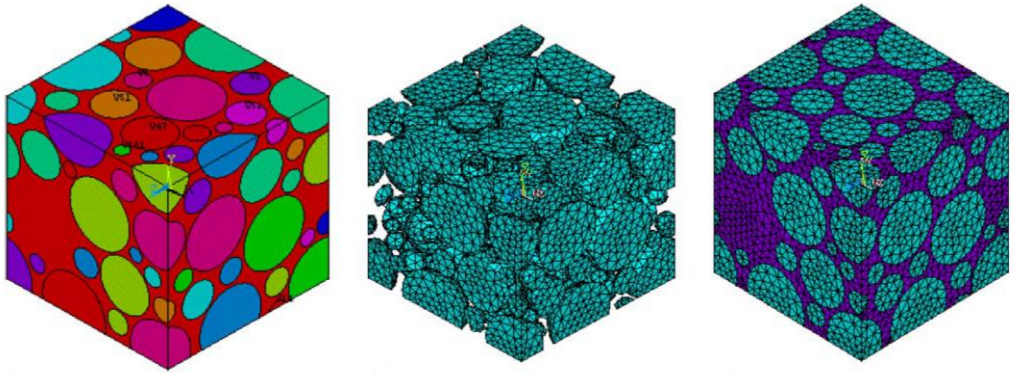

(a) (b) (c)

Figure 2-3. 3D RVE models of randomly distributed spherical particles created by random sequential adsorption algorithm (RSA) (a) geometric model, (b) meshed particles and (c) meshed RVE [38]

(a) (b) (c)

Figure 2-4. RVE with random distributed sphero-cylinder shaped particles. (a) geometric model, (b) meshed particles and (c) meshed RVE [39].

It was found that volume fraction of the particles had significant impact on the mechanical behaviour of the composite. Stiffer particles could improve the effective Young's modulus, while the overall sensitivity of the effective Poisson's ratio with respect to the particle stiffness was minimal. The particle orientations also strongly impacted the mechanical properties of MMCs, especially along the longitudinal direction.

Moreover, it was discovered that the mechanical properties of MMCs can be further enhanced by decreasing the sizes of ceramic particulates and/or matrix grains from micrometre to nanometre level. Such materials are referred to as the nanocomposites [40]. Sadeghian [41] fabricated Al-TiB_2 nanostructured composite by mechanical alloying from pure Ti, B and Al powder mixture and evaluated its mechanical behaviour. Al 20% weight ratio (wt.%) TiB_2 nanocomposite showed a tensile strength around 540MPa [41]. Al 5083/SiC_p nano composite was synthesized by high energy ball milling and spark plasma sintering and demonstrated an elastic modulus of 126GPa [42].

2.1.2 Unidirectional/aligned fibre reinforced composites

Fibre reinforced composites have been produced for centuries. Fibre glass, or in other names such as glass-reinforced plastic (GRP), glass-fibre reinforced plastic (GFRP), was one of the earliest fibre reinforced composites which has been put into practice. Its patent was awarded to Hermann Hammesfahr in the U.S. in 1880 [43]. Industrial applications of fibre glass include aircrafts, boats, automobiles, bathtubs and enclosures, swimming pools, hot tubs, septic tanks, water tanks, roofing, pipes, cladding, orthopaedic casts, surfboards, and external door skins.

The principles of fibre reinforcement have been adumbrated for a few years since the mass production of fibreglass and have been extended to the reinforcement metals in 1960s. Tensile tests were carried out on tungsten or molybdenum wires reinforced copper [44]. Reinforcement of tungsten or molybdenum wires was uniaxially aligned in copper matrix. Both continuous and discontinuous wires have been used, and both brittle and ductile tungsten wires [44]. A linear relationship between strength and fibre volume fraction for a particular aspect ratio was found to fit the experimental data, as Figure 2-5 shows.

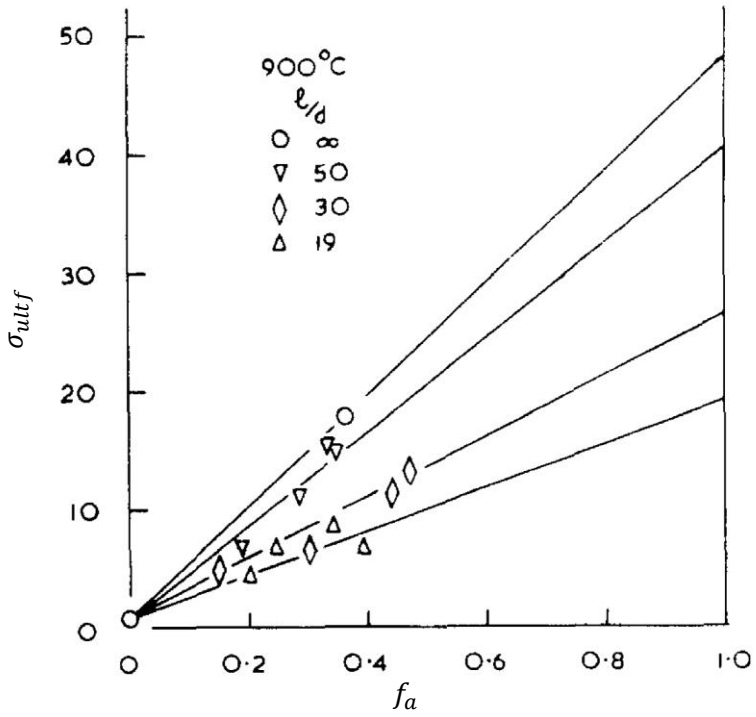

Figure 2-5. Tensile strengths of copper/molybdenum composites tested at 900℃ [44].

Recently, a growing trend suggests that it is more sustainable to use natural fibres as reinforcements in polymer composites instead of synthetic fibres like glass. In addition, natural fibres reinforced composites is presently receiving increasing attention because of its cost effectiveness, low density, and high specific strength [45–47]. Selected natural fibres, mostly plant based fibres such as ramie, flax, hemp, harakeke, sisal, alfa, cotton, coir with proper harvest time and treatment can reach desirable mechanical properties [48]. A graphical overview of the range of strength, stiffnesses, specific stiffnesses and specific strengths of natural fibre composites (NFC) compared with those for glass fibre reinforced plastics produced by Shah [49] is shown in Figure 2-6.

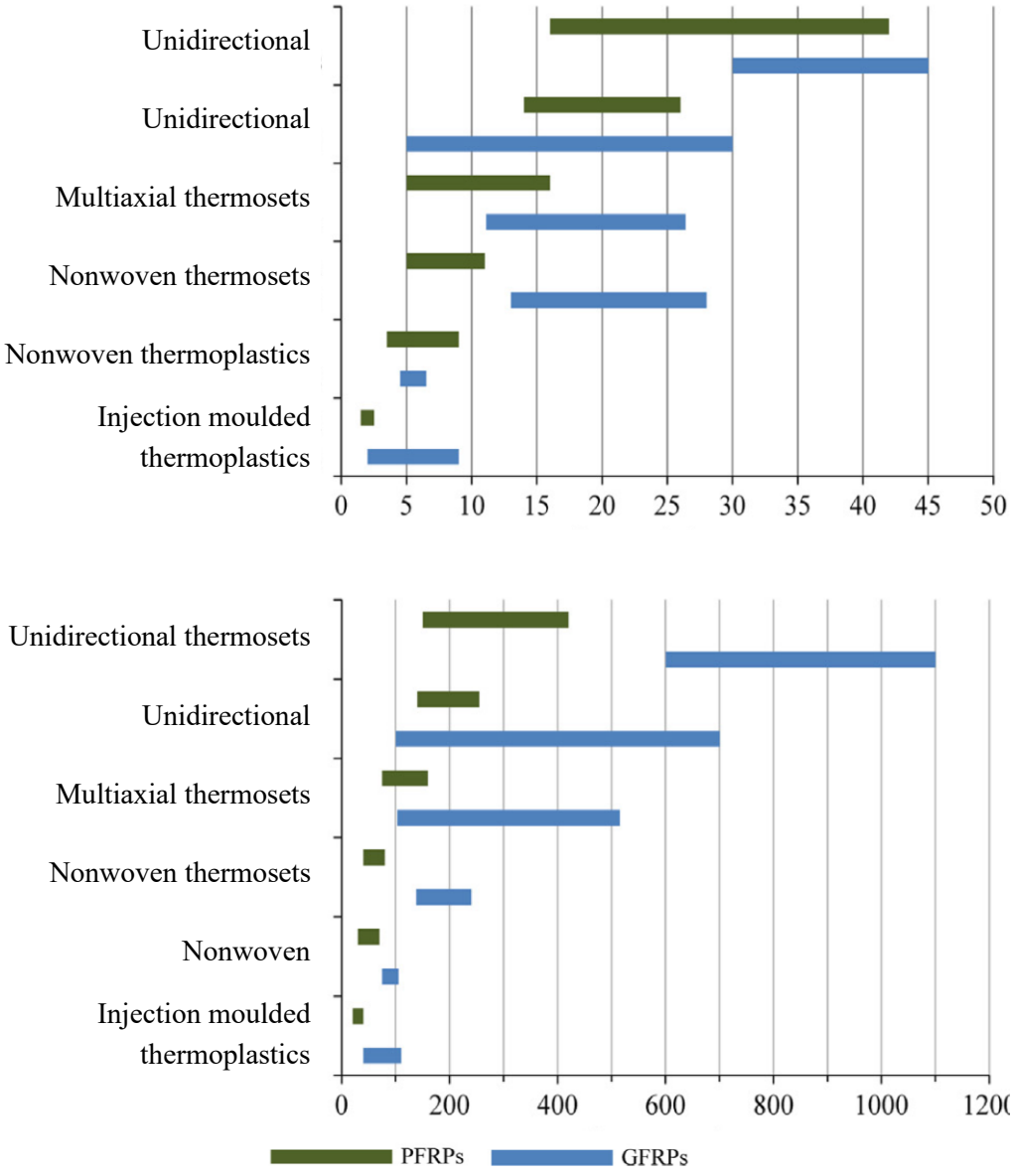

Figure 2-6. Comparison of stiffness and strength of NFCs (upper of paired bars, green) with glass fibre reinforced plastics (lower of paired bars, blue) [49].

Besides, highly oriented, co-extruded polypropylene (PP) tapes allow the production of recyclable unidirectional 'all-polypropylene' composites. The specific mechanical properties are comparable to those reported for a commercial unidirectional glass fibre reinforced PP, while the all-PP composites clearly have great advantages in terms of recyclability [50].

Various analytical and experimental research on the mechanical properties of uniaxial/random fibre reinforced composites have been conducted. Thomason [51]

reported the influence of fibre length and concentration on the mechanical properties of glass fibre-reinforced polypropylene. For random, in-plane, glass fibre-reinforced polypropylene laminates, the modulus of these laminates increases linearly with fibre content up to 40% in weight. Above 40% fibre content weight, improvement of the modulus is considerably less [51]. Modulus is practically independent of fibre length above 0.5mm. The tensile stress-strain curve was determined in a Ti–6Al–4V alloy uniaxially reinforced with 35 vol.% Sigma 1140 and SiC monofilaments. The composite exhibited a bilinear stress–strain curve as Figure 2-7 shows.

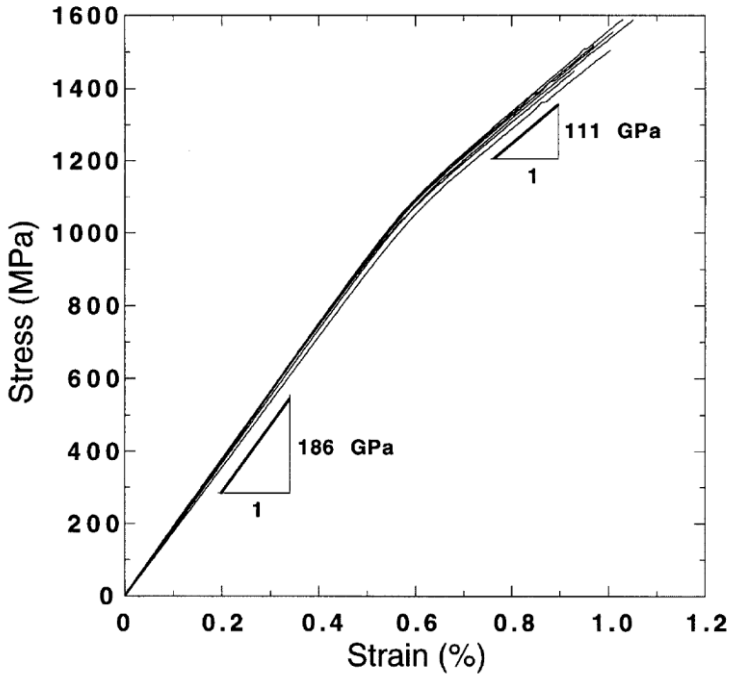

Figure 2-7. Tensile stress–strain curves of six tensile tests of Ti–6Al–4V alloy uniaxially reinforced with 35 vol. % Sigma 1140+SiC monofilament [52].

Computational micromechanics tools such as representative volume element and periodic boundary conditions were also introduced to investigate the mechanical properties of fibre reinforce d composites [53].

2.1.3 Interpenetrating phase composites

Interpenetrating phase composites (IPCs) is the main target of this thesis. The most significant character of IPCs is the interconnectivity of each constituent phase of the composite. Consequently, many attractive properties in each of the constituent phases may be retained in the composite. Each phase of the interpenetrating composite can bear loads independently and hold the completeness of the structure, even if one phase of the composite fails. Interpenetrating composites often exhibit excellent mechanical and physical properties compared with its discontinuous counterparts. Breslin *et al.* [54] developed an interpenetrating Al_2O_3 and Al composite, consisting of approximately 65% (by volume) of Al_2O_3. It was a novel co-continuous ceramic-metal composite, thus called C^4 material. A list of physical and mechanical properties is shown in Table 2-1. It can be seen that the thermal conductivity is twice that of steel while the coefficient of thermal expansion is smaller than that of steel.

Table 2-1. Physical and mechanical properties of co-continuous ceramic-metal composite

Property	Value
Density	3.5-3.7 g cm^{-3}
Thermal conductivity	80 W K^{-1} m^{-1}
Coefficient of thermal expansion	10×10^{-6} K^{-1}
Young's modulus	215 GPa
Average modulus of rapture a in three-point bend	470 MPa
Fracture toughness	10.5 MPa $m^{0.5}$

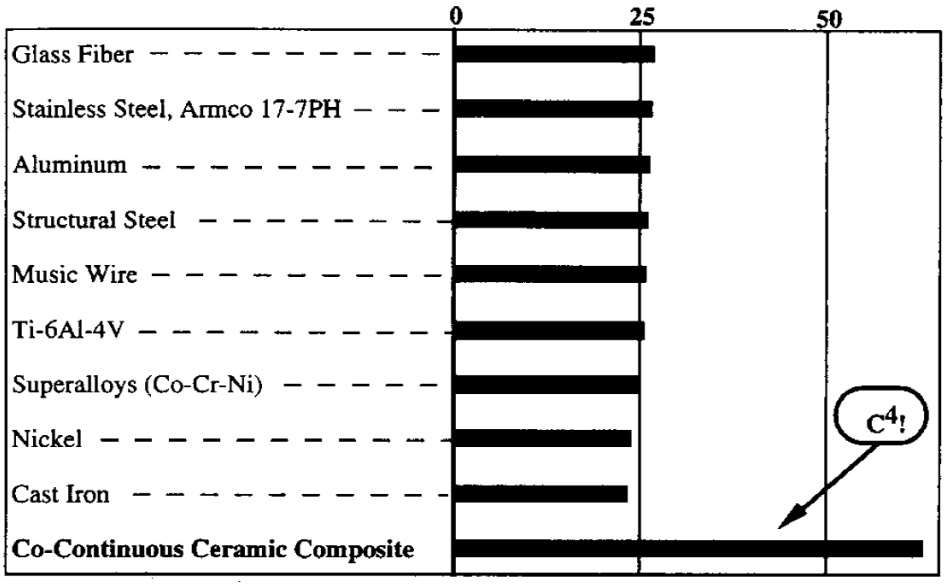

Figure 2-8. Comparison of specific stiffnesses (stiffness to weight ratio) of various materials with that of C^4 [54].

A comparison of specific stiffness (stiffness to weight ratio) is given in Figure 2-8. It is obvious that the specific stiffness of C^4 material is superior compared with materials like aluminium or Ti-6Al-4V [54]. The uniaxial elastic and plastic behaviour of C^4 material has then been studied by the same group both experimentally and analytically via finite element method. A bilinear tensile stress vs strain loading curve was observed from the result of a typical tensile test. The C^4 material exhibit an elastic modulus near 207 GPa and a linear plastic modulus of approximately 108 GPa [55]. However, confined to the computational method and tools in the 1990s, Breslin *et al.* used a simplified two-phase interpenetrating representative volume element to represent the composite, which led to slight deviation from the experimental results of elastic modulus. Similar alumina/aluminium composites with interpenetrating microstructures were made by infiltrating an alumina preform which had the structure of a reticulated ceramic foam [56]. Interpenetrating composites produced by this approach also possess higher elastic modulus than conventional metal matrix composites with a homogeneous reinforcement distribution. Furthermore, metal-epoxy and metal-syntactic foam IPCs were processed and tested. The result showed that the elastic modulus of syntactic foam

reinforced by interpenetrating open cell aluminium preform doubles comparing the syntactic foam itself while its density rises less than 10% [57].

Robert J. Moon, Matthew Tilbrook, and Mark Hoffman [58] presented a comparison of different theoretical composite modulus prediction methods including Ravichandran, Tuchinskii, Hashin-Shtrikman, and the effective medium approximation (EMA). The effective Young's moduli of co-continuous Al-Al_2O_3 composites over the 5 to 97 vol% Al_2O_3 composition range were experimentally measured and compared with those prediction methods. The results showed that the EMA, with an appropriate microstructural shape factor, was the most consistent method for approximating the composite Young's modulus [58]. The EMA method uses Eshelby's [33] ellipsoidal inclusion shape-dependent strain relation tensor, *T*, to consider the inclusion shape. A shape factor, ψ, is used to describe the ellipsoid aspect ratio. The weighted mean effective bulk and shear moduli, *K** and *G** are defined by:

$$(K_1 - K^*)f_1 \cdot T_{k1} + (K_2 - K^*)f_2 \cdot T_{k2} = 0 \qquad (2.15)$$

$$(G_1 - G^*)f_1 \cdot T_{G1} + (G_2 - G^*)f_2 \cdot T_{G2} = 0 \qquad (2.16)$$

These equations and tensors are given in reference of Kreher and Pompe [59], as well as Tilbrook *et al.* [60]. The full piecewise functions in terms of shape parameter ψ and shape-dependent strain relation tensor *T* is provided [60]. However, this method was still doubted as the relation between the actual shape of reinforcement phase and the shape factor, ψ, is unclear. The relation between Young's modulus of the composite and the Al_2O_3 volume fraction predicted by different methods are shown in Figure 2-9.

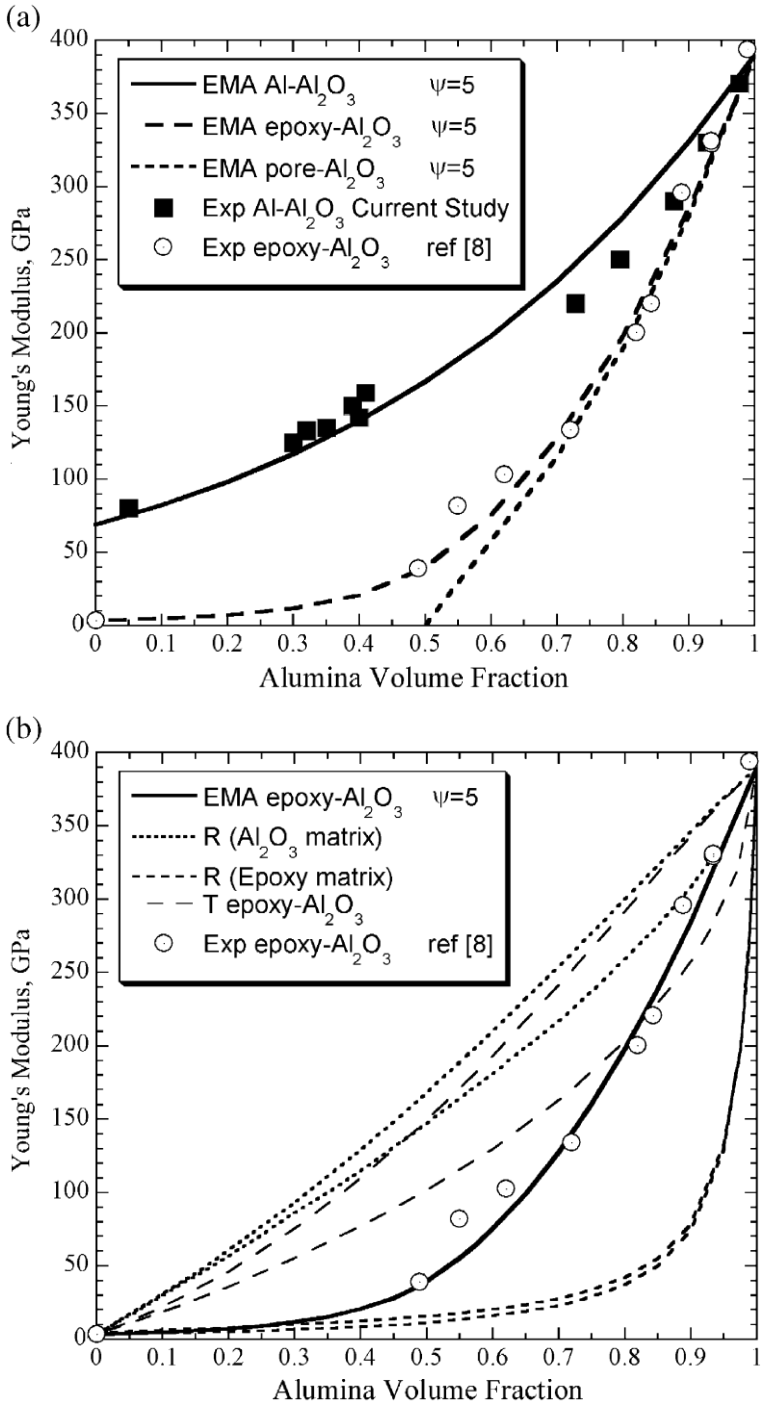

Figure 2-9. Effect of the modulus ratio (E_1/E_2) on the effective composite modulus. (a) comparison between epoxy-Al_2O_3, and Al-Al_2O_3 measured composite Young's modulus with effective medium approximation (EMA) ($\psi = 5$) predictions. (b) epoxy-Al_2O_3, composite modulus plotted with EMA ($\psi = 5$), and the Ravichandran (R in the legends) and Tuchinskii Bounds (T in the legends) [59].

The main limit of the EMA method is that the shape parameter ψ and shape-dependent strain relation tensor T are hard to determine when the architecture and microstructure of a composite is unknown or difficult to describe.

After the C^4 material, three-dimensional periodic architecture composite can be created by robotic deposition. Liquid metal infiltration of this structure resulted in an Al_2O_3-Al interpenetrating phase composite exhibiting low thermal expansion of 8.9×10^{-6} K^{-1}, and high compressive strength at 700MPa [61]. In addition to Al-Al_2O_3 IPCs, Cu-Al_2O_3 IPCs have also been considered via finite element analysis. Based on the microstructure of Cu-Al_2O_3 composite shown in Figure 2-10, Poniznik *et al.* [62] built a cubic representative element which consists of a prescribed number of voxels where each voxel is represented by an eight-node brick element.

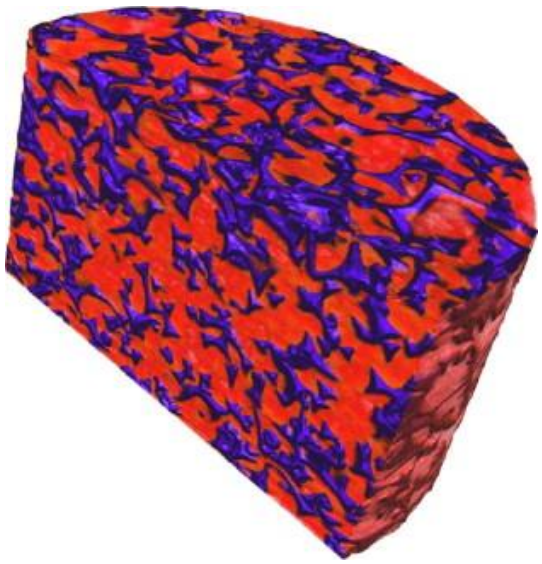

Figure 2-10. Microstructure of Al_2O_3–Cu composite, X-ray CT scan: dark phase - copper, light phase - alumina [62].

To build this representative element, material properties of the reinforcement phase were assigned to a certain amount of randomly selected elements corresponding to its phase volume fraction, while other elements were related to matrix, as Figure 2-11 (a) shows. Xie *et al.* [63] developed another approach which characterize the realistic microstructure of IPC in a more precise way comparing to the work done by Poniznik *et al.* [62], as Figure 2-11 (b) shows. Calculation of the elastic properties of those finite

element models presented good results in between Hashin-Shtrikman upper and lower limits [62,63].

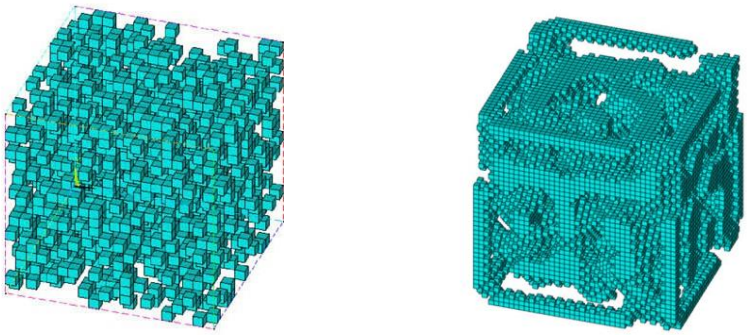

(a) (b)

Figure 2-11. (a) chosen elements for a phase with 20% volume fraction (b) random model for Cu-Al_2O_3 interpenetrating composite [62,63].

Furthermore, reactive metal penetration (RMP) in two subsequent steps was used to prepare intermetallic-ceramic composites with co-continuous structure. It has been reported that an NiAl(Si)/Al_2O_3 interpenetrating composite was obtained via RMP and showed mechanical properties (Young's modulus, density, coefficient of thermo expansion) better than Al/Al_2O_3 composite mentioned before [64].

In addition, triply periodic minimal surfaces (TPMS) are introduced to establish IPC structures via multi-material additive manufacturing. In general, the most appealing TPMS are those having cubic symmetry, as they can be repeated in 3D space and can be viewed as building blocks for any desirable geometry while maintaining periodicity. In nature, minimal surface topologies usually exist as interfaces separating two sub volumes. Thus, TPMS are used to separate cubic RVEs to build two-phase interpenetrating phase composites. Al-Ketan *et al.* [65] studied the mechanical properties of IPCs constructed by different TPMS topologies, as Figure 2-12 (a) and (b) shows.

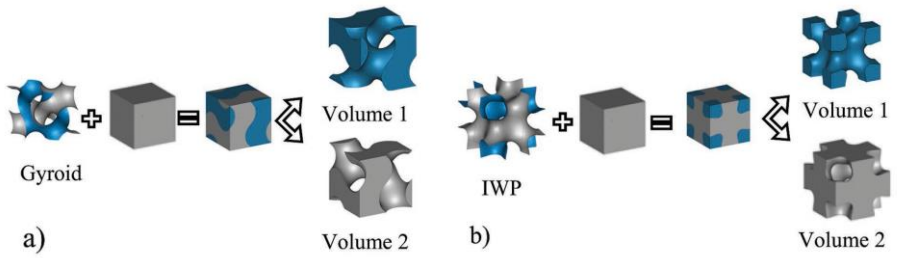

Figure 2-12. Gyroid surface splits the space into two identical volumes a) Gyroid and b) I-graph and wrapped package-graph (IWP) surface splits the space in two nonidentical volumes [65]

The comparison of mechanical properties (Young's Modulus, maximum strength, yield strength and toughness) of the TPMS IPCs and idealized simple hollow structure IPCs with 15% volume fraction of the reinforcement phase showed that TPMS IPCs outperforms the idealized IPCs. However, the connecting part of idealized simple reinforcement structure are with sharp connection edges, which is not considered a well-designed IPC structure. The comparison target of this work may have the potential to be improved in terms of the mechanical properties. Al-Ketan *et al.* [66] presented another work of the mechanical properties of periodic IPCs assembled by means of dividing the space by TPMS. Additional TPMS IPC structures were tested and similar conclusions were drawn. However, the idealized simple hollow structure remains the same. It could be better if reasonable non-TPMS structures were constructed and compared to determine which structure performs better. Abueidda *et al.* [67] presented comparison of the uniaxial modulus between different TPMS foams as Figure 2-13 and Figure 2-14 shows. IPCs can be constructed based on those TPMS foams. The other researches done by Abueidda *et al.* [67–70] focused on the electrical and thermal conductivity of TPMS IPCs.

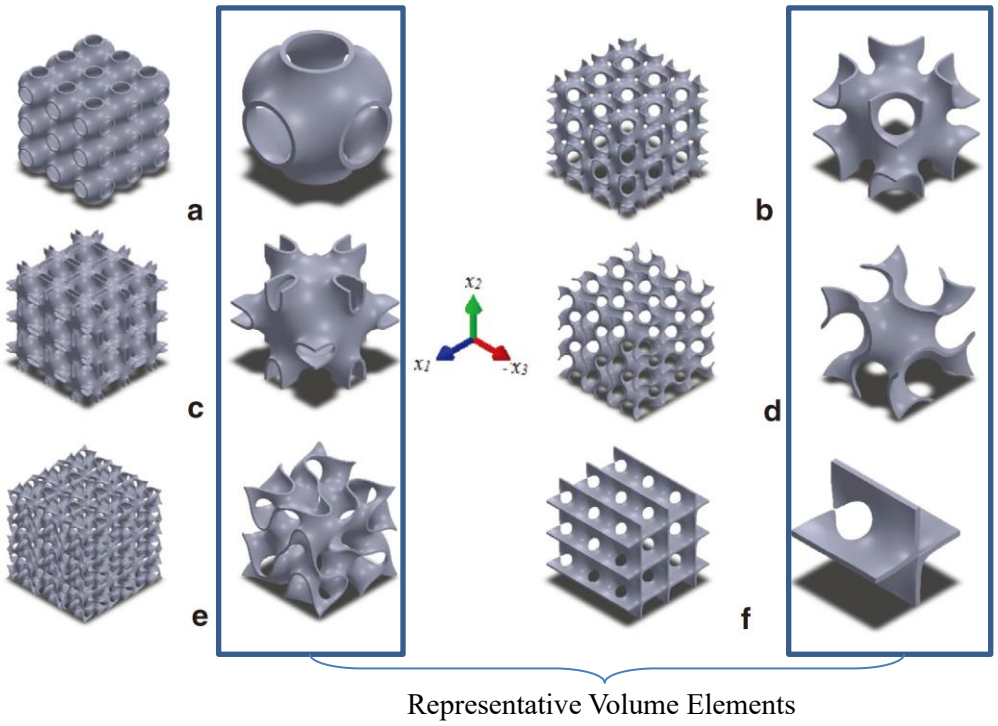

Figure 2-13. Architectures of foams that are based on TPMS; (a) Primitive, (b) IWP, (c) Neovius, (d) Gyroid, (e) Fischer-Koch S, (f) Crossed layers of parallels (CLP). The pictures on the left show the three-dimensionally repeated unit cells while the pictures on the right represent the unit cell of the structure [67].

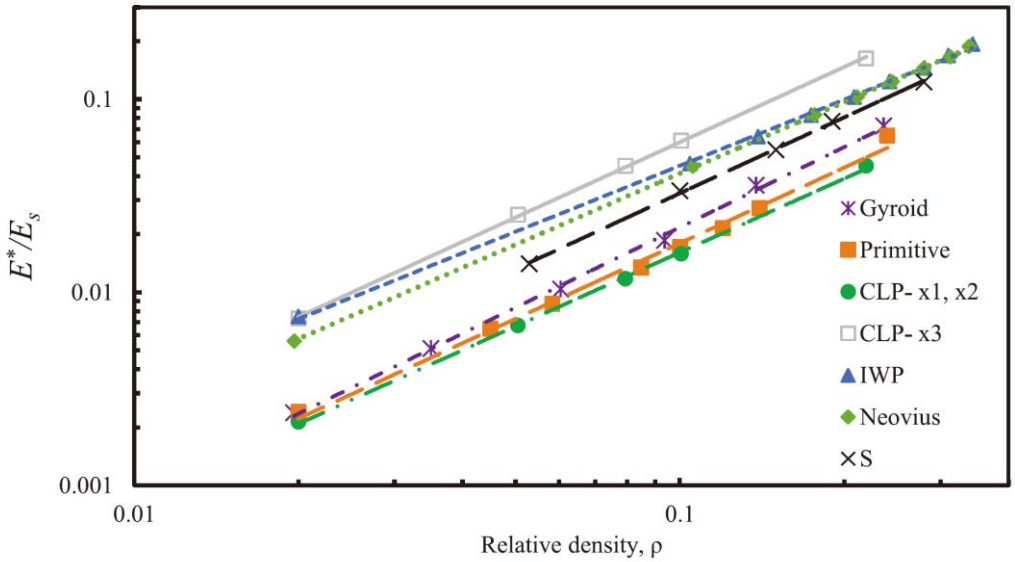

Figure 2-14. Uniaxial modulus of TPMS-foams at varying relative density [67].

The results of FE analysis and experiments showed that the conductivity of TPMS IPCs are superior than that of particulate-reinforced composite, while the difference of averaged conductivity k_{avg} between the simple cross-cubic fibre IPC structures and TPMS IPCs is small.

Polymers are also widely used materials as both reinforcement and matrix for interpenetrating composites. Interpenetrating polymer network (IPN) is a combination of two or more polymers in network form [71]. L. H. Sperling has done encyclopaedic documentaries of IPNs including synthesis, properties and applications [72,73].

Notably, it has been found as a breakthrough that the Young's Modulus of a composite can substantially exceed the Voigt limit, which had long been regarded as the upper limit of stiffness of isotropic composite materials [74,75]. It was theoretically proved that with specific structure, the Young's Modulus of the composite are largely affected by the Poisson's ratio combination of the constituent materials, as Figure 2-15 shows [74]. Furthermore, Poisson's ratio of IPCs can be designed at a desired value, e.g. positive, or negative, or zero [74,75]. In addition, it was predicted that with proper cross-cubic structure, interpenetrating composite have achieved a conductivity which almost reaches the highest possible theoretical upper limit [76]. Coefficient of thermal expansion of interpenetrating composites could be significantly larger than the maximum possible value as well [77].

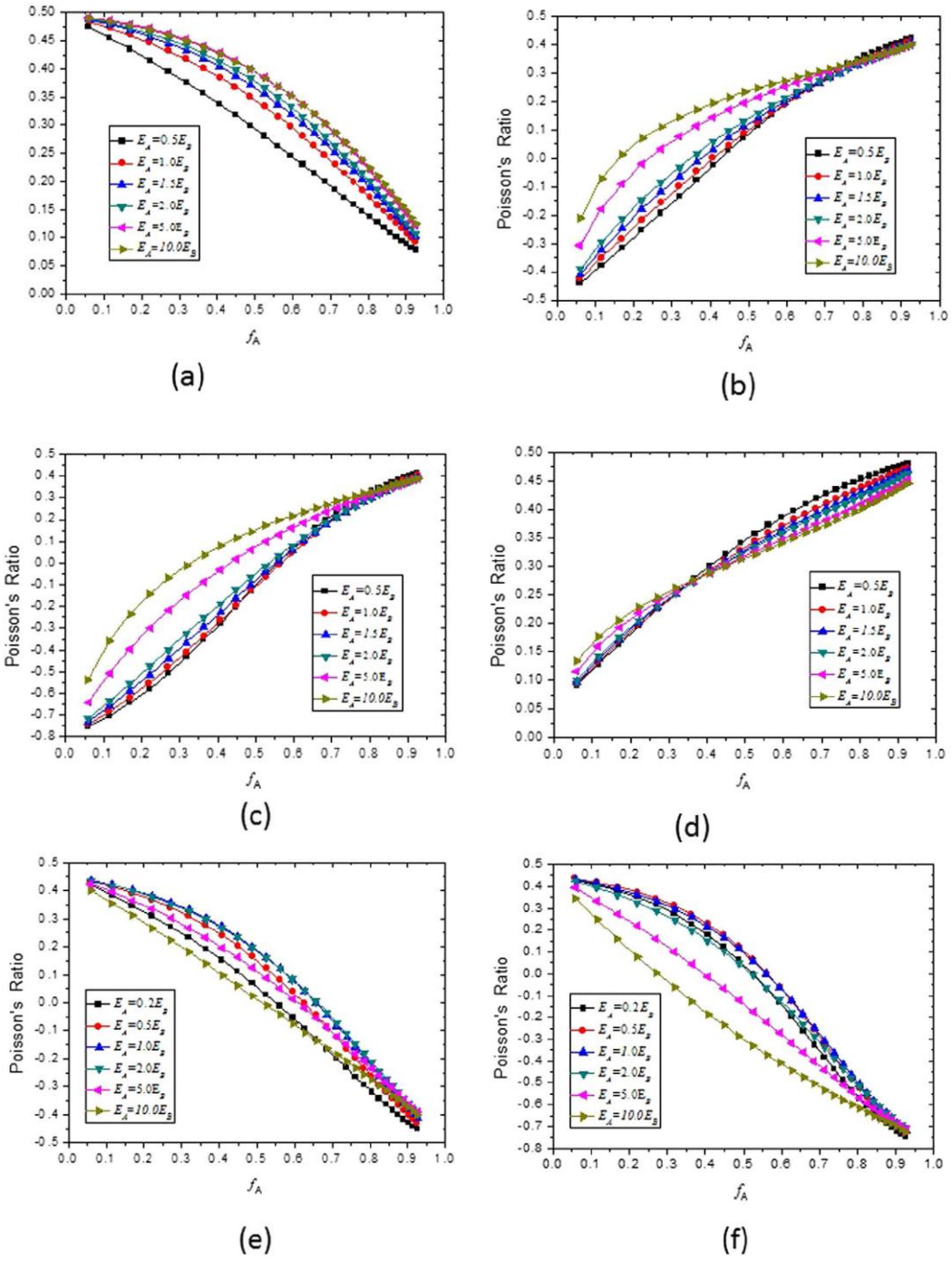

Figure 2-15 Effects of the value of $/E_A/E_B$ on the relationship between the normalized Young's modulus of the composites and the volume fraction of material A: (a) $\nu_A = 0.05$ and $\nu_B = 0.495$; (b) $\nu_A = 0.45$ and $\nu_B = -0.5$; (c) $\nu_A = 0.45$ and $\nu_B = -0.8$; (d) $\nu_A = 0.495$ and $\nu_B = 0.05$; (e) $\nu_A = -0.5$ and $\nu_B = 0.45$; (f) $\nu_A = -0.8$ and $\nu_B = 0.45$ [74].

2.2 Auxetic behaviour and auxetic materials

The classical theory of elasticity [78,79] shows that the Poisson's ratio of an isotropic material could be in the range $-1 < \nu < 0.5$. However, everyday experience tells us that when we stretch a material, the material not only becomes longer in the direction of stretch but also becomes thinner in cross-section. Similarly, a material under compression usually expands. In both these cases the behaviour of the material under deformation is governed by one of the fundamental mechanical properties of materials, the Poisson's ratio (υ). Poisson's ratio has long been regarded as positive and a range between 0 and +0.5 are given as the range of Poisson's ratio in most of the classical and modern textbooks [80]. Although a few single crystal materials, e.g., pyrite [78] and cadmium [81], are found to exhibit negative Poisson's ratio, they are not isotropic. Isotropic material with a negative Poisson's ratio had been veiled in secrecy for many years until 1987 when an cellular/porous material was produced and tested under compression by Lakes, showing a Poisson's ratio around -0.6 to -0.7 [82]. After that, auxetic behaviour has also been found in different structures. A schematic diagram of positive and negative Poisson's ratio deformation is shown in Figure 2-16.

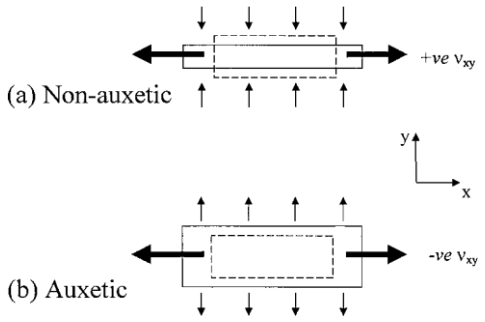

Figure 2-16. Schematic diagram of positive and negative Poisson's ratio deformation. a) Non-auxetic behaviour in which an initially undeformed material undergoes longitudinal extension and lateral contraction for a tensile load applied in the longitudinal (x) direction. b) Auxetic behaviour in which an initially undeformed material undergoes longitudinal and lateral extension for a tensile load applied in the longitudinal (x) direction.

In contrast to the general cognition that negative Poisson's ratio is rare in crystalline solids, 69% of cubic elemental metals exhibit auxetic behaviour when stretched along the [1 1 0] direction [83]. Several idealized zeolites and molecular structures are found

to possess a negative Poisson's ratio, and have been explained by their geometry and deformation mechanisms [84,85]. Silicon dioxide (SiO_2) in the α-cristobalite structure exhibits a negative Poisson's ratio averaging around -0.16 [86]. Negative Poisson's ratio behaviour is also found in tension deformation experiment of a natural layered ceramic. This auxetic behaviour enhances the deformation capacity by about one order of magnitude [87]. Single layered graphene ribbons [88], 2D puckered structure of PdSe2 monolayer [89], nanolayered graphene/Cu composites [90] also show negative Poisson's ratio under uniaxial load. Very large Poisson's ratio (from -5 to -11) has been observed in the thorough-thickness direction in highly porous fibre networks made of 316L fibres [91]. However, all the aforementioned materials are either cellular/porous or highly anisotropic materials. Poisson's ratio has attracted more and more attention in recent years. With the advance in materials syntheses, experimental measurements and computational simulations, it has been recognised that Poisson's ratio is related to the densification, connectivity, ductility and the toughness of solid materials. It has also been found that the elastic properties as well as ductility of a composite material can be largely affected, thus tuned by the Poisson ratios of different phases [74–76]. Cellular materials are often used as filler in sandwich structures. Compared to the conventional foam fillers, auxetic materials with a negative Poisson's ratio can enhance the stiffness [74,75], indentation resistance [92,93], crashworthiness, energy absorption performance [94,95], and fracture toughness [96] of sandwich structures. Greaves et al. [97] presented a numerical window of Poisson's ratio from -1 to 0.5 as a function of the ratio of bulk

and shear moduli and located the position of a wide range of materials, as Figure 2-17 shows. On the right side of the figure locates the compact materials such as liquids and rubbers where stress primarily results in shape change, their Poisson's ratio ν closes to 0.5. For most well-known solids such as metals, polymers and ceramics, 0.25 < ν < 0.35. Generally, glasses and minerals are more compressible and exhibits a Poisson's ratio around 0 to 0.2.

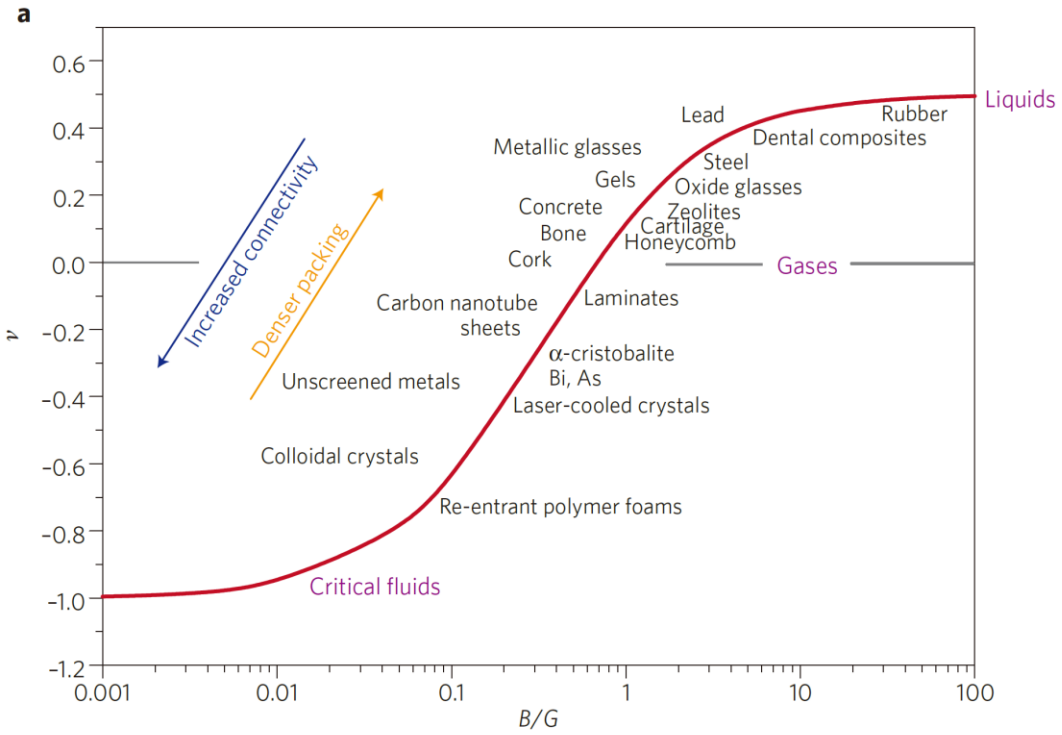

Figure 2-17. Numerical window of Poisson's ratio ν, from -1 to 0.5, plotted as a function of the ratio of the bulk and shear moduli B/G for a wide range of isotropic classes of materials [97]

Research of negative Poisson's ratio materials was initially supported by NASA and Boeing for aviation and aerospace applications [98,99]. Further investigation into the auxetic behaviour proved that many features of negative Poisson's ratio materials are desirable in aerospace industry [100,101]. Textile industry utilizes negative Poisson's ratio structures with their new knitting techniques to fabricate functional clothing, home

ware and medical textiles [102–105]. Auxetic materials attract car manufacturers for their better crashworthiness performance. Military and biomedical industry showed their interest in negative Poisson's ratio materials as well [106,107]. Conventional honeycombs [108,109] and open-cell foams [110], which have a positive Poisson's ratio under small deformation, can also exhibit a negative Poisson's ratio (i.e., auxetic behaviour) under large strain compression because of cell junction/vertex rotation.

Most fabricated materials with a negative Poisson's ratio are porous in macro or micro scale, with relatively low stiffness, which may limit their applications to low load-bearing structures. When high stiffness/weight ratio, strength and energy absorption are all demanded, composite materials may be a good choice. Compared to the conventional particle reinforced and unidirectional fibre reinforced composites [111–114], interpenetrating phase composites (IPCs) reinforced by a self-connected network rather than by separated particles or fibres, have been demonstrated to have much better mechanical and physical properties [1,56,60,75,76,115] than those of their conventional counterparts. Therefore, the fabrication of auxetic IPCs should be a good choice to overcome the defects of single negative Poisson's ratio materials.

2.2.1 Auxetic structures and mechanisms of auxetic behaviour

After three decades of research, the mechanism of auxetic materials are summarised in different alternatives. The microstructure of re-entrant foams was captured in Lakes' continued work [116] in 1988, as Figure 2-18 (b) shows. For comparison, microstructure of the conventional polyester foam is also presented in Figure 2-18 (a).

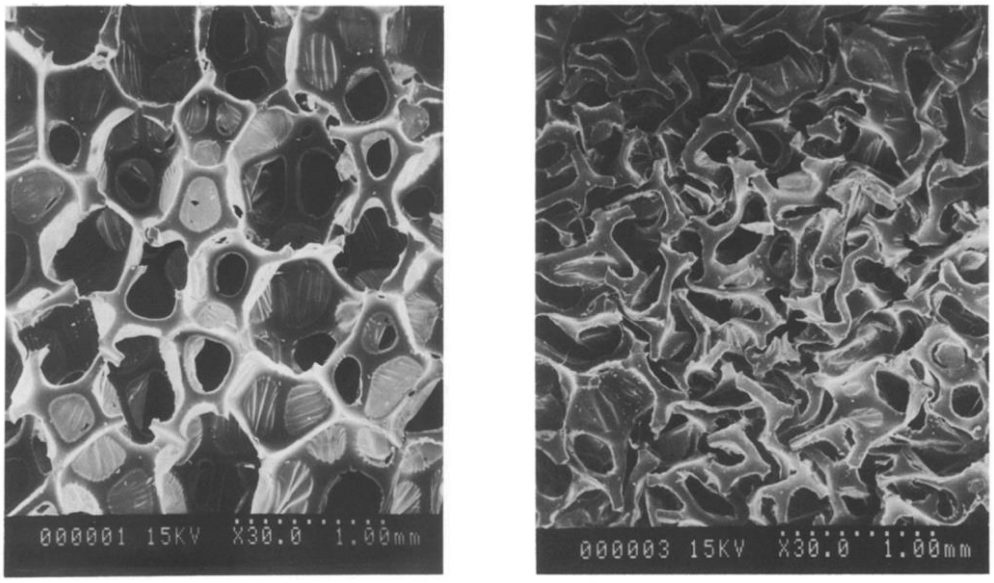

(a) (b)

Figure 2-18. (a) Scanning electron micrograph (SEM) of conventional polyester foam. (b) Scanning electron micrograph of re-entrant polyester foam [116].

The unit cell of a conventional polyester foam was idealized as a typical structure of tetrakaidekahedral (14-sided) cell, while the re-entrant foam was produced by symmetrical collapse of a 24-sided polyhedron with cubic symmetry, as Figure 2-19 shows. When the re-entrant foam is pulled uniaxially, the other side expands because of the concavity of the structure. Lakes found that the auxetic behaviour does not require a large cellular structure or depend on the structure size. In principle, materials with microstructure on a scale smaller than 1μm could exhibit a negative Poisson's ratio [82]. The Poisson's ratio reaches -0.7 for Lakes' re-entrant foam. However, as an open cell foam, the re-entrant foam only has a Young's modulus around 72kPa, which may limit its applications.

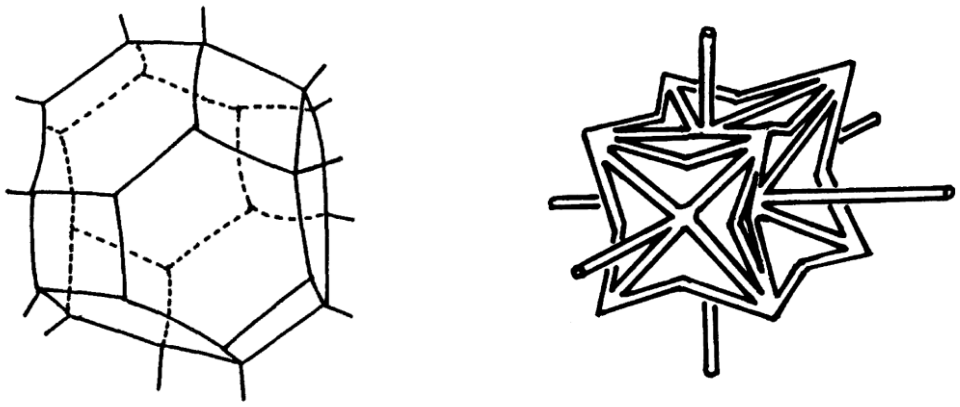

(a) (b)

Figure 2-19. (a) Idealized unit cell of conventional foam. (b) Idealized unit cell of re-entrant foam [116].

Meanwhile, the well-known material polytetrafluoroethylene (PTFE) was found to have negative major Poisson's ratio. A microporous, anisotropic form of expanded polytetrafluoroethylene exhibited negative major Poisson's ratio as large as -12 [117]. The microstructure and mechanism of this behaviour was observed by SEM photograph and schematically drawn as Figure 2-20 shows. When tensile strain was applied, the micro rotation of the nodes led to an auxetic behaviour of expanded PTFE.

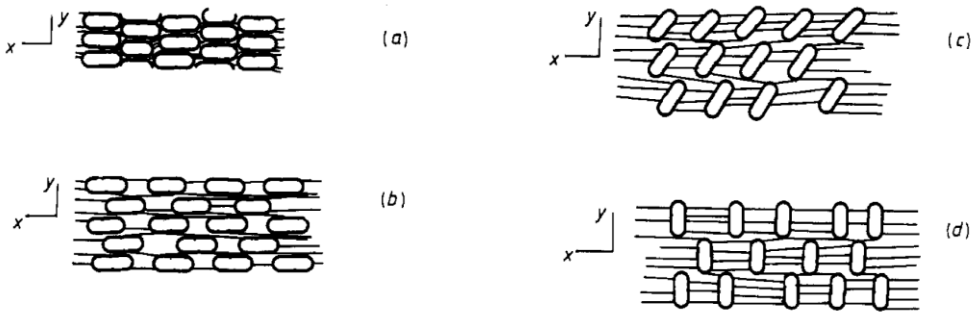

Figure 2-20. Schematic diagram of structural changes observed in microporous PTFE undergoing tensile loading in the x direction. (a) Initial densified microstructure. (b) Tension in fibres causing transverse displacement of nodes and lateral expansion. (c) Rotation of nodes producing further lateral expansion. (d) Fully expanded condition

In 1992 Yeganeh-Haeri *et al.* revealed that a naturally existed material, α-cristobalite of crystalline silicon dioxide is auxetic [86]. A tetrahedral rotation framework was established to illustrate the mechanism of the auxetic behaviour of the SiO_4 in atomic structure level. With one oxygen atom at each of the four corners surrounding a Si atom, each oxygen atom is shared between two SiO_4 tetrahedral units. The rotation of a 3×3×3 SiO_4 unit cell is shown in Figure 2-21. In addition, zeolites share similar mechanism when exhibiting negative Poisson's ratio [84,118]. The 2D rotating hinged triangle and square structures are shown is Figure 2-22.

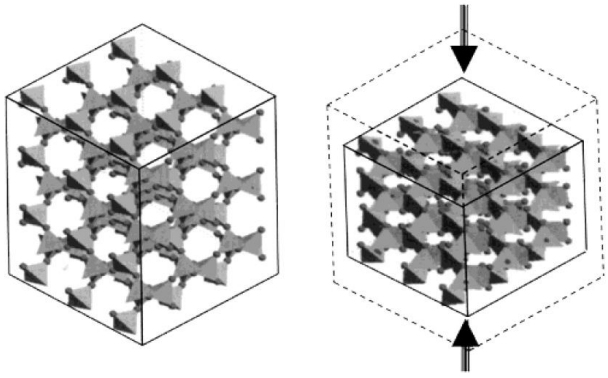

(a) (b)

Figure 2-21. Auxetic behaviour of a 3×3×3 unit cell of SiO_4 caused by tetrahedral rotation (a) fully expanded. (b) fully compressed [80].

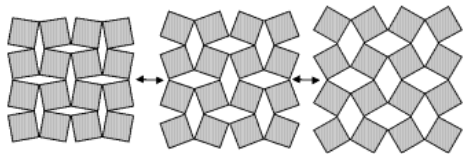

(a)

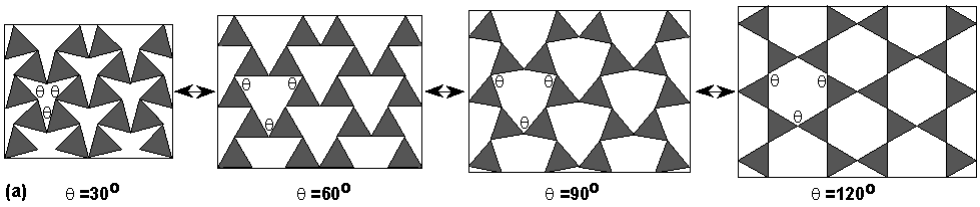

(b)

Figure 2-22. Schematic illustration of the mechanism of auxetic zeolites: (a) Hinged rotating

triangles; (b) Hinged rotating rectangles [84].

Conventional 2D hexagonal honeycomb could also exhibit zero or negative Poisson's ratio in one direction [119]. The microstructures of positive, negative and zero Poisson's ratio hexagonal honeycomb is illustrated in Figure 2-23.

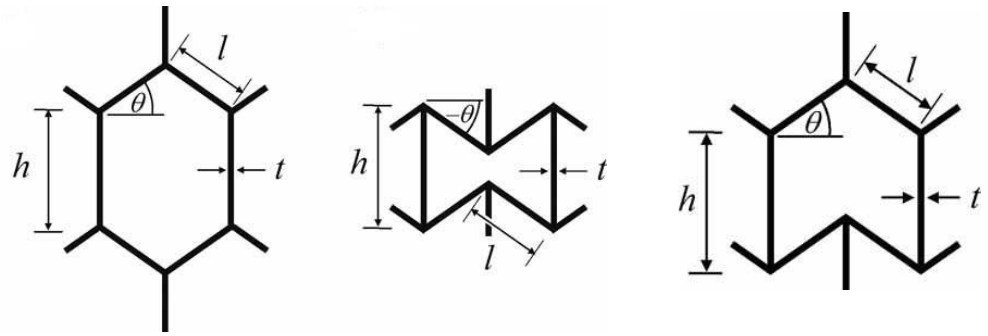

(a) (b) (c)

Figure 2-23. The hexagonal honeycomb geometries: (a) conventional non re-entrant form (b) auxetic re-entrant form (c) semi re-entrant form [119].

Additionally, lots of different auxetic structures are found or fabricated to achieve a negative Poisson's ratio material. 2D re-entrant triangular [120], 3D re-entrant variant structures [121,122], re-entrant star and its variants [123], and different hinged rotating structures [124–127] are all feasible microstructures for negative Poisson's ratio materials. Figure 2-24 provides an overview of the other auxetic structures stated.

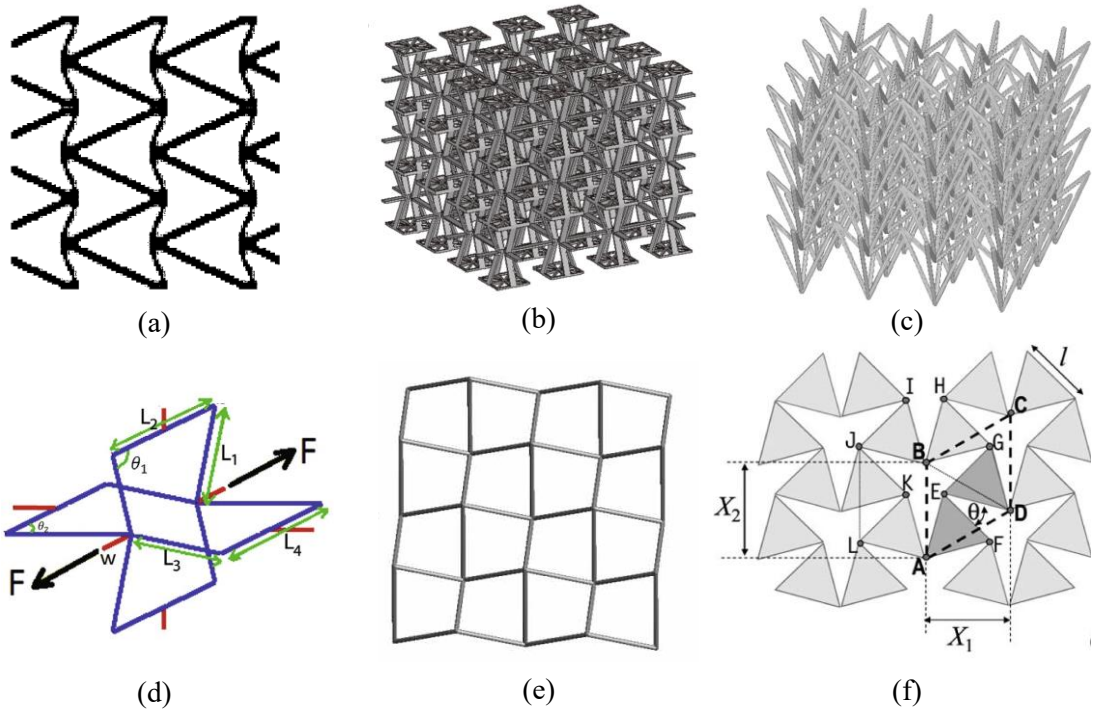

Figure 2-24. Microstructure of different negative Poisson's ratio materials: (a) 2D re-entrant triangular. (b) (c) (d) 3D re-entrant variants. (e) re-entrant star variant. (f) hinged rotating structures [120–127].

Besides, macro scale auxetic structures as Figure 2-25 shows are used in reactor cores in some nuclear reactors. The structure was designed to withstand the horizontal components of the forces generated during an earthquake, whilst also allowing free movement of the structure to accommodate differential thermal movements between the graphite core and steel supporting/restraining structures at the edges of the core [128].

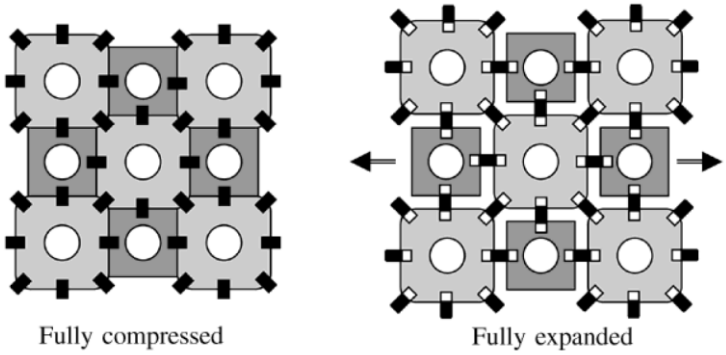

Figure 2-25. Schematic of the horizontal plane of a radially keyed graphite brick moderator core of a Magnox nuclear reactor. Auxetic behaviour occurs due to radial movement of the free-standing columns of graphite bricks [128].

The auxetic behaviour has also been explained in the molecular level. Evans et al. designed a 'reflexyne' molecular network model in 1991 to illustrate the negative Poisson's ratio of materials observed in naturally occurring materials and fabricated re-entrant foams [129]. This was the first attempt at designing a material that demonstrates a negative Poisson's ratio owing to mechanisms acting at the molecular level. After that, self-expanding molecular networks were modelled through force-field based simulations [130]. The molecular lever auxetic behaviour was explained by the same mechanism of hinged rotating triangles. Near zero Poisson's ratio behaviour of a series of polyphenylacetylene network were explained by different honeycomb molecular networks [131]. The 'egg rack' structure as Figure 2-24 (e) shows is also considered in molecular level. The calix[4]arene subunits can be constructed as 'double calix' molecular networks, which share same mechanism as the 'egg rack' structure [132]. The elastic properties such as in-plane and out-of-plane Poisson's ratios and Young's moduli of calix[4]arene networks were predicted and the Poisson's ratio was as small as -0.8 [133]. Figure 2-26 gives a representation of molecular networks designed to exhibit auxetic behaviour. The in-plane mechanical properties of different types of two-dimensional molecular networks with auxetic potential were characterised [123]. The comparison showed that two-dimensional poly-triangles and the poly-calixes are effectively more auxetic than those based on 2D re-entrant models.

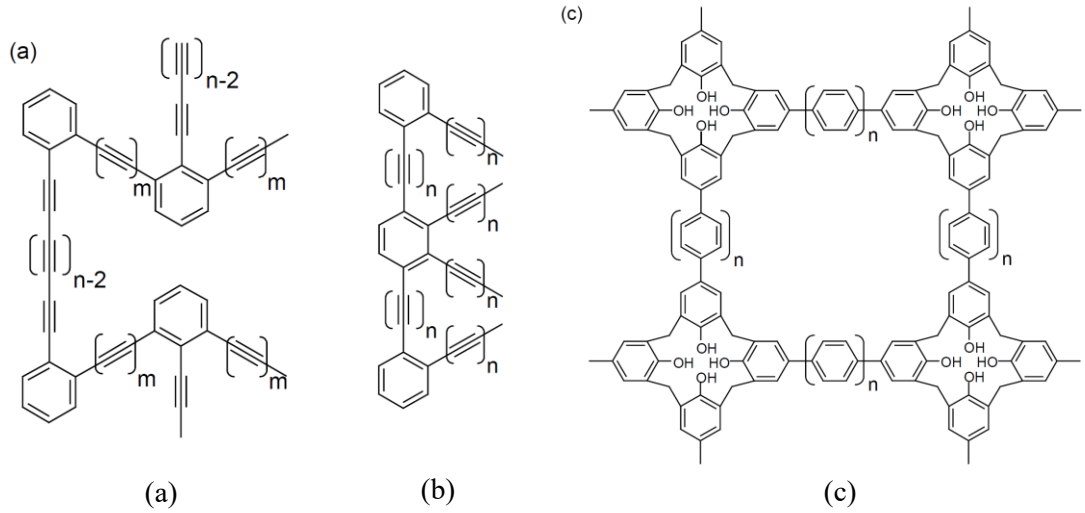

Figure 2-26. Two-dimensional molecular networks designed to show auxetic behaviours [123].

2.2.2 Auxetic composite materials

Although auxetic materials with a negative Poisson's ratio can enhance the stiffness [74,75], indentation resistance [92,93], crashworthiness, energy absorption performance [94,95], and fracture toughness [96] compared to conventional open foams, most of the auxetic materials with easy access are porous materials. The relatively low stiffness and strength of porous foams excluded porous auxetic materials from the applications used for load-bearing structures and tough conditions. The auxetic structure based on re-entrant foams are always weak in shear. As a particular kind of auxetic materials, the development of auxetic composites has currently attracted great attentions due to their wonderful properties as compared to porous auxetic foams and non-auxetic composites. Auxetic composites has been used in aerospace, automotive industry and protection gear (such as helmets and cushions) [80]. Milton [134] suggested a group of two-phase composite materials designed with different layer methods of multiscale laminates. Chen and Lakes [135] used re-entrant copper foam as the matrix with viscoelastic elastomer, solder and indium as the filler materials to produce auxetic composites. Alderson *et al.* [136] paved two different ways of auxetic composite manufacturing. One of them was to produce auxetic composite materials

with appropriate laminates configurations of conventional materials and another was to produce single fibre composites use auxetic fibres. With the development of materials productions, auxetic fibre networks were used to reinforce the conventional matrix materials such as polymers and metals. It was confirmed that composite with negative Poisson's ratio can be produced by infusing auxetic stainless steel mats with a polymer and the ratio of reinforcing network stiffness to matrix stiffness was sufficiently high [137]. Zhou *et al.* [138] fabricated a kind of auxetic composites by injecting polyurethane (PU) resin to a mould containing auxetic textile structure and compared the compression behaviour of the auxetic textile composite with non-auxetic composites made from the same materials and dimensional parameters. However, they discovered that the auxetic composite behaved more like a damping material with a lower range of compression stress, while the non-auxetic composite behaved more like a stiffer material with a higher range of compression stress. In addition, a finite element analysis of the auxetic textile composite has been done by the same research group and matched the experiments well. The finite element analysis shows that the auxetic behaviour of the 3D auxetic textile structure increases with increasing compression strain [139]. Composites with elliptic inclusions exhibited auxetic effect with relative lower Young's modulus compared with the non-auxetic composites as evidenced by the finite element analysis [140]. Additive manufacturing and rapid prototyping techniques enable us to fabricate complex topologies of architectures of cellular materials in a precisely controlled and ordered way rather than randomly generated architectures by metallurgy or synthesis, as Figure 2-27 shows [141]. Schwerdtfeger *et al.* [142] build typical re-entrant foam structures via selective electron-beam melting (SEBM) which allows the direct translation of CAD models to real world objects. The following test showed that the Poisson's ratio of the auxetic behaviour direction of the specimen was around -0.2. Samples of chiral honeycombs are also produced and tested with two different types of materials, by two different models of Rapid Prototyping machines [143]. Additive manufacturing has also become an alternative to fabricate polymer matrix composites [144]. Thereafter, the advantage of additive manufacturing and rapid prototyping was taken to create auxetic composites. Re-entrant auxetic structure were

made by rapid prototyping method with 316L-0407 austenitic stainless-steel alloy. The metal auxetic structures were then filled by gelatine and polyurethane fillings. It has been proved by experiment that the filler could affect the impact resistance and absorption capabilities [145]. Li *et al.* [146] fabricated re-entrant honeycomb and chiral truss lattice composite by 3D-printing. The two constituents of the auxetic composites are VeroWhite and TangoPlus. It is found that the auxetic lattice reinforced composites exhibited enhanced stiffness and energy absorption under uniaxial compression.

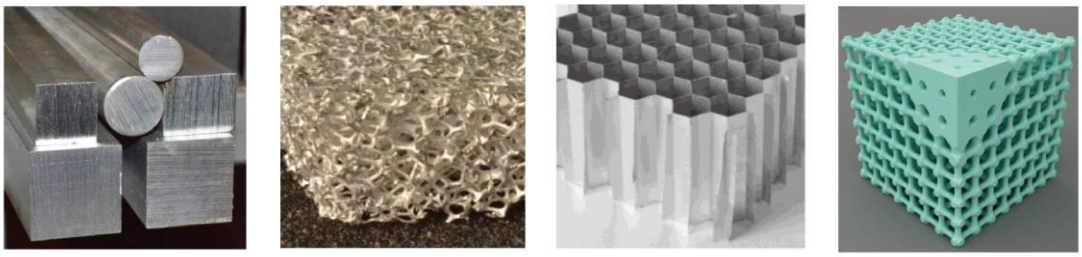

(a) (b) (c) (d)

Figure 2-27 Architecture of the materials. (a) None. (b) Random. (c) Ordered. (d) Ordered and location specific.

When a self-connected auxetic lattice structure or fibre-network is embedded as reinforcement in a matrix with a low positive Poisson's ratio, the composite would have the potential to exhibit auxetic behaviour. It has already been experimentally demonstrated that composites reinforced by an auxetic fibre-network exhibits a negative Poisson's ration in the thickness direction [137]. Composites reinforced by a re-entrant hexagonal honeycomb are also found to exhibit strong in-plane auxetic behaviour [147].

2.3 Fibrous Materials

Fibrous materials can be defined as bulk materials made of large numbers of individual fibres [148]. Fibrous materials can be metals, polymers or ceramics. Researches on fibrous materials have been a hotspot for several decades started from the 1940s. The prediction of the physical and mechanical properties was regarded as a complex

question as the behaviour of fibrous materials is remarkably different from that of their constituent individual fibres. Parameters such as aspect ratio, fibre volume fraction, porosity, tortuosity and pore shape factor were introduced to generally describe a fibrous material. Fibrous materials can be two-dimensional structures and three-dimensional solids such as corks and bones. Fibrous materials are widely used in packaging, textiles, insulation, lightweight structures, and acoustic resonances dampers [149,150]. Furthermore, fibrous materials are also used as the reinforcements in composites. Fibre networks are a kind of specific fibrous materials in which fibres are connected with each other. Composites reinforced by fibre networks with a proper method could be interpenetrating phase composites, as reviewed previously. A brief review of fibrous materials probably leads to a better understand of IPCs reinforced by fibre networks, especially randomly created ones.

2.3.1 Cellular fibrous material

Some of the fibrous networks possess regular architectures or microstructure cells. For example, 2D triangle cells and hexagon cells, 3D tetrahedron and tetradecahedrons are found in fibrous materials. Some of them consist of random cells such as Voronoi cells and Delaunay cells. Gibson and Ashby [151] gives a comprehensive overview about the researches done in the domain of structures, physical properties and mechanical properties of cellular solids. The regular or random cells in these kinds of composites can be regarded as tessellations of 2D or 3D spaces. Triangle, squares and hexagons can tessellate a 2D area. In the same way 3D space can be partitioned by tetrahedron and tetradecahedrons. For random tessellation methods, hyperplane tessellation, STIT tessellation (tessellations that are stable under iterations) and Poisson-Laguerre tessellation are applied to the modelling of cellular materials other than Voronoi tessellation. All these four methods can tessellate both 2D and 3D spaces, schematic illustrations of 3D cubic RVE tessellations are shown as Figure 2-28 [152]. Random mosaic tessellation [153] and Gilbert tessellation [154] can also be applied to create random fibre network models. The mechanical behaviour of cellular materials are

investigated based on these models, e.g. Redenbach [155] utilized Laguerre tessellations generated by random sphere packings to describe the geometric structure of cellular material. Zhu et al. did a series of research on the open foams with hexagon, tetrakaidecahedral cells and Voronoi cells [156–158]. An elliptical yield function was found to fit the predicted yield surfaces of imperfect 2D hexagon and Voronoi foams [159].

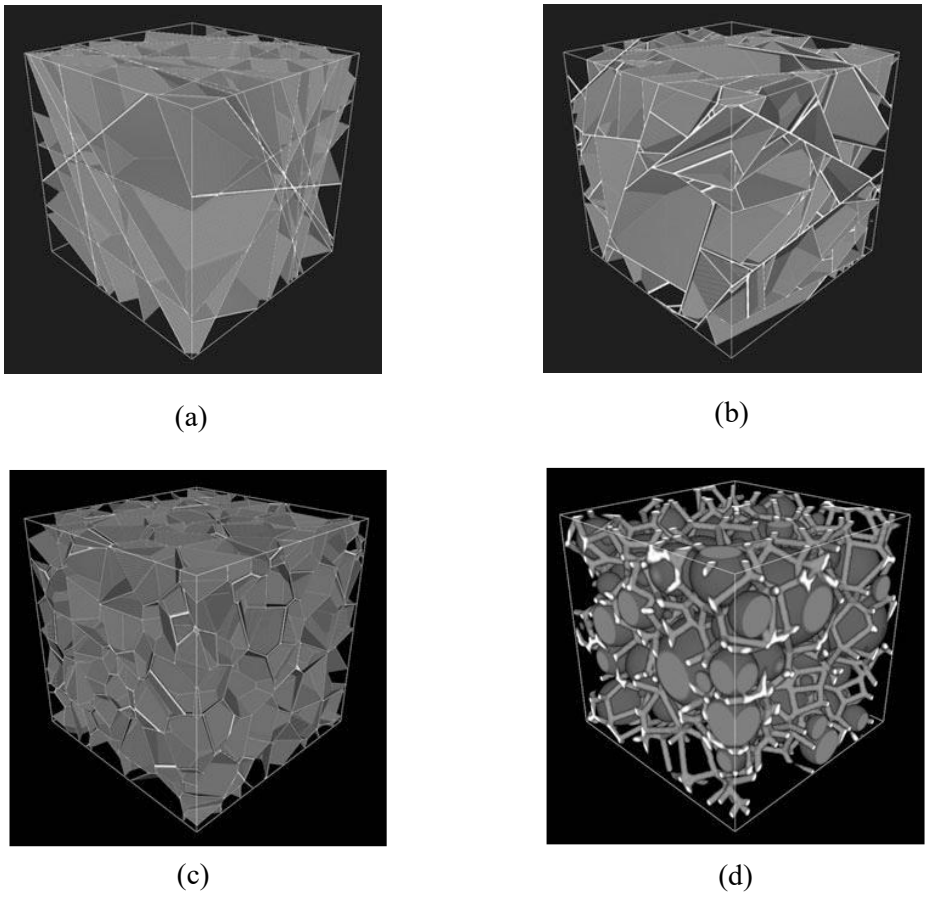

Figure 2-28. Tessellations of 3D RVEs to model the structure of cellular materials: (a) hyperplane tessellation (b) STIT tessellation (c) Voronoi tessellation (d) Poisson-Laguerre tessellation [152].

2.3.2 Stochastic fibrous material

Stochastic architectures or microstructures also widely exist in fibrous materials. A significant difference between cellular fibrous materials and stochastic fibrous material in the microstructures can be observed in Figure 2-29 [160]. The fibres in cellular

fibrous materials are connected to each other by joints (stronger in cross section compared with that of the fibres) at the end of the fibres, while the fibre in stochastic fibrous materials are connect by overlaps of the fibres and cross-links between the fibres.

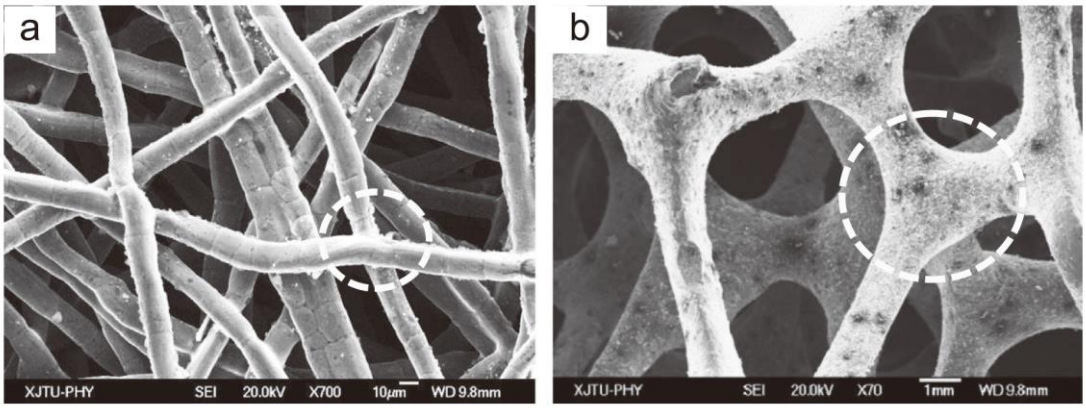

Figure 2-29. Comparison of the microstructures of (a) a metal fibre sintered sheet with fibre diameter 12μm and relative density of 23% and (b) an open cell aluminium foam [160].

Study of the mechanical properties of stochastic fibrous materials began from investigating the compressibility of wool [161]. After that, Cox pioneered to predict the elastic behaviour of papers based on the distribution and mechanical properties of the constituent fibres [162] in 1952. Papers may to some extent be the most common stochastic fibrous material used in our daily life, which is a bonded planar random fibre network and are deeply researched. Kallmes [163–166], Seth [167,168] and Page [169,170] have contributed a great deal to this field through their research work on properties of paper. They extended Cox's analysis by using probability theory to study fibre bonding points, the free fibre lengths between the contacts, and their distributions. Different natural fibrous materials have been studied for their advantages on the environmental and sustainable aspects over its synthesized counterparts which are difficult to recycle. Based on the origin of the natural fibres, those suitable for composite reinforcement can be grouped into leaf, bast, seed and fruit origin [171]. For example, sisal fibres are produced by sisal leaves and widely used in composite material industries. The mechanical properties [172] as well as degradation behaviour [173] and recyclability [174] of the sisal fibre and its composites were investigated. However, not

all the natural fibres can form a proper network. Sisal fibres are mostly used in unidirectional fibre reinforced composites. Only nanofibril networks around the neat sisal fibre can be formed by dipping process [175].

When it turns to artificial porous materials, metal fibre sintered sheets (MFSSs) are a typical kind of random fibre network with desirable mechanical properties as separation and filtration material where high temperatures, high pressures, and aggressive chemicals are present. MFSSs are widely used in petrochemical, common chemical industry, hydraulic filtration, pharmaceutical, and power generation. AISI 316L stainless steel fibres with diameters of 50 and 100 μm were compacted and sintered to prepare the specimens of metal fibre porous structures in Ducheyne's work [176]. The modulus of elasticity measured in compression was found to be close to the theoretical Mackenzie relationship and upper Hashin-Shtrikman bound [176]. Copper fibre can also be used to produce metal fibre sintered sheets. The unique four step fracture process and the relationship between the porosity and tensile strength is determined [177]. Jin et al. [178] developed a 2D stochastic beam model to investigate the in-pane elasto-plastic behaviour of metal fibre sintered sheets. In his work, a 2D random fibre network was generated by overlapping all the fibres with each other, which led to very strong bonding connection and thus high nodal connectivity between fibres. The simulation results showed that the in-plane Young's modulus and bulk modulus have a linear correlation with the relative density [178]. As the multilayer structure of porous fibre sintered sheets, MFSSs are transversely isotropic.

Chapter 3 Regular lattice structured interpenetrating composites

3.1 Introduction

As potential candidates of applications in need of high stiffness-weight ratio and/or tuned mechanical properties, different types of novel composite materials have been manufactured and investigated in depth. Compared to particle reinforced and unidirectional fibre reinforced composites, interpenetrating phase composites (IPCs) with interconnected network in reinforced phase rather than discontinuous structures are attractive for their enhanced mechanical and physical properties.

In general, the factor which could affect the mechanical properties of composites including geometrical lattice structure design, different mechanical properties combination for the constituent material (such as Poisson's Ratio and Young's moduli), interphase conditions between reinforcements and matrices. Periodic cells such as Kelvin cells (tetrakaidekahedron cell) have been widely used to represent the reinforcement phase of metal-metal interpenetrating phase composites. However, very little attempt has been made on micro-scale structural design aiming at finding the variations of mechanical properties with different microstructures of IPCs.

This chapter gives a numerical approach to explore how different lattice microstructures in IPCs affect the normalized elastic properties of the composites. Several periodical microstructures are modelled. Different types of IPC structures are considered via representative volume elements and periodic boundary conditions (PBCs). All the structures are numerically tested to find if their calculated Young's moduli can reach and exceed the Voigt limit with proper combinations of constituent materials. The volume fraction, moduli, and Poisson's ratios of the constituent materials are taken into consideration. Elastic properties of lattice structured interpenetrating composites are analytically acquired via finite element method. The elastic moduli of different IPC

structures are compared to experimental and theoretical approaches to validate the results. Those of the conventional particle and fibre reinforced composites are listed together.

3.2 Geometric structures

This chapter focus on the two-phase interpenetrating composites of which consist two homogenous and isotropic materials. Three different kind of composites are considered. The microstructure of the composites is supposed to be perfectly periodic, containing a large number of identical cubic cells. In FE analysis where time and memory consuming are sensitive, it is meaningful to describe the IPCs by a much smaller model, which is still large enough to include all the features and characteristics of the structure. The representative model is small enough on one hand for short calculation time and large enough on the other hand for fully describe the material. This smaller model is a representative volume element. In this case, the periodic cells are perfect candidates as RVEs. The different selections on the same structure are shown in Figure 3-1 as a cross-sectional view of the material structure. The cyan colour of material represents for the matrix while the magenta colour of material represents for the reinforcements. The In each cubic cell, the reinforced open foam structure is assumed to be reticular cylindrical struts latticed in three different patterns: (I) cross-cubic, (II) cross-cubic with space diagonals, (II) tetrakaidekahedral, while the matrix fills the RVE space other than the reinforcements, as shown in Figure 3-3. The method of existence and size determination of an RVE has been discussed during the research of particle model [179,180].

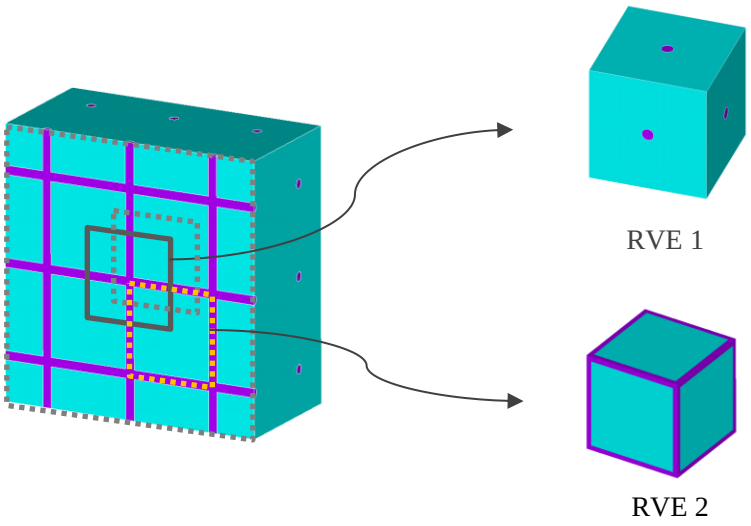

Figure 3-1. RVE1 selection of simple cubic lattice IPC.

The fibre network is constructed in ANSYS and added together with the conjunction spherical reinforce components. And then RVEs are constructed by Boolean operations as Figure 3-2 shows. Firstly, the fibre in an RVE is obtained by intersecting the fibre network from a solid cube in correct dimension and place. Then the matrix in the RVE is obtained by subtracting the fibre in the RVE from the same solid cube. Finally, these two entities are put together to form a complete RVE. The interface of the fibres and matrix is bonded together.

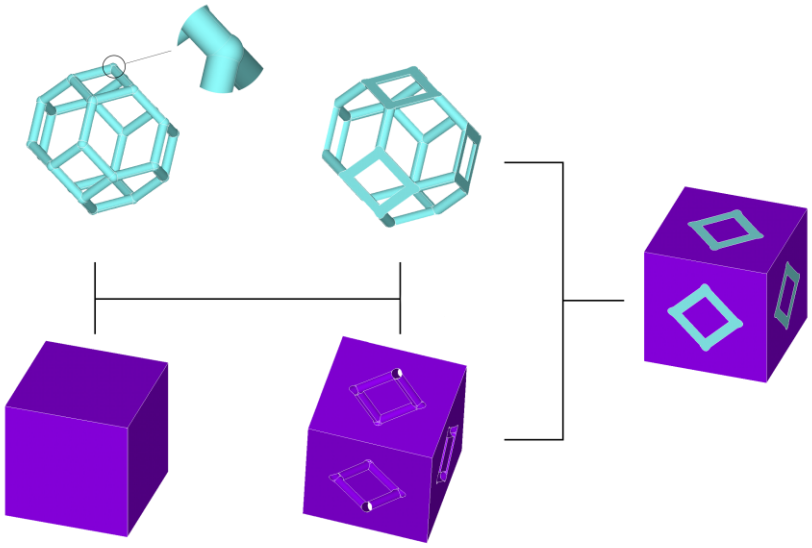

Figure 3-2. Boolean operation to build an RVE of regular IPC.

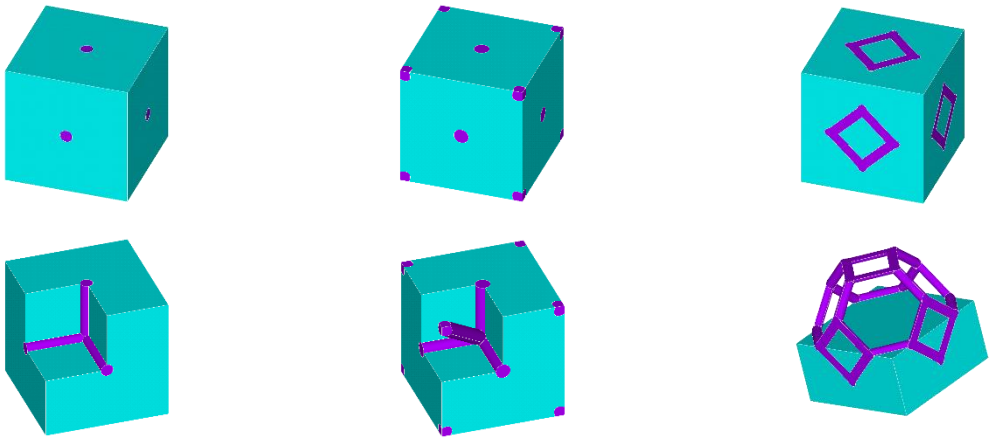

Figure 3-3. The geometrical structures of three different types of self-connected reinforcement composites: (a) Type I, (b) Type II, (c) Type III.

All the three cubic RVEs have an edge length L, and the diameter of the open-foam cylinders strut is d. By changing d, the different set of volume fractions can be obtained. The two phase of the interpenetrating composites RVEs are made from two isotropic materials. E_m, E_f, ν_m, ν_f represent the Young's moduli and Poisson's ratio of the matrix and fibre reinforcement separately. The volume fractions of the reinforcement and

matrix are denoted as VF_f and VF_m. The intersections of the rods are reinforced by spherical connections to simulation the crossing of micro lattice structures.

In order to predict the elastic performance of the composites by tracking how Young's Modulus of the composite E_c is affected by different constituent material properties and volume fractions. $E_m = 1$ is assumed for generality and simplicity. ν_m and ν_f are set to be with as much difference as possible in positive and negative range. Sets of E_f/E_m, ν_m and ν_f are listed in Table 3-1.

Table 3-1. Young's moduli and Poisson's ratios of constituent materials

E_f/E_m	2	2	10	10	2	2	10	10
ν_f	0.49	0.05	0.49	0.05	0.49	0.3	0.49	0.3
ν_m	0.05	0.49	0.05	0.49	-0.8	-0.8	-0.8	-0.8

For the volume fraction, it is obvious that $VF_f + VF_m = 1$. Thus, the volume fraction of the fibre is considered from 5% to the upper close of the geometrical limit of each structure Type. The diameter of fibres in Type I, II and III can be denoted as d_I, d_{II}, d_{III}. The geometrical fibre volume fraction limit of each structure type is given as the following equations.

$$d_I < L \tag{3.1}$$

$$d_{II} < \frac{\sqrt{2}}{1+\sqrt{2}} L \tag{3.2}$$

$$d_{III} < \frac{\sqrt{2}}{4} L \tag{3.3}$$

As the structure is complex especially in the cross parts of the fibres, it is difficult to mesh the whole RVE by rectangular prism or cuboid elements. Tetrahedral element are a reasonable choice for this kind of structures. The RVEs are meshed by 3D 10-node tetrahedral structural solid element SOLID187 in ANSYS. As it is proved that the

solving results of these simple regular models is not sensitive to the element sizes as long as the models can be solved without any shape elements in ANSYS, the size of the element *es* is set as a function of the fibre volume fraction as to ensure a balance of efficiency and calculation time. A piecewise function is created to describe how to determine the size of the element *es* according to the fibre volume fraction. At a given fibre volume fraction the fibre diameter can be calculated. If the corresponding fibre diameter to the fibre volume fraction is denoted in specific notation as $d_f = d_{fe} \times 10^k$. In specific notation $1 \leq |d_{fe}| < 10$, *es* is specified as

$$es = \begin{cases} floor(d_{fe}) \times 10^k, d_{fe} < 5 \\ 0.5, d_{fe} \geq 5 \end{cases} \quad (3.4)$$

The function *floor* is defined to round d_{fe} toward negative infinity. This can give an element size automatically with a given fibre volume fraction, thus accelerate the solving procedure of FE analysis. After mesh, the nodes on the interfaces of the fibres and matrix are merged as one single nodes. Besides, the nodes of each face of the RVEs are kept exactly the same in both number and positions for periodicity, as Figure 3-4 shows.

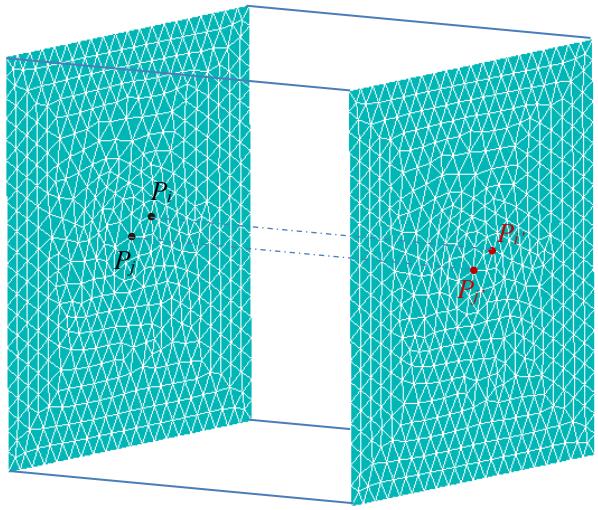

Figure 3-4. The two facets of an RVE with the exactly the same mesh pattern.

The length of the RVEs of three types of IPCs are $L = 10$.

3.2 Boundary conditions

An appropriate boundary condition is vital in numerical approaches to estimate the mechanical properties of materials. When a composite material is described via one representative volume elements, that means a single RVE can form the full material structure by periodically replicate itself. Thus, a matching boundary condition, namely, the periodic boundary conditions need to be applied to constraint the deformation behaviour of the RVE model. It has been suggested that periodic boundary conditions are more suitable than mixed boundary conditions and prescribed displacement boundary conditions for a periodic RVE [109,157,181]. A unified periodical boundary conditions for representative volume elements of composites was presented to predict the rhombohedral RVE models' elastic moduli for both unidirectional laminate and angle-ply laminates [182]. Any correctly defined RVE with different shapes can obtain the same mechanical properties with correct periodic boundary conditions. This has been proved by Xia's work [183] with two types of different RVEs of the same structure, as Figure 3-5 shows.

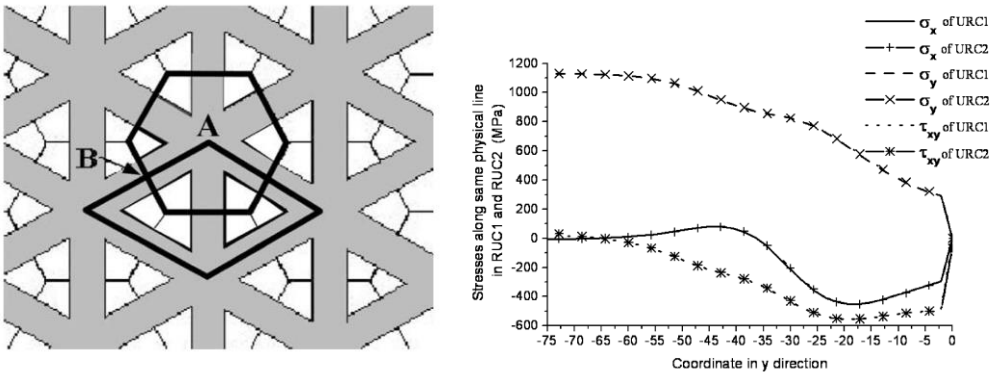

(a) (b)

Figure 3-5. (a) The shape of two RVEs A and B. (b) stress along same physical line of two RVEs with different RVE (RUC stands for representative unit cell which shares the same meaning in the figure legends) shapes [183].

The periodic boundary conditions assume that the corresponding nodes on the opposite edge of the mesh have the same translation pattern and the same rotations in all directions. Figure 3-6 shows two different types of periodic boundary conditions, the restricted periodic boundary conditions and general periodic boundary conditions. For the restricted periodic boundary conditions, one of the ends of the RVE structure is fixed thus no displacement will occur.

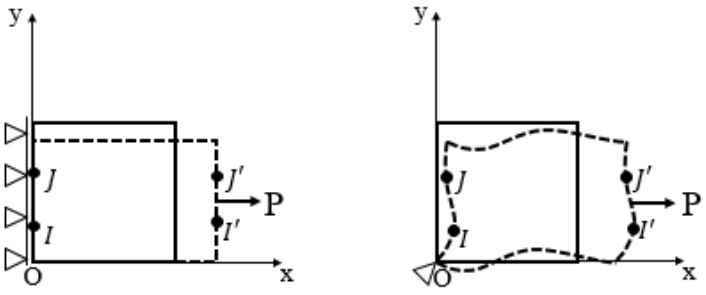

(a) (b)

Figure 3-6 Two types of periodic boundary conditions (a) Restricted periodic boundary conditions; (b) General periodic boundary conditions.

According to the definition, the constraint equations of the restricted periodic boundary conditions can be specified as follows:

$$u_I = 0;\ u_J = 0 \tag{3.5}$$

$$u_{I'} - u_I = u_{J'} - u_J \tag{3.6}$$

where u is one of the degrees of freedom of the FE node such as *I*, *I'*, *J* or *J'*. As $u_I = 0$ and $u_J = 0$, it can be easily derived that $u_{I'} = u_{J'}$, which means the shape of the RVE after deformation will be as same as the shape of the original one. For example, a cubic RVE as illustrated before will remain rectangular under a uniaxial load. This boundary condition is too strong because it is obvious that a cubic RVE of interpenetrating composite will become an entity with curved surface under uniaxial tension or compression. Therefore, a general periodic boundary condition is introduced as

$$u_{I'} - u_I = u_{J'} - u_J \tag{3.7}$$

we adopt

$$U = [u_x \quad u_y \quad u_z]^T \tag{3.8}$$

where u_x, u_y and u_z are the translations in nodal *x, y* and *z* directions. As the solid elements such as SOLID187 only have three translational degrees of freedom at each node, U in

$$U = [u_x \quad u_y \quad u_z]^T \tag{3.8}$$

can describe the deformation of each node of the RVEs. For a cubic RVE in this Chapter shown as Figure 3-7, the group of nodes located at the RVE facet on the *yz* plane of coordinates *oxyz* is designated as F_{xn} and those nodes opposite to F_{xn} is designated as F_{xp}. To make it clearer, the vertices of the cube is labelled as a, b, c, d, o, e, f, g. Face oabd is noted as F_{xn} . With the same manner, the F_{yn}, F_{yp}, F_{zn}, F_{zp} can be designated.

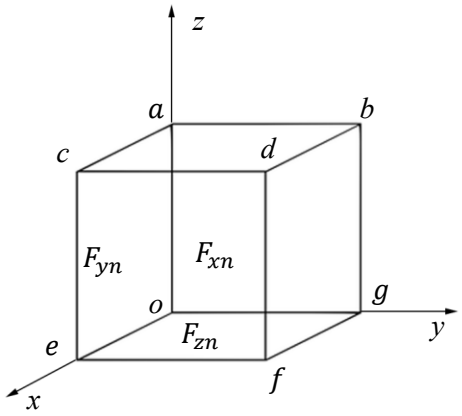

Figure 3-7. Schematic diagram of a cubic RVE.

Thus, the periodic boundary conditions of a cubic RVE can be specified as Equation 3.9 in [183]

$$U_{Fxp\ j} - U_{Fxn\ j} = U_{Fxp\ i} - U_{Fxn\ i} \tag{3.9}$$

However, when applying periodic boundary conditions on composite materials which two constituent materials filled the whole space of the solid cubic RVE. If periodic boundary conditions are simply applied at each cubic face, the over constraints on the edges and vertices of the cubic RVE could not be ignored. We denote the nodes on the vertices of a cubic RVE as V_1 to V_8 and the groups of nodes on the edges (except the vertices) of a cubic RVE as E_1 to E_{12}, respectively as Figure 3-8 shows. To avoid the over constraint issue, revised periodic boundary conditions for cubic RVE is presented in three groups.

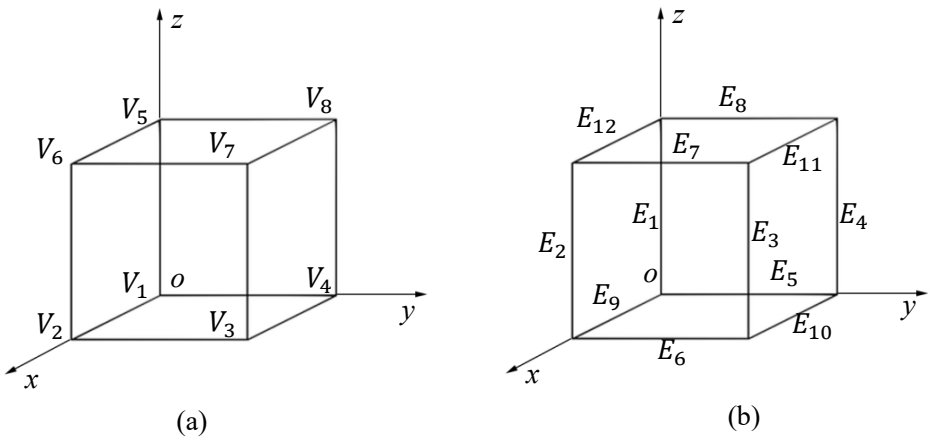

Figure 3-8. (a) Vertices of a cubic RVE. (b) Edges of a cubic RVE.

For the vertices, the constraint equations are

$$U_{V3} - U_{V4} = U_{V2} - U_{V1} \tag{3.10}$$

$$U_{V6} - U_{V5} = U_{V2} - U_{V1} \tag{3.11}$$

$$U_{V8} - U_{V5} = U_{V4} - U_{V1} \tag{3.12}$$

$$U_{V7} - U_{V8} = U_{V2} - U_{V1} \tag{3.13}$$

Where U_{V1} to U_{V8} are the translations of the nodes located on the vertices of the RVE. For example, U_{V1} are the translations in *x*, *y* and z directs of the node on V_1. To avoid over constraints on the vertices, we cannot constrain all the nodes pair by pair. Four constraint equation are enough for the vertices of the RVE. For the edges, U_{E1} to U_{E12} represent for the translations of the groups of nodes in E_1 to E_{12} except for the nodes on corresponding vertices. For example, U_{E1} are the translations of the group of nodes among group E_1 except for node V_1 and V_5. Thus, the translations in *x*, *y* and z directs of the group of nodes in E_1 can be denoted as $U_{E1\,i}$. The constraint equations are

$$U_{E2\,j} - U_{E1\,j} = U_{E2\,i} - U_{E1\,i} \tag{3.14}$$

$$U_{E3\,j} - U_{E4\,j} = U_{E3\,i} - U_{E4\,i} \tag{3.15}$$

$$U_{E4\,j} - U_{E1\,j} = U_{E4\,i} - U_{E1\,i} \tag{3.16}$$

$$U_{E6\,j} - U_{E5\,j} = U_{E6\,i} - U_{E5\,i} \tag{3.17}$$

$$U_{E7\,j} - U_{E8\,j} = U_{E7\,i} - U_{E8\,i} \tag{3.18}$$

$$U_{E8\,j} - U_{E5\,j} = U_{E8\,i} - U_{E5\,i} \tag{3.19}$$

$$U_{E10\,j} - U_{E9\,j} = U_{E10\,i} - U_{E9\,i} \tag{3.20}$$

$$U_{E11\,j} - U_{E12\,j} = U_{E11\,i} - U_{E12\,i} \tag{3.21}$$

$$U_{E12\,j} - U_{E9\,j} = U_{E12\,i} - U_{E9\,i} \tag{3.22}$$

To avoid over constraint issue, only 9 constraint equations are listed instead of 12. For the facets, U_{Fxn} to U_{Fzp} represent for the translations of the groups of nodes on the facets of the RVE. For example, U_{Fxn} is the translations of the groups of nodes on F_{xn} except for edges E_1, E_4, E_5, E_8 and vertices V_1, V_5. The constraint equations are

$$U_{Fxp\,j} - U_{Fxn\,j} = U_{Fxp\,i} - U_{Fxn\,i} \tag{3.23}$$

$$U_{Fyp\,j} - U_{Fyn\,j} = U_{Fyp\,i} - U_{Fyn\,i} \tag{3.24}$$

$$U_{Fzp\,j} - U_{Fzn\,j} = U_{Fzp\,i} - U_{Fzn\,i} \tag{3.25}$$

For the meshed cubic RVEs, there are only one node on each vertex, thus Equation 3.10 to Equation 3.13 can be directed applied as constraint equations in ANSYS. For the nodes on the edges except for the nodes on the vertices of the RVEs, the Equation 3.14 to Equation 3.22 can be specified as

$$U_{E2\,i} - U_{E1\,i} = U_{V2} - U_{V1} \tag{3.26}$$

$$U_{E3\,i} - U_{E4\,i} = U_{V2} - U_{V1} \tag{3.27}$$

$$U_{E4\,i} - U_{E1\,i} = U_{V4} - U_{V1} \tag{3.28}$$

$$U_{E6\,i} - U_{E5\,i} = U_{V2} - U_{V1} \tag{3.29}$$

$$U_{E7\,i} - U_{E8\,i} = U_{V2} - U_{V1} \tag{3.30}$$

$$U_{E8\,i} - U_{E5\,i} = U_{V5} - U_{V1} \tag{3.31}$$

$$U_{E10\,i} - U_{E9\,i} = U_{V4} - U_{V1} \tag{3.32}$$

$$U_{E11\,i} - U_{E12\,i} = U_{V4} - U_{V1} \tag{3.33}$$

$$U_{E12\,i} - U_{E9\,i} = U_{V5} - U_{V1} \tag{3.34}$$

For the nodes on the faces except for those on the vertices and edges of the RVEs, the Equation 3.23 to Equation 3.25 can be specified as

$$U_{Fxp\,i} - U_{Fxn\,i} = U_{V2} - U_{V1} \tag{3.35}$$

$$U_{Fyp\,i} - U_{Fyn\,i} = U_{V4} - U_{V1} \tag{3.36}$$

$$U_{Fzp\,i} - U_{Fzn\,i} = U_{V5} - U_{V1} \tag{3.37}$$

For Type I, II and III composite structures in this chapter, constrain Equations 3.10 – 3.13, 3.26-3.34 and 3.35-3.37 are applied to the nodes on the vertices, edges and faces of the RVE. This can be done by ANSYS with APLD coding to execute each specific node. On each boundary, one pair of nodes is selected to serve as the reference nodes for the displacement constraints. A small uniaxial translational load of 0.1% of the RVE

length L is applied on one of the reference nodes. The displacement load is denoted as $u_{x0} = L \times 0.1\%$. It is obvious that the RVEs are all symmetric about the x, y and z-axis. So only one axis needs to be considered. For example, we choose V_1 and V_2 and then apply load u_{x0} on the node at V_1. The node on V_2 is fixed.

3.3 Results

The reaction force F_r on the pair of reference nodes can be obtained after solving in ANSYS. F_r can be regarded as the concentrated force of the loaded face as all other nodes are constrained with the reference nodes by equation. Thus, the Young's modulus in the x-direction of the RVE can be expressed as

$$E_{cx} = \frac{\sigma_x}{\varepsilon_x} = \frac{\frac{F_r}{A_x}}{\frac{u_{x0}}{L}} = \frac{F_r}{Lu_{x0}} \tag{3.38}$$

where σ_x is the stress in the x direction, ε_x is the strain in the x direction, A_x is the area of the face F_{xn}. The Poisson's ratio ν_{cxy} and ν_{cxz} can be obtained from

$$\nu_{cxy} = -\frac{u_y}{L\varepsilon_x} \tag{3.39}$$

$$\nu_{cxz} = -\frac{u_z}{L\varepsilon_x} \tag{3.40}$$

3.3.1 Effects of the Young's moduli of constituent materials on the Young's moduli of the composites

Relationship between the Young's modulus of the composite E_c and volume fraction of the reinforcement f_f is obtained from IPC type I. Results are shown in Figure 3-9. The volume fraction of IPC type I is from 3% to 95%. The Voigt, Reuss, and the Hashin-Shtrikman upper and lower limits are also provided in Figure 3-9.

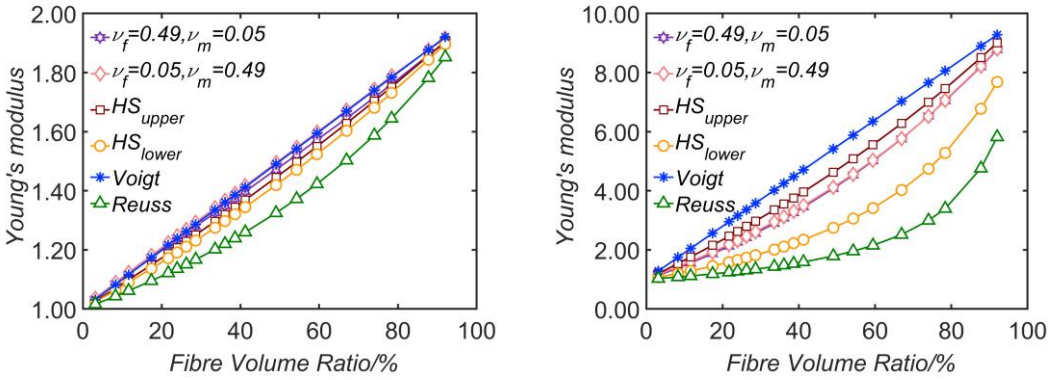

Figure 3-9. Young's Modulus of the composite E_c as a function of the reinforcement volume fractions in IPC type I, compared with Voigt, Reuss, and the HS upper and lower limits. (a) $E_f = 2$. (b) $E_f = 10$. All the Voigt, Reuss, and the HS upper and lower limits are presented coincident with the parameters of each material.

From Figure 3-9, Young's modulus of the composite E_c has a nearly linear function with fibre volume fractions f_f. When $E_f/E_m > 1$, E_c of composite type I increased in a linear relationship with f_f. The Young's modulus of composite type II and III are shown in Figure 3-11 and Figure 3-11.

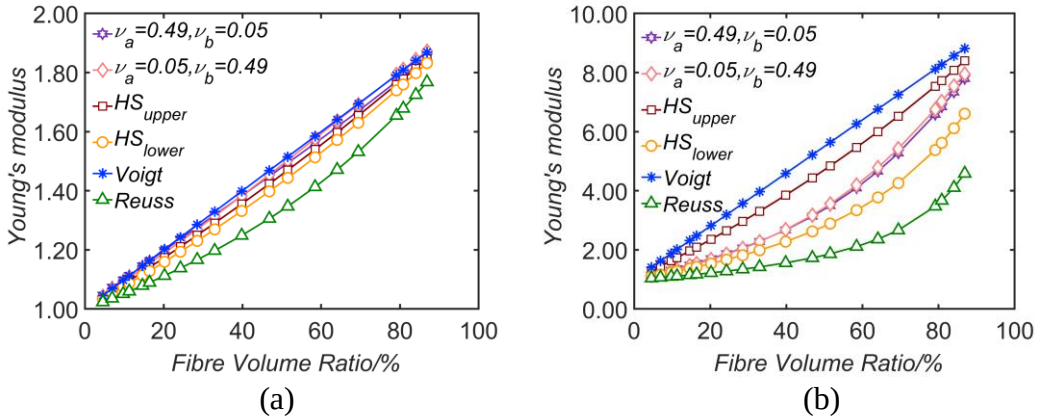

Figure 3-10. Young's Modulus of the composite E_c as a function of the reinforcement volume fractions in IPC type II, compared with Voigt, Reuss, and the HS upper and lower limits. (a) $E_f = 2$. (b) $E_f = 10$.

Figure 3-10 and Figure 3-11 show the same trend of E_c in relation to f_f. The volume fractions of IPC type II are from 3% to 90% and those of ICP type III are from 3% to 47%.

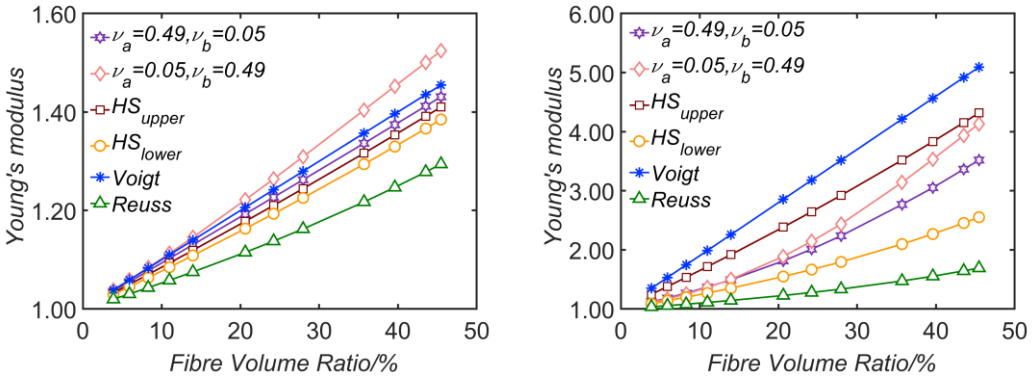

Figure 3-11. Young's Modulus of the composite E_c as a function of the reinforcement volume fractions in IPC type III, compared with Voigt, Reuss, and the HS upper and lower limits. (a) $E_f = 2$. (b) $E_f = 10$.

It can be seen from Figure 3-9 (a) that when the difference between Poisson's ratios of two constituent materials is large ($\nu_f = 0.05$, $\nu_m = 0.49$), while there are no big divergence in the Young's moduli of the two phases ($E_f/E_m = 2$), the Young's modulus of the composite can be slightly larger than Voigt limit. These results be found at all 3 types of RVEs, especially in type III. However, when the difference between the Young's moduli of the two constituent materials are big enough, for instance $E_f/E_m = 10$ in Figure 3-9 (b), and the other parameters remain the same, the Young's modulus of the composite stays lower than the Voigt and Hashin-Shtrikman upper limits. This result coincident with the theoretically analysis that if $\nu_m = \nu_f$, the Young's Modulus of the composite is much larger than Reuss and Hashin-Shtrikman's lower limit. However, no matter what E_f/E_m combinations and model structure chosen, the composite elastic moduli can't surpass the Voigt limit [75].

3.3.2 Effects of the Poisson's ratios of constituent materials on the Young's moduli of the composites

Poisson's ratios of the constituent material can also affect the mechanical properties of the composite. Matrices with both positive ($\nu_f = 0.49$, $\nu_m = 0.05$; ($\nu_f = 0.05$, $\nu_m =$

0.49) and negative Poisson's ($\nu_f = 0.49, \nu_m = -0.8$; $\nu_f = 0.3, \nu_m = -0.8$) ratios are considered in this Chapter.

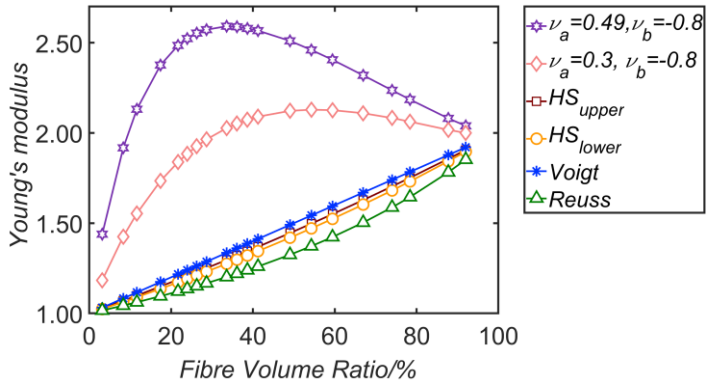

(a)

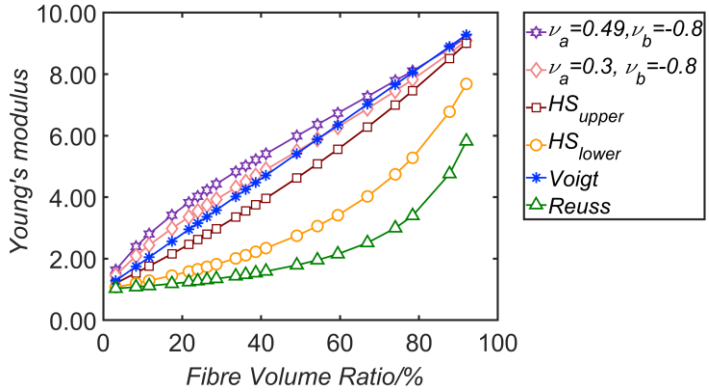

(b)

Figure 3-12. Young's Modulus of the composite E_c as a function of the reinforcement volume fractions in IPC type I with auxetic matrix, compared with Voigt, Reuss, and the HS upper and lower limits. (a) $E_f = 2$. (b) $E_f = 10$.

Figure 3-12 (a) give an outcome that the Young's Modulus of the composite type I drastically surpass the Voigt limit when the Poisson's Ratio of one phase of the composite goes to negative ($\nu_f = 0.49, \nu_m = -0.8$). The Young's Modulus acquired with negative Poisson's ratios matrix is far larger than that acquired with positive ones. The Young's Modulus of the composite rises with the volume fraction of the reinforcement increases, peaks when the volume fraction of the reinforcement is in the range of 30% to 50%, surpass the Young's Modulus of the reinforcement, then gradually goes down, closing to the Voigt limit at the end of 95%. In Figure 3-12 (b),

when the difference between the Young's moduli of the two constituent materials is large ($E_f/E_m = 10$), the Young's Modulus of the composite is still larger than the Voigt limit in the most of the fibre volume fractions. However, the difference between E_c and E_{cvoigt} is not that big compared to Figure 3-12 (a). The Young's moduli of the composite cannot dramatically surpass the Young's Moduli of the reinforcement and keeps increasing as the volume fraction of the composites increase, instead of having obvious peaks at certain volume fractions.

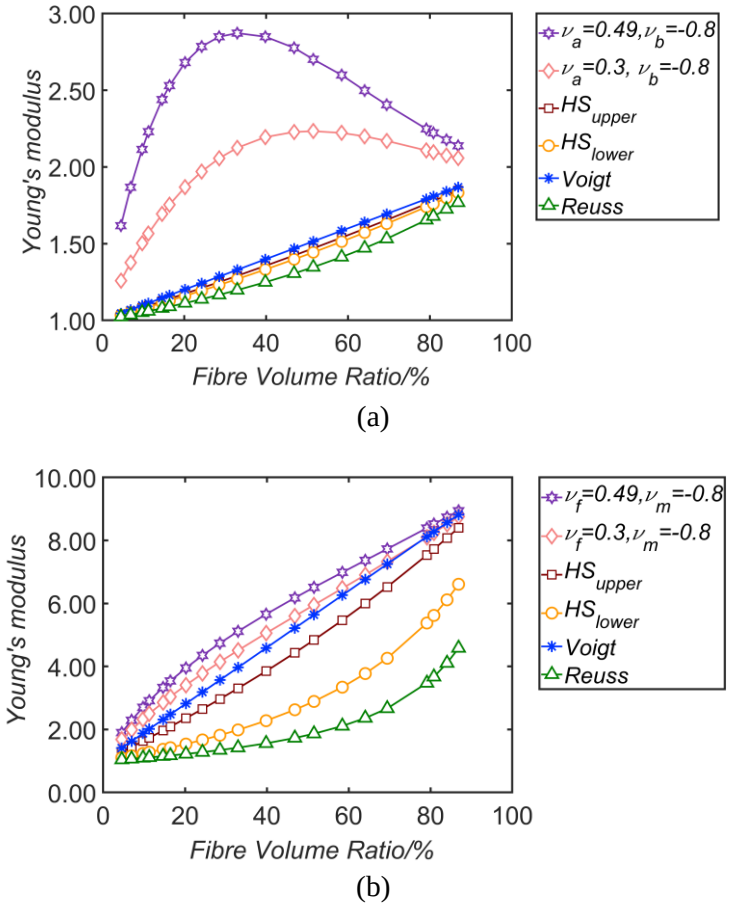

Figure 3-13. Young's Modulus of the composite E_c as a function of the reinforcement volume fractions in IPC type II with auxetic matrix, compared with Voigt, Reuss, and the HS upper and lower limits. (a) $E_f = 2$. (b) $E_f = 10$

The Young's Moduli of type II and type III composites with negative Poisson's ratio matrix is shown in Figure 3-13 and Figure 3-14. The relationships between volume fractions of the fibre and the Young's modulus of the composites at same constituent Poisson's ratio and material combinations in Figure 3-13 are almost the same with those

in Figure 3-12. The only different is that the peak of E_c at $E_f/E_m = 2$ of the Type II structure is higher than Type I, which means that type II structure can reach a large elastic modulus with same constituent material. In Figure 3-14, limited to the structure of type III composite, the maximum possible fibre volume fraction is around 47%. However, a clear peak of the curve of the Young's Modulus of the composite at $v_f = 0.05$, $v_m = 0.49$ can be observed. The shapes of all the curves Figure 3-14 are similar with half of the Figure 3-13 and Figure 3-12 with fibre volume fraction from 3% to 5%.

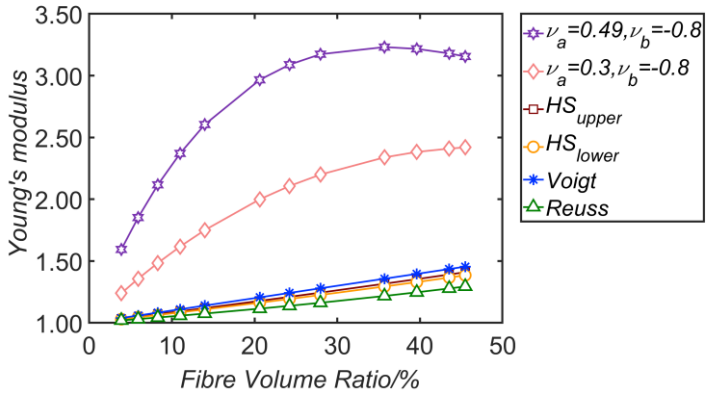

(a)

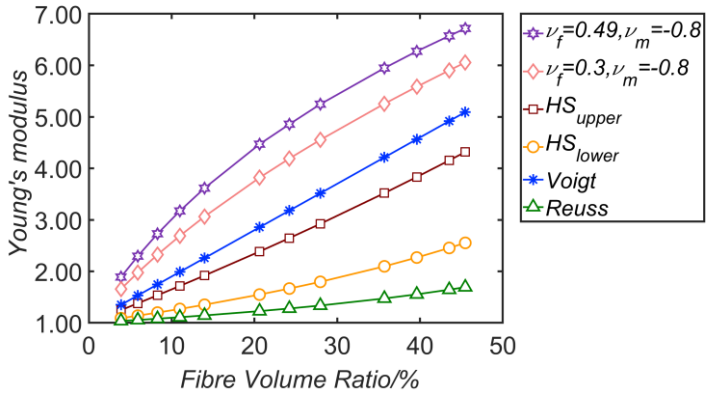

(b)

Figure 3-14. Young's Modulus of the composite E_c as a function of the reinforcement volume fractions in IPC type III with auxetic matrix, compared with Voigt, Reuss, and the HS upper and lower limits. (a) $E_f = 2$. (b) $E_f = 10$

All the three types of IPC structures share the same trend that Young's Modulus of the composites at $v_f = 0.49$, $v_m = -0.8$ are larger than that at $v_f = 0.3$, $v_m = -0.8$.

3.3.3 Comparison of regular lattice structured interpenetrating composites by normalized Young's moduli

Comparisons of the type I, II and III in 8 sets of parameter combinations listed in of the two phases are plotted below as Figure 3-15 (a) to (h).

Table 3-2. Sets of parameter combinations in Figure 3-15 (a) to (h).

	$\nu_f = 0.49$	$\nu_f = 0.05$	$\nu_f = 0.49$	$\nu_f = 0.3$
	$\nu_m = 0.05$	$\nu_m = 0.49$	$\nu_m = -0.8$	$\nu_m = -0.8$
$E_f/E_m = 2$	Figure 3-15 (a)	Figure 3-15 (c)	Figure 3-15 (e)	Figure 3-15 (g)
$E_f/E_m = 10$	Figure 3-15 (b)	Figure 3-15 (d)	Figure 3-15 (f)	Figure 3-15 (h)

In these figures the Young's moduli are normalized by the Voigt limit as Equation 2.7 shows. The normalized Young's modulus can be expressed as

$$E_N = E_c/E_{cVoigt} \tag{3.41}$$

The broken lines $y = 1.0$ parallel to *x* axis in Figure 3-15 indicates the Voigt limit itself. Thus, the results plotted above this line represents that the Young's modulus of the composite E_c surpasses the Voigt limit. A value of $E_N = 2.0$ means that the Young's modulus of the composite is 2 times larger than the upper limit. In general, we can see that the tetrakaidekahedron structure Type III performs well in negative Poisson's ratio matrix IPCs, while on the contrary, the simplest cross-cubic model performs the best in positive Poisson's ration matrix IPCs.

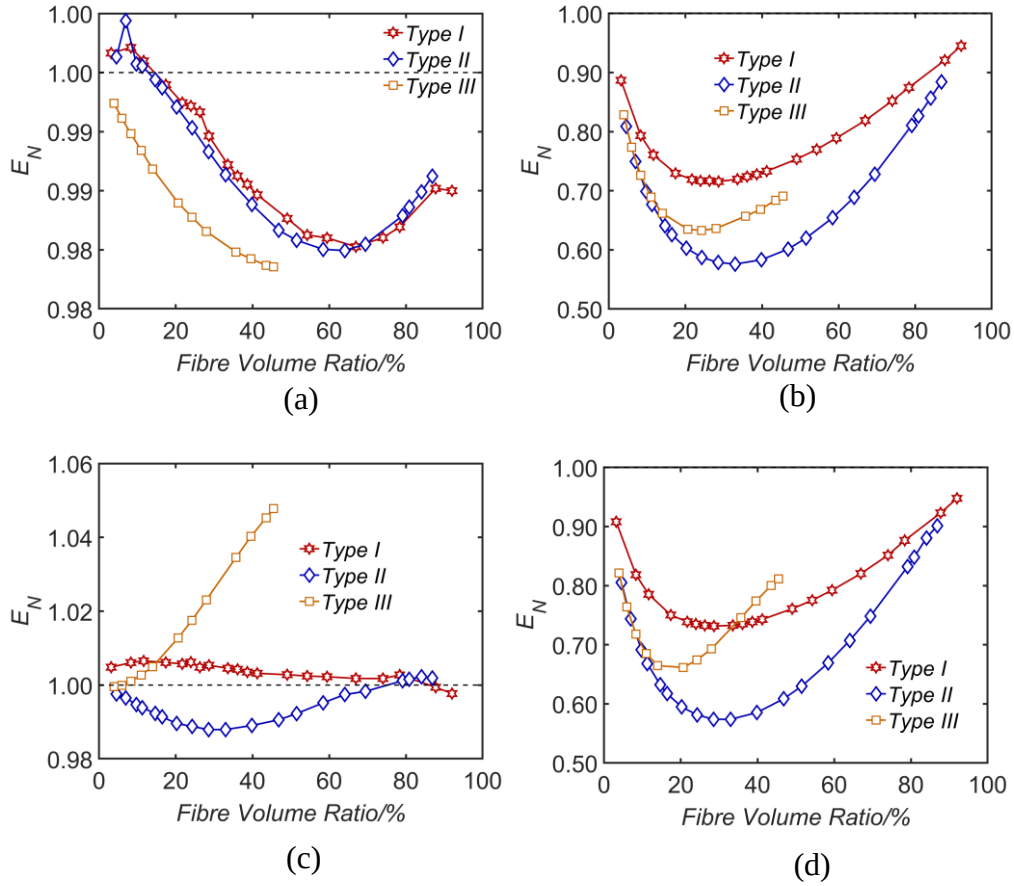

Figure 3-15. Comparison of Normalized Young's Modulus of the three types of composite structures: (a) to (d)

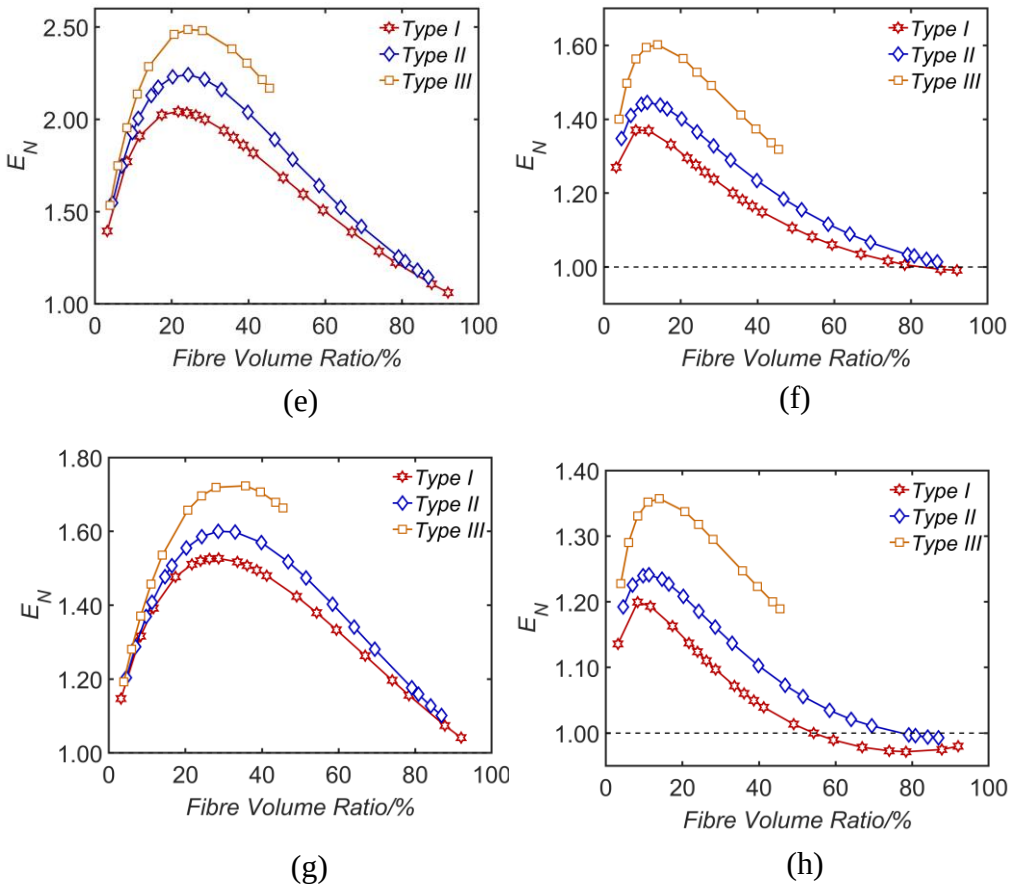

Figure 3-15. Comparison of Normalized Young's Modulus of the three types of composite structures

An overview of the Figure 3-15 shows that the normalized Young's modulus E_n decreases, reaches its lowest point, and then increases with the increase of fibre volume fraction when ν_f and ν_m are positive. Most of the values of E_n are smaller than 1 when ν_f and ν_m are positive, which mean the Young's moduli of the composite cannot surpass the Voigt limit when the Poisson's ratio of two constituent materials are positive. However, when ν_m is negative, the relations between normalized Young's modulus and fibre volume fraction turns to be the opposite, increases first, peaks, and then decreases. E_n is larger than 1 in most of the corresponding volume fractions and can be as large as 2.5. The Young's moduli of the composite can be two times larger than the Voigt limit. Furthermore, it can be summarized that E_n increases when E_f/E_{m} approaches 1 and $|\nu_f - \nu_m|$ get the largest possible value. When the Poisson's ratio of the matrix is

negative, the largest normalized Young's modulus can be obtained in around 30% fibre volume fraction when $E_f/E_{\mathrm{m}} = 2$ and in around 10% to 15% fibre volume fraction when $E_f/E_{\mathrm{m}} = 10$.

It can be observed in Figure 3-15 (a) to (d) that the normalized Young's moduli of IPC Type II and Type III are not as large as that of IPC Type I when the Poisson's ratios of the two constituent materials is all positive. The elastic performance of the IPC structure can be sequenced as $E_n|_{\text{Type I}} > E_n|_{\text{Type III}} > E_n|_{\text{Type II}}$ in most of the cases. However, Figure 3-15 (e) to (h) illustrate that when one constituent material exhibits negative Poisson's ratio behaviour, the elastic performance of IPC Type III is better than that of IPC Type I and Type II. The elastic performance of the IPC structure can be sequenced as $E_n|_{\text{Type III}} > E_n|_{\text{Type II}} > E_n|_{\text{Type I}}$ in most of the cases.

In addition, comparisons of Figure 3-15 (a) and (c), (b) and (d) reveal that the elastic performance of IPCs is not with much difference between $\nu_f = 0.05$, $\nu_m = 0.49$ and $\nu_f = 0.49$, $\nu_m = 0.05$. For example, the Young's moduli of the composite when $\nu_f = 0.05$, $\nu_m = 0.49$ and $\nu_f = 0.49$, $\nu_m = 0.05$ are very similar in IPC Type I and II. It can be inferred that the value difference between ν_f and ν_m instead of the values itself is the key to affect the elastic performance of the IPCs.

It can be seen from the stress maps of the reinforcements in Figure 3-16 (a) and (b) that the fibres along the axle directions (*x* axis direction in Figure 3-16 a and b) undertakes more load than those fibres along space diagonals. In Figure 3-16 (c) there are no fibre shows significant stress concentration in the tetrakaidekahedral reinforcements. In other words, that means normally the materials are most effectively constructed in Type I structure than Type II and III. That could be a possible explanation of why Type I composite structure performs the best.

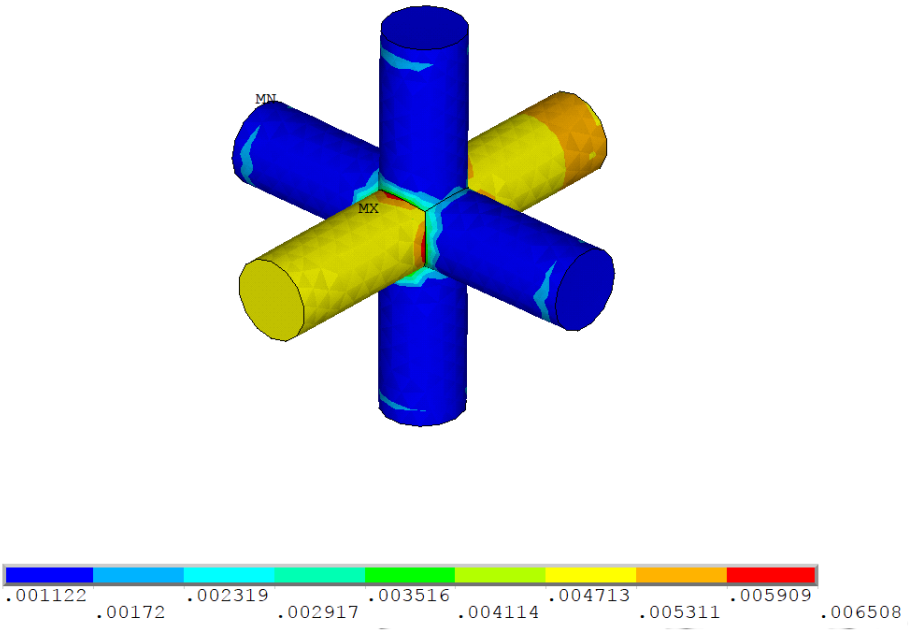
MN
MX
.001122
.00172
.002319
.002917
.003516
.004114
.004713
.005311
.005909
.006508

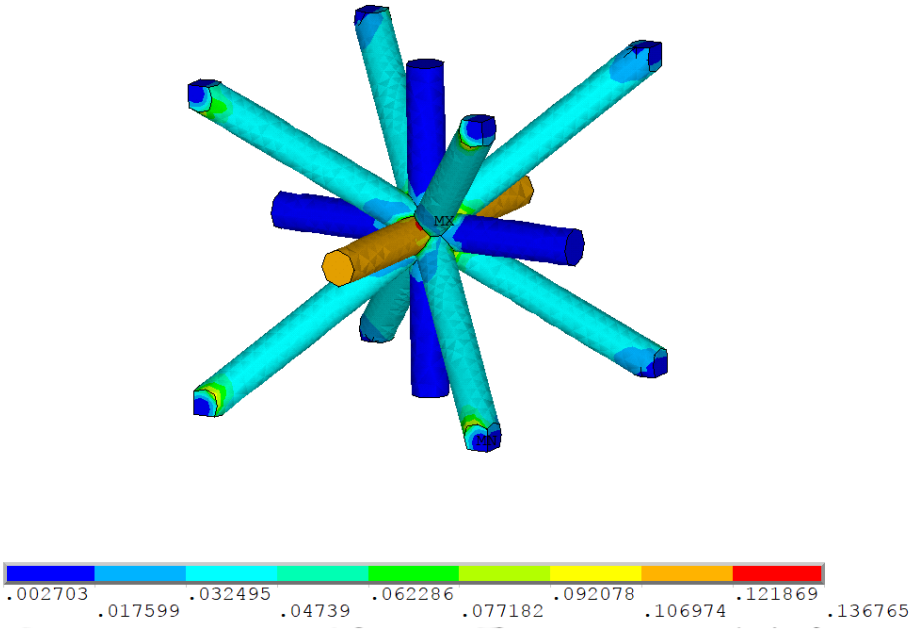
MX
.002703
.017599
.032495
.04739
.062286
.077182
.092078
.106974
.121869
.136765

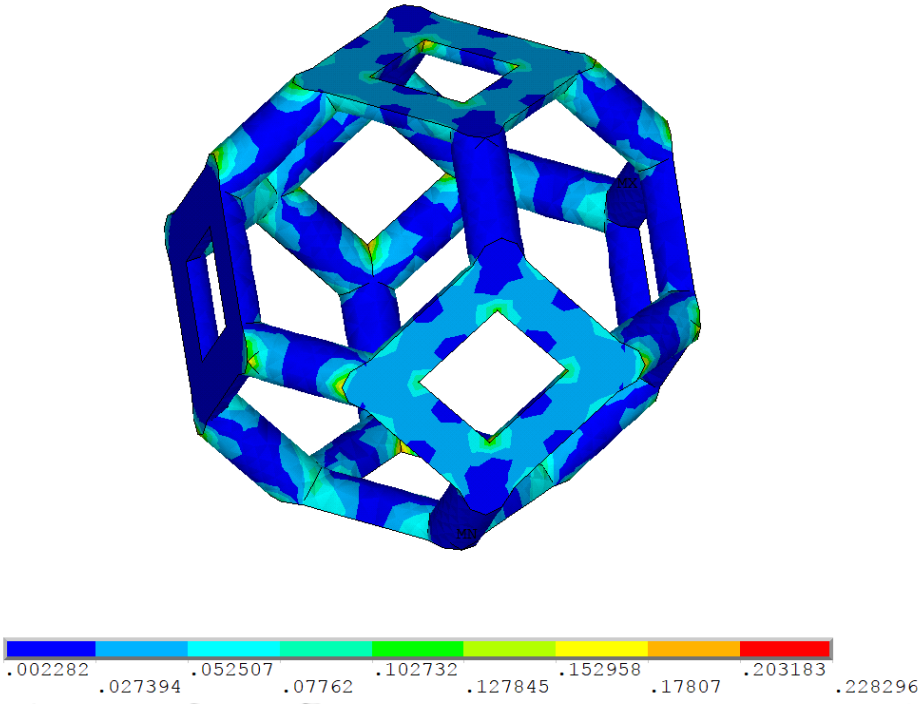

Figure 3-16. Comparison of Von Mise stress of the three types of composite structures.

When the Poisson's ratio of the composite goes to negative, it has been proved that the Young's moduli and Poisson's ratio of a cubic – cubic two-phase composite material as Figure 3-17 shows can be theoretically obtained by solving a set of 8 simultaneous linear equations as follows [74]

$$\frac{L-t}{LE_A}\left(\sigma_{x1}-\nu_A\sigma_{y1}-\nu_A\sigma_{y4}\right)+\frac{1}{LE_A}\left(\sigma_{x1}-\nu_A\sigma_{y2}-\nu_A\sigma_{y3}\right)=\varepsilon_x$$

$$\frac{L-t}{LE_A}\left(\sigma_{x2}-2\nu_A\sigma_{y1}\right)+\frac{1}{LE_A}\left(\sigma_{x2}-2\nu_A\sigma_{y2}\right)=\varepsilon_x$$

$$\frac{L-t}{LE_B}\left(\sigma_{x3}-2\nu_B\sigma_{y4}\right)+\frac{1}{LE_B}\left(\sigma_{x3}-2\nu_A\sigma_{y3}\right)=\varepsilon_x$$

$$\frac{L-t}{LE_A}\left(\sigma_{y1}-\nu_A\sigma_{x1}-\nu_A\sigma_{y4}\right)+\frac{1}{LE_A}\left(\sigma_{y1}-\nu_A\sigma_{x2}-\nu_A\sigma_{y1}\right)=\varepsilon_y$$

$$\frac{L-t}{LE_A}\left(\sigma_{y2}-\nu_A\sigma_{x1}-\nu_A\sigma_{y3}\right)+\frac{1}{LE_A}\left(\sigma_{y2}-\nu_A\sigma_{y2}-\nu_A\sigma_{x2}\right)=\varepsilon_y$$

$$\frac{L-t}{LE_A}\left(\sigma_{y3}-\nu_A\sigma_{x3}-\nu_A\sigma_{y3}\right)+\frac{1}{LE_A}\left(\sigma_{y3}-\nu_A\sigma_{x1}-\nu_A\sigma_{y2}\right)=\varepsilon_y$$

$$\frac{L-t}{LE_B}\left(\sigma_{y4}-\nu_A\sigma_{y4}-\nu_A\sigma_{x3}\right)+\frac{1}{LE_A}\left(\sigma_{y4}-\nu_A\sigma_{x1}-\nu_A\sigma_{y1}\right)=\varepsilon_y$$

$$(L-t)^2\sigma_{y4} + (L-t)t\sigma_{y1} + (L-t)t\sigma_{y3} + t^2\sigma_{y2} = 0$$

Where L and t are dimensions shown in Figure 3-17 below from which the fibre volume fraction can be obtained. $\sigma_{x1}, \sigma_{x2}, \sigma_{x3}$ *and* $\sigma_{y1}, \sigma_{y2}, \sigma_{y3}, \sigma_{y4}$ are normal stresses on two surfaces of the 1/8 RVE shown below.

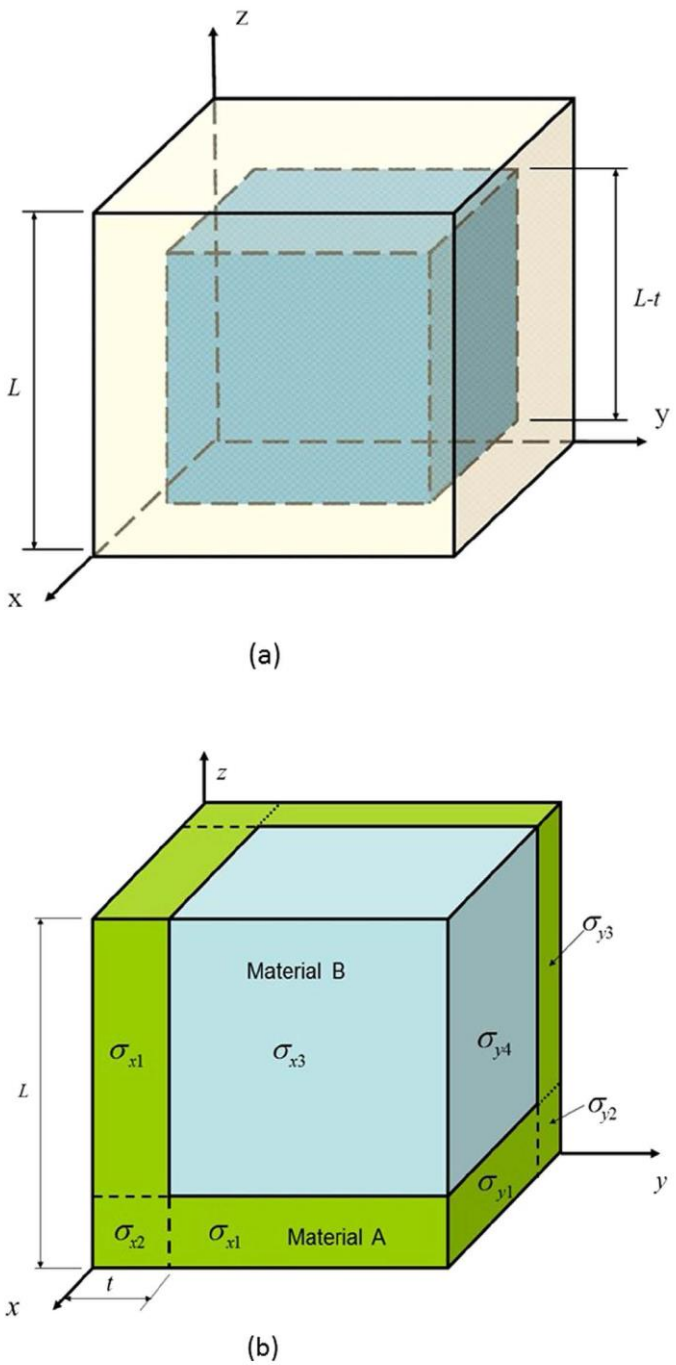

Figure 3-17. Theocratical model of cubic – cubic two-phase composite material

In this case, given L=10 and t=1, thus fibre volume fraction is $1-(L-t)^3/L^3=$ 27.1%, $E_f/E_m=10$, and ε_x=0.001. Confine the Poisson's ratio of fibre ν_f from 0 to 0.5 and that of matrix ν_m from -1 to 0.5, the relation between ν_f, ν_m, and the Young's moduli of the composite can be obtained, as Figure 3-18 shows.

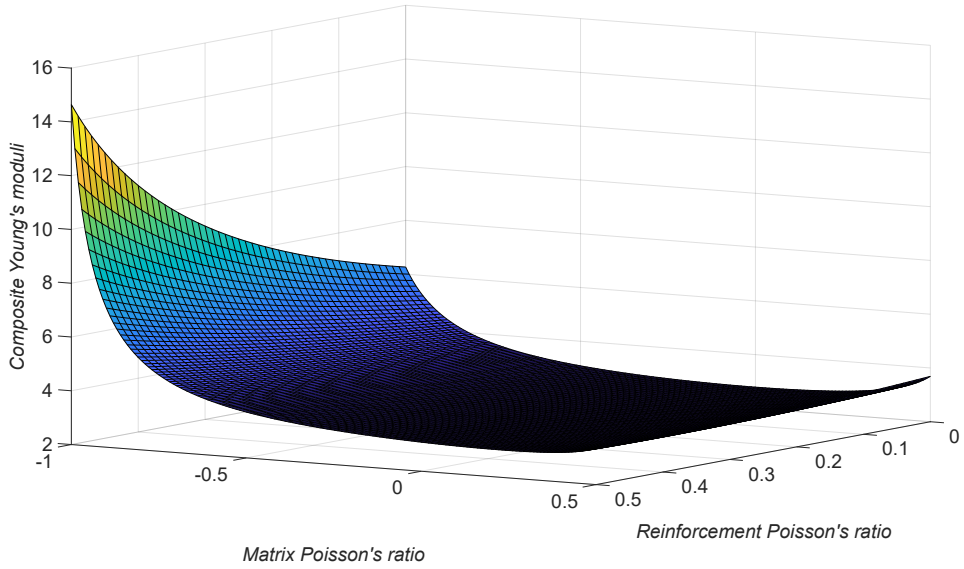

Figure 3-18. The relation between ν_f, ν_m, and the Young's moduli of the composite.

The results showed that the Young's moduli of this kind of structure could exceed Voigt limit, even large than both matrix and reinforcement when the Poisson's ratio of its one phase is negative and that of the other phase is positive. The Young's moduli of the composite reach the maximum value at $\nu_f=0.5$, $\nu_m=-1$.

Furthermore, the effect of Young's moduli of matrix and reinforcement on the Young's moduli of the composite is considered. Given L=10 and t=1, thus fibre volume fraction is $1-(L-t)^3/L^3=27.1\%$, and ε_x=0.001, Figure 3-19 shows the case that $\nu_f=0.2$, $\nu_m=0.3$ and Figure 3-20 shows the case that $\nu_f=0.5$, $\nu_m=-0.8$.

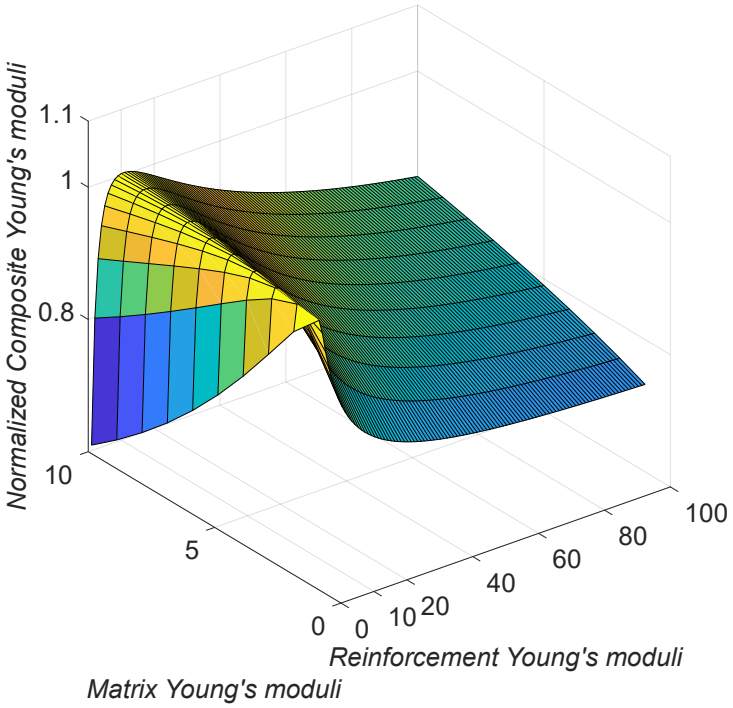

Figure 3-19. The relation between E_f, E_m, and the normalized Young's moduli of the composite when $\nu_f = 0.2, \nu_m = 0.3$.

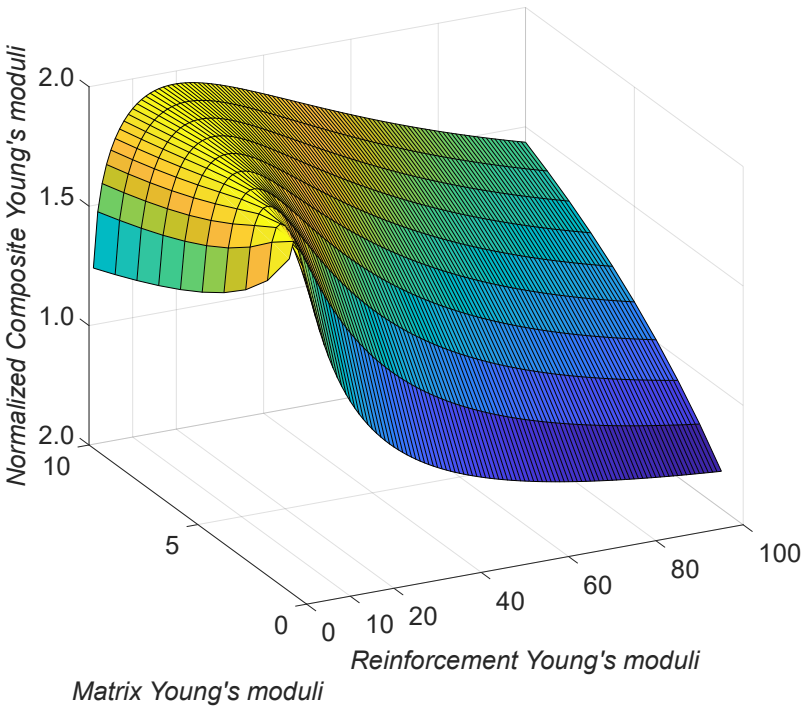

Figure 3-20. The relation between E_f, E_m, and the normalized Young's moduli of the composite when $\nu_f = 0.5, \nu_m = -0.8$.

The Young's moduli of the composite are normalized by the Voigt limit. It can be seen in both cases that when E_f, E_m are close the normalized Young's moduli reaches maximum value.

The cross-section strut shape changes from cubic to circle in this chapter, but the results are still compatible.

From the perspective of the results, it can be seen that the matrix undertakes much more load from the stress map as Figure 3-21 shows when the Poisson's ratio goes to negative comparing to the cases with positive Poisson's ratio matrix.

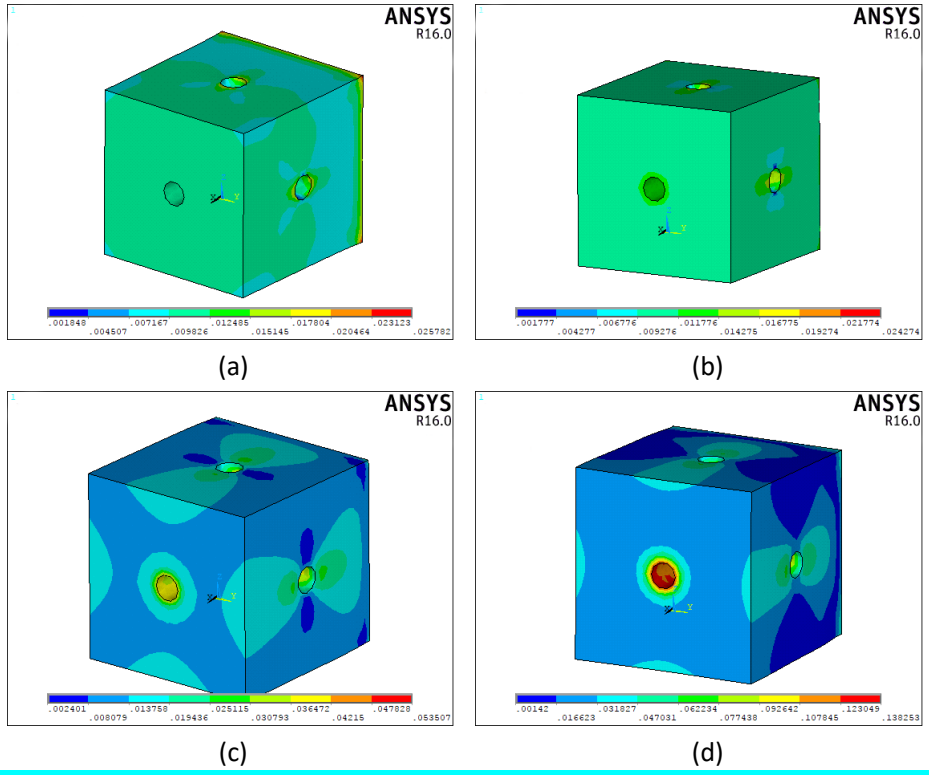

Figure 3-21. Von mises stress map of the matrix Type I structure when fibre volume fraction is set as 10%, $E_f/E_m = 10$: (a) $\nu_f = 0.2$ $\nu_m = 0.3$, (b) $\nu_f = 0.49$ $\nu_m = 0.05$, (c) $\nu_f = 0.49$ $\nu_m = -0.5$, (b) $\nu_f = 0.49$ $\nu_m = -0.8$.

From the figure above it is obvious that the matrix with same parameters other than the Poison's ratio under the same load result in very different stress average value and stress distribution. Both are larger when the difference between the Poisson's ratio of matrix and reinforcement is larger. This may be caused by interaction between the matrix and the reinforcement through the interface. The higher inner pressure between the interface of matrix and the reinforcement contributes to the resistance of

deformation when difference between the Poisson's ratios of matrix and reinforcement is large. Otherwise when this difference is small there are no significant pressure between the two during deformation.

3.4 Discussion

As traditional particulate composites and unidirectional fibre reinforced composites have been developed and investigated, it is necessary to compare the elastic properties of these lattice structured interpenetrating composites to its conventional counterparts. Chawla, Sidhu and Ganesh [35] did a detailed investigation for SiC/Aluminium particle composite both experimental and computational. In 1983, the tensile behaviour of polystyrene-glass-bead composites has been tested [184]. Those are all typical particle reinforced composites. Comparing particle composites to IPCs could prove that interpenetrating phases enhances the elastic performance of the composite with same constituent material and fibre volume fraction. Figure 3-22 illustrates the microstructures of the particle reinforced composites.

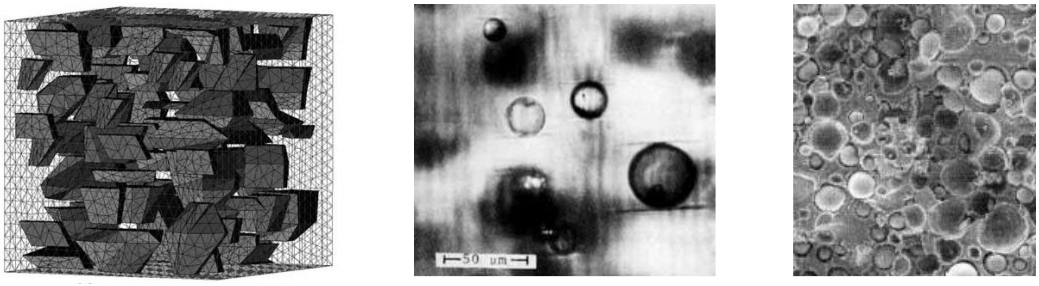

(a) (b) (c)

Figure 3-22. The particle reinforced composites listed for comparison. (a) SiC /Aluminium particle composite [35]. (b) Glass reinforced polystyrene [184]. (c) Epoxy based glass particle composite [185].

Table 3-3 listed the elastic properties of some particle reinforced composites.

Table 3-3 Summary of particle reinforced composites used in comparison with our models.

Composites	E_f (MPa)	ν_f	E_m (MPa)	ν_m
SiC /Al [35]*	410000	0.19	74000	0.33
Glass/Polystyrene [184]	70000	0.22	3250	0.34
Glass /Epoxy [185]**	69000	0.15	3000	0.35

* Computational results from reference [35] are taken for comparison

** Experimental results from reference [185] are taken for comparison

The reinforcement volume fractions of the composites in reference papers are listed in Table 3-4 below.

Table 3-4. Volume fractions of the composites in reference papers.

Composites	Reinforcement volume fractions				
SiC /Al [35]	10%	20%	30%		
Glass/Polystyrene [184]	10%	15%	20%	25%	
Glass /Epoxy [185]	14%	22%	28%	35%	43%

The normalized Young's moduli of our models are obtained and compared with the models in listed references above. The results are plotted in the Figure 3-23 below.

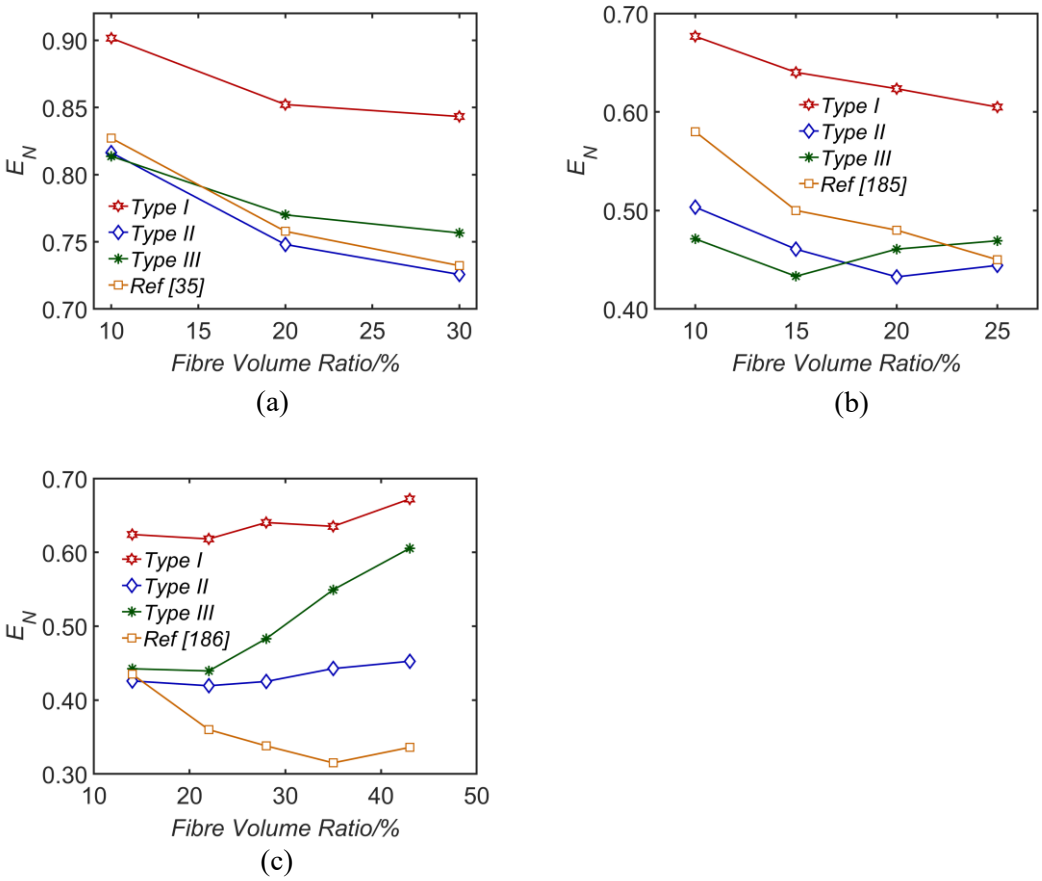

Figure 3-23. Comparison of the 3 types of structures with the traditional particle composites in research papers. computational results from reference [35] in subfigure (a), experimental results from reference [184] in subfigure (b), and experimental results from reference [185] in subfigure (c).

Figure 3-23 shows that when the Poison's ratios of both two phases of the composite are close and positive, the simple cubic model performs much better than the particle composites and maintain the best among those three models regarding each set of material parameters.

Interpenetrating phase composites have also been fabricated via different methods. It is also a wide concern to investigate which type of geometry structure model can reveal their mechanical properties more precisely. For the interpenetrating composites, especially those with well-connected lattice structures are hard to fabricate, the experimental sample and results in research papers often lacks the comprehensiveness for investigating the mechanical behaviour with the Young's modulus and Poison's ratio of each phase.

In this thesis, research of the interpenetrating composite materials including both experimental and computational work are compared with our models.

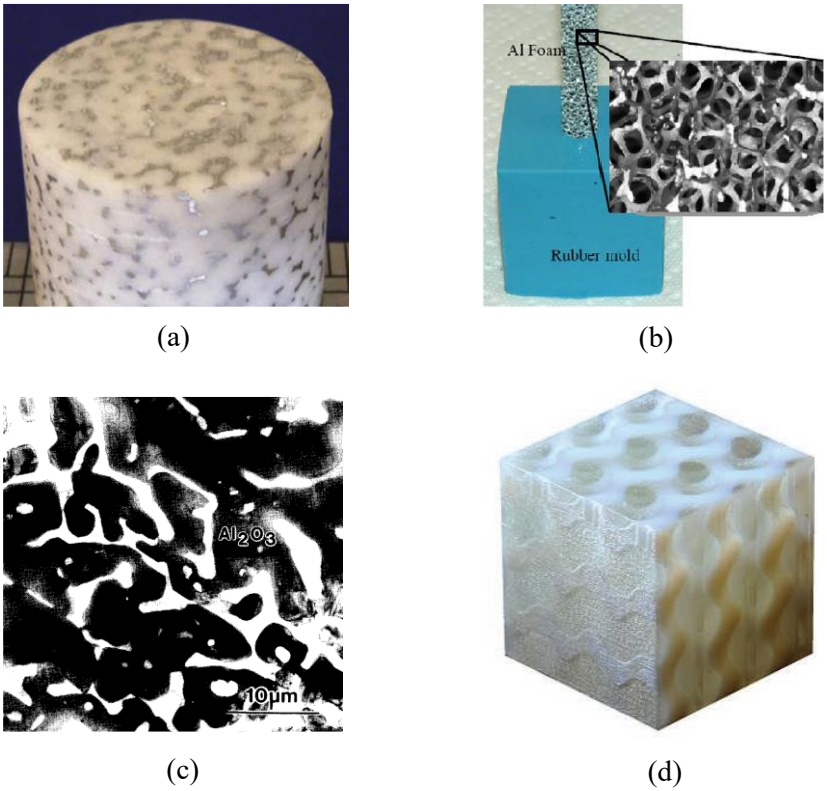

(a) (b)

(c) (d)

Figure 3-24. Interpenetrating composite materials listed for comparison. (a) Syntactic Foam with coated aluminium scaffold [57]. (b) Syntactic Foam prepared by dispersing hollow glass micro balloons into an epoxy matrix, reinforced by metal form using open-cell Duocel® aluminium [186]. (c) Al/Al_2O_3 composites [54]. (d) TangoPlus/VeroWhite composites formed by Boolean operations from triply periodic minimal surfaces [65]. All these results are experimental except Jhaver and Hareesh's work [57].

The parameters in the research papers are summarized below in Table 3-5.

Table 3-5 Summary of interpenetrating composites used in comparison with our models, including mechanical properties of the constituent materials and the fibre volume fractions.

Composites	E_f (MPa)	ν_f	E_m (MPa)	ν_m	V_f
Syntactic Foam / Al [57]	68900	0.34	1600	0.33	9%
Syntactic Foam / Al [186]	69600	0.35	5122	0.34	8%
Al / Al_2O_3 [54]	380000	0.35	69600	0.25	65%

TangoPlus / VeroWhite [65]	1660	0.3*	0.7456	0.3*	48%

After comparison, the results are listed in Table 3-6.

Table 3-6 Results of the comparison of our models and other interpenetrating composites.

Compared paper \ E_N	Model 1	Model 2	Model 3	Paper Results
Syntactic Foam /Al [57]	0.583	0.378	0.333	0.276
Syntactic Foam /Al [186]	0.761	0.640	0.626	0.602
Al / Al_2O_3 [54]	0.871	0.789	0.791	0.792
TangoPlus/VeroWhite [65]	0.568	0.532	0.527	0.355

From the results in Table 3-6, we can find that the elastic property of our lattice interpenetrating structures are better than those interpenetrating composites fabricated with syntactic foam (epoxy and micro balloons in the aforementioned two papers) and aluminium, the alumina-aluminium composites, and TMPS-IPCs which are relatively difficult to fabricate with metals like alumina or steel.

3.5 Conclusion

In this Chapter, the geometric models of three types of RVEs are constructed by solid Boolean operations. The revised periodic boundary conditions generally suitable for solid cube RVE is specified. The constituent material combinations are selected to predict the effect of their Young's moduli and Poisson's ratio on the Young's moduli of the composite. It can be concluded from the results of this chapter that the Young's modulus of different lattice-structured interpenetrating composites can be much larger than the HS upper limit and can surpass the Voigt limit. This is coincident with the analytical results by Zhu, Fan and Zhang [74] in 2015. The Young's modulus of the composites E_c has strong relationship with the Poisson's ration of the two constituent materials. E_c increases as E_f, E_{m} and fibre volume fraction f_f increases. However, when the Poisson's ratio of the matrix is negative and E_f/E_{m} is relatively small, the

Young's modulus E_c increases with VF_f from the beginning, reaches its peak, and then decreases. The largest Young's modulus E_c can be obtained in around 30% to 40% fibre volume fraction in this case. Furthermore, the normalized Young's modulus E_n decreases, reaches its lowest point, and then increases with the increase of fibre volume fraction when ν_f and ν_m are positive. When ν_m is negative, the relations between normalized Young's modulus and fibre volume fraction turns to be the opposite trend, increases firstly, then decreases. E_n peaks when E_f/E_{m} approaches 1 and $|\nu_f - \nu_m|$ get the largest possible value. The largest normalized Young's modulus can be obtained in around 30% fibre volume fraction when $E_f/E_{\mathrm{m}} = 2$ and the Poisson's ratio of the matrix is negative and in around 10% to 15% fibre volume fraction when $E_f/E_{\mathrm{m}} = 10$.

Generally, the basic cubic model performs the best when the Poison's ratio of both phases of the composites are positive, while the tetrakaidekahedron model with the most connection points of the lattice structure show a larger normalized Young's modulus when the Poison's ration goes to negative.

These kind of latticed interpenetrating composites are better than its conventional counterparts like particle and unidirectional reinforced composites, as well as aluminium and TMPS-IPCs composites.

Chapter 4 Auxetic interpenetrating composites

4.1 Introduction

When a self-connected auxetic lattice structure or fibre-network is embedded as reinforcement in a matrix with a low positive Poisson's ratio, the composite would have the potential to exhibit auxetic behaviour. It has already been experimentally demonstrated that composites reinforced by an auxetic fibre-network exhibits a negative Poisson's ratio in the thickness direction [137]. Composites reinforced by a re-entrant hexagonal honeycomb are also found to exhibit strong in-plane auxetic behaviour [147]. As most of the microstructures which exhibit an auxetic behaviour are self-connected and periodic, auxetic lattice foams are perfect candidates as reinforcement in interpenetrating composites. Despite considerable efforts have been devoted to designing and synthesizing composites with auxetic reinforcements, the quantitative understanding of the interplay between the auxetic behaviour and the other mechanical properties such as stiffness, strength, and toughness is still elusive. Research on composites with auxetic behaviour are very limited and the properties are in general anisotropic. In this chapter, we study the mechanical behaviour of solid interpenetrating composites reinforced by three different types of auxetic fibre-networks with cubic symmetry. The concavity of the fibre-networks is considered as a key factor affecting the auxetic behaviour of the constructed composites. The effects of the volume fraction, elastic properties and concavity of the fibres, and the structural

hierarchy on the elastic properties of the interpenetrating auxetic composites are investigated by computational simulation.

4.2 Geometric structures and computational methods

4.2.1 Geometric structures

Re-entrant foams are the most common auxetic cellular-network materials, examples include 2D re-entrant honeycombs, 3D re-entrant foams, double-arrowhead re-entrant structure, star-shaped structure. In this chapter, we study the elastic properties of interpenetrating composites which are reinforced by three different types of regular re-entrant fibre-networks. As all the three types of interpenetrating composites are periodic and have cubic symmetry, we use representative volume elements to study their elastic properties. The RVE of the type I re-entrant fibre-network, as shown in Figure 4-1 (a), has 12 self-connected chevron struts in 6 rectangular diagonal planes, each of which contains two chevron struts. The RVE of the type II re-entrant fibre-network is shown in Figure 4-1 (b), which consists of 6 self-connected inward crosses. The RVE of the type III re-entrant fibre-network is shown in Figure 4-1 (c).

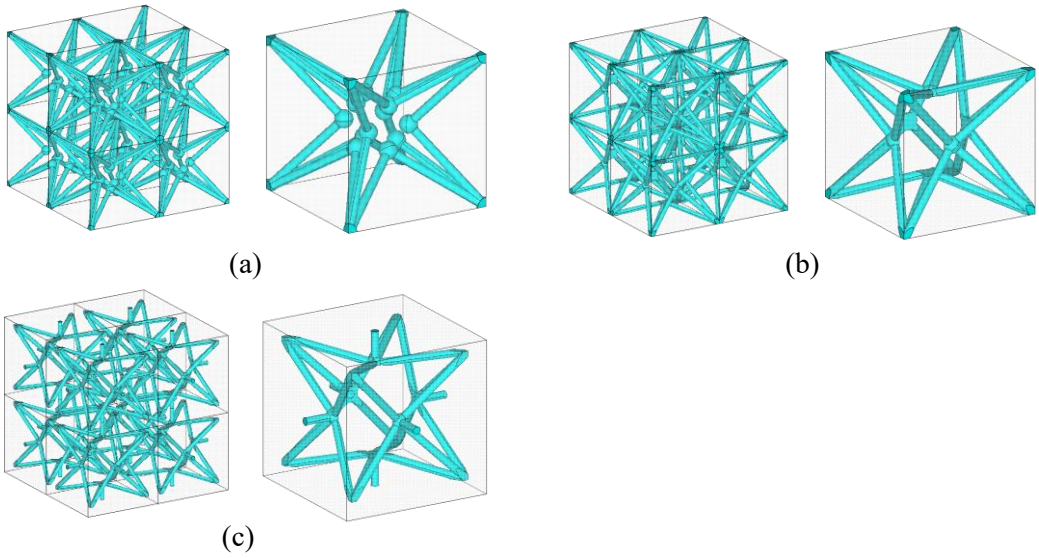

Figure 4-1. The geometrical structures of three different type of self-connected reinforcement auxetic fibre-networks: (a) Type I, (b) Type II, (c) Type III.

All the reinforced fibres are presumed to have a round axial section with the same diameter. The RVE models are constructed by the same method with the RVEs in Chapter 3.

4.2.2 Model parameters

One of the most important parameters for a two-phase interpenetrating composite is the fibre volume fraction. For the three different types of re-entrant fibre-networks, all the fibres are assumed to have the same uniform circular cross-section. The fibre volume fraction VF_f can be controlled by varying the diameter of the fibres or the fibre direction angle α shown in Figure 4-2. Because of the natural limit of the fibre-network geometric structures, the fibre volume fraction V_f considered in this thesis is limited in the range from 4% to 32% for type I and II composites, and from 2.5% to 20% for type III composites.

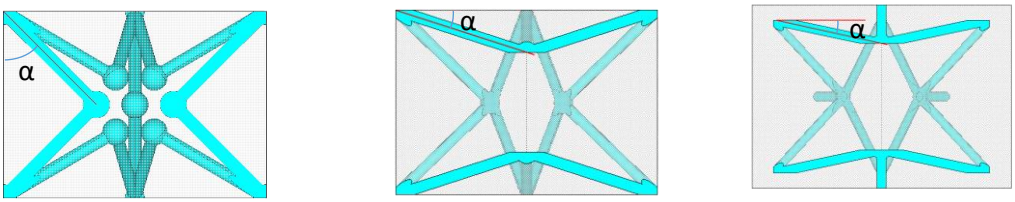

(a) (b) (c)

Figure 4-2. Fibre direction angle α in the three different types of reinforcement fibre-networks. (a) the chevron, angle α measured in the main diagonal plane of the type-I RVE; (b) and (c) the re-entrant, angle α measured in the RVE main diagonal plane of the type I and II composites.

For the three types of interpenetrating composites, their negative Poisson's ratio and other elastic properties (e.g., Young's modulus) significantly depend on the chevron or the re-entrant angle α. In order to explore how the fibre angle affects the elastic properties of the three types of interpenetrating composites, the following three sets of angles given in Table 4-1 are used in simulations.

Table 4-1. Fibre angle α of the three different types of fibre-networks.

	α_1	α_2	α_3
Type I	20°	30°	40°
Type II	12°	18°	20°
Type III	12°	18°	20°

It is assumed that the reinforcement fibre-network and the matrix of the interpenetrating composites are made by two different isotropic solid materials. The Young's moduli and Poisson's ratios of the constituent materials are denoted as E_f, E_m, ν_f, ν_m, where subscript f stands for fibre and m for matrix. For simplicity and generality, both the Young's moduli of the fibre and the matrix are normalised by that of the matrix, thus the normalised Young's modulus of the matrix is always 1 and the possible range of the normalised Young's modulus of the fibre is given in Table 4-2. In some 3D printed composites [65], VeroWhite (rigid photopolymer) is often used as the stiffer phase whose Young's modulus is $E_f = 1.66\text{GPa}$, and TangoPlus (soft rubbery material) is

often used as the softer phase whose Young's modulus is $E_m = 0.7456\text{MPa}$. Thus, the ratio E_f/E_m in such composites is close to 2500. In most polymer, rubber or metal matrix composites reinforced by a metal or ceramic, the ratio E_f/E_m stays in the range from 2 to 1000, examples include Al/epoxy composites [57], glass/epoxy composites [185] and Al/Al_2O_3 composites [54]. In order to enhance the auxetic behaviour (i.e., a large negative Poisson's ratio), a relatively high value of E_f/E_m is preferred.

Table 4-2. The range of the normalised Young's Moduli of three fibre material.

E_f/E_m	2	10	50	100	500	1000	2000

The elastic properties of composites can be significantly affected by the Poisson's ratio of the matrix material [74,75], but are less sensitive to that of the stiffening material (this may be because the volume fraction of the latter is usually much smaller). As almost all the single-phase solid isotropic materials have a positive Poisson's ratio, a very small Poisson's ratio is preferred for the matrix material in order to enhance the auxetic behaviour of the composites. For the aforementioned materials as the potential reinforcement and matrix phases, the Poisson's ratios of TangoPlus and VeroWhite are approximately 0.49 and 0.3 [65,146], which are not ideal for an isotropic auxetic composite. Carbon matrix may have a very low Poisson's ratio from approximately 0 to 0.05 [187], while the Poisson's ratio of SiC matrix is around 0.14 to 0.35. In metal matrix composites, beryllium which is used as the matrix material in AlBeMet for aerospace and commercial applications has a very low Poisson's ratio of 0.03 [188]. The Poisson's ratios of Al and Al_2O_3 are approximately 0.35 and 0.25, separately, and the carbon fibre has a Poisson's ratio between 0.05 and 0.1. Table 4-3 gives the combination of the Poisson's ratios of the possible matrix and fibre materials.

Table 4-3. Poisson's ratios of the fibre and matrix materials.

v_f	0.35	0.25	
v_m	0	0.1	0.2

4.2.2 Computational method

The RVE models of the composites reinforced by the three different types of auxetic fibre-networks are constructed in ANSYS. Both the fibre and matrix materials are assumed to be homogeneous and isotropic solids, and they both are partitioned into higher order 3D, 10-node tetrahedra (Solid187) elements. As all the three types of composites are periodic, periodic boundary conditions are applied to the RVE models in the finite element simulations. To obtain the Young's modulus and Poisson's ratios, a small tensile strain of 0.1% is applied to the RVE models in all the simulations.

4.3 Results

The three types of composites studied in this thesis can be used as either structural or functional materials in engineering applications. The focus of this study is on their function side, e.g., the negative or zero Poisson's ratios. As all the three types of composites have cubic symmetry in their geometric structure, they have only three independent elastic constants and their elastic properties are nearly isotropic, e.g., their Poisson's ratios are the same in their three orthogonal symmetric planes.

4.3.1 Effects of fibre volume fraction on the Poisson's ratio of the composites

The Poisson's ratios of the three different types of composites significantly depend on the fibre volume fraction. When the fibre angle is fixed at $\alpha = 20°$ for all the three different types of composites (see Figure 4-2), Figure 4-3 (a) shows the dependencies

of their Poisson's ratios on the fibre volume fraction while other parameters are fixed at $\nu_m = 0.1,\ \nu_f = 0.25,\ E_f/E_m = 1000$; and Figure 4-3 (b) presents the similar relationships when $\nu_m = 0,\ \nu_f = 0.25,\ E_f/E_m = 1000$.

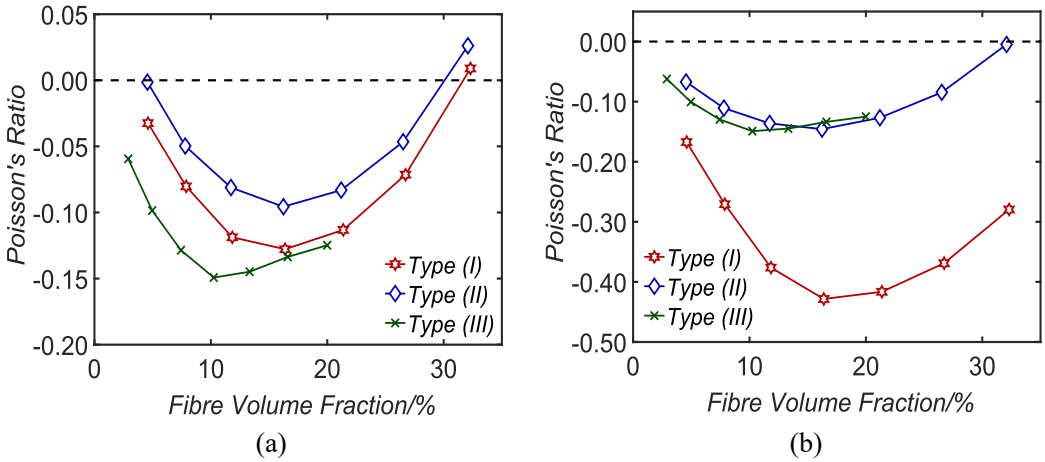

Figure 4-3. Effects of fibre volume fraction on the Poisson's ratio of the composites when $\alpha = 20°$. (a) $\nu_m = 0.1, \nu_f = 0.25,\ E_f/E_m = 1000$; (b) $\nu_m = 0, \nu_f = 0.25,\ E_f/E_m = 1000$.

As can be seen in Figure 4-3, all the three different types of composites exhibit a very strong negative Poisson's ratio when the fibre volume fraction is in range from 3% to 35%. The focus of this research is on the negative Poisson's ratio (i.e., the auxetic behaviour). Outside this fibre volume fraction range, the composites may not exhibit a negative Poisson's ratio. Obviously, all the three different types of solid composites could be designed to have a 'zero' Poisson's ratio. Comparison between the results in Figure 4-3 (a) and Figure 4-3 (b) illustrates that the Poisson's ratio of the matrix material can strongly affect the auxetic behaviour (i.e., the negative Poisson's ratio) of the composites, the smaller the Poisson's ratio of the matrix material, the larger the magnitude of the negative Poisson's ratio of the composites.

4.3.2 Effects of fibre angle α on the Poisson's ratios of the composites

Figure 4-4 shows the effects of the fibre angle α on the relationships between the Poisson's ratio and the fibre volume fraction for the three different types of composites

when all the other parameters are fixed at $\nu_m = 0.1,\ \nu_f = 0.25,\ and\ E_f/E_m = 1000$. As can be seen in Figure 4-4, in order to achieve large magnitude of negative Poisson's ratio for the composites, a suitable (or an optimal) fibre angle α is critical. This is consistent with the experimentally measured results in anisotropic composites [147] which showed that it is possible to obtain different Poisson's ratio structure by changing defined fibre angle θ.

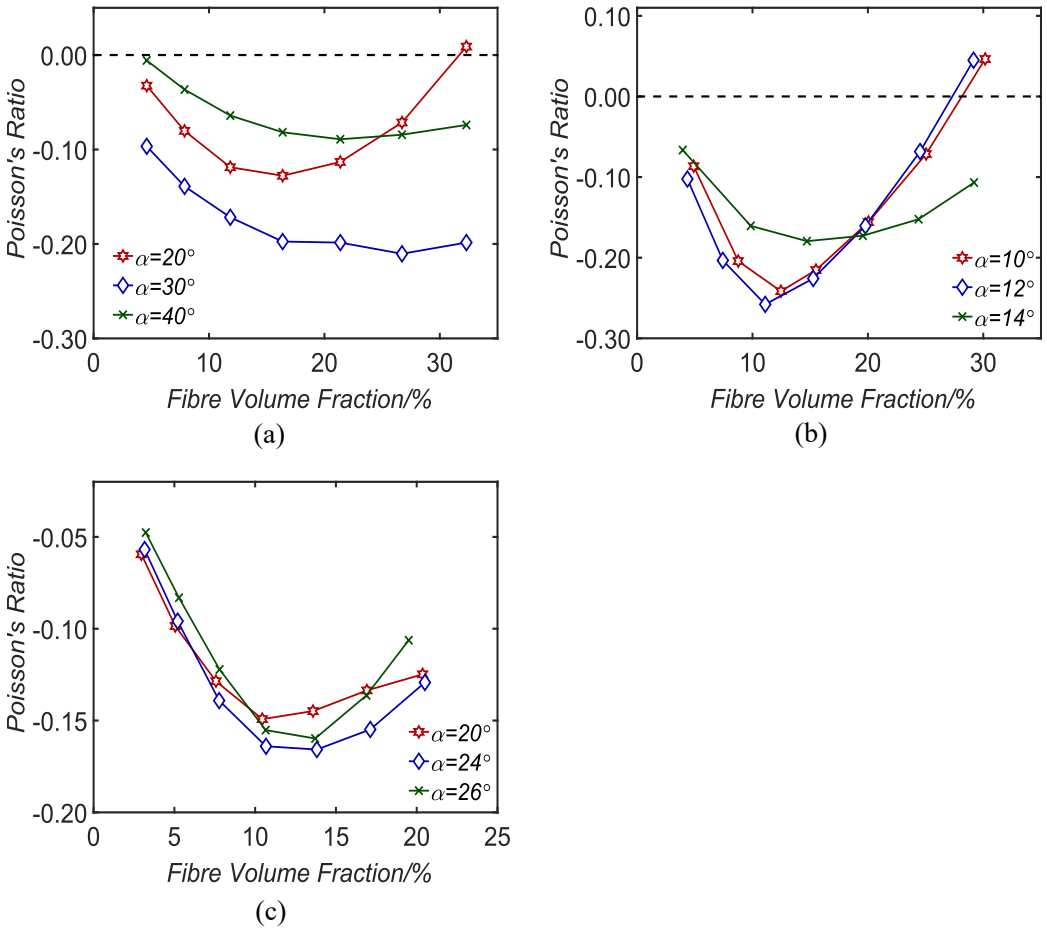

Figure 4-4. Effects of the fibre angle α on the relationships between the Poisson's ratio and the fibre volume fraction for the different types of composites. (a) Type I; (b) Type II; (c) Type III.

4.3.3. Effects of E_f/E_m on the Poisson's ratio of the composites

When $\alpha = 20°$, $\nu_m = 0.1$ and $\nu_f = 0.25$, the effects of E_f/E_m on the relationship between the Poisson's ratio and the fibre volume fraction of the type III composites are

illustrated in Figure 4-5. As can be seen, the larger the ratio of E_f/E_m, the more obvious auxetic behaviour the composites may have. With the reduction of E_f/E_m, the auxetic behaviour gradually disappears, being consistent with the experimental finding in anisotropic composites [147].

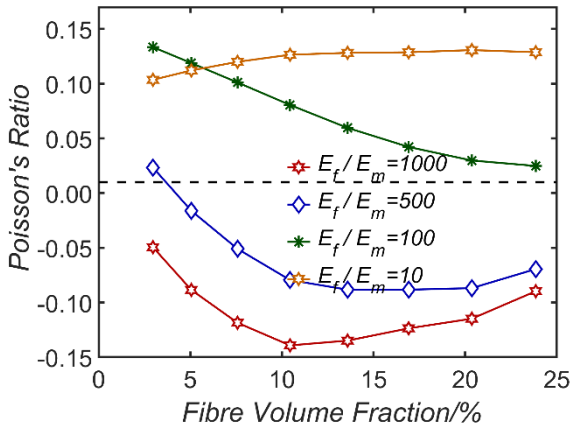

Figure 4-5. Effects of E_f/E_m on the relationship between the Poisson's ratio and the fibre volume fraction of the type III composites with $\nu_m = 0.1$, $\nu_f = 0.25$, and fibre angle $\alpha = 20°$.

4.3.4. Effects of E_f/E_m on the relationship between the Young's modulus and the fibre volume fraction of the composites

Although the focus of this chapter is on the auxetic behaviour (i.e., negative Poisson's ratio) of the solid composites, the stiffness is a very important property to enable the desired function in applications. When the fibre angle is fixed at $\alpha = 20°$, Fig. 6 shows the effects of the ratio E_f/E_m on the relationship between the Young's modulus and the fibre volume fraction of the type I composites with $\nu_m = 0.1$, $\nu_f = 0.25$. It is noted that the Young's moduli of the composites have been normalised by that of the matrix material. As can be seen, the larger the ratio E_f/E_m , the larger the Young's modulus of the composites.

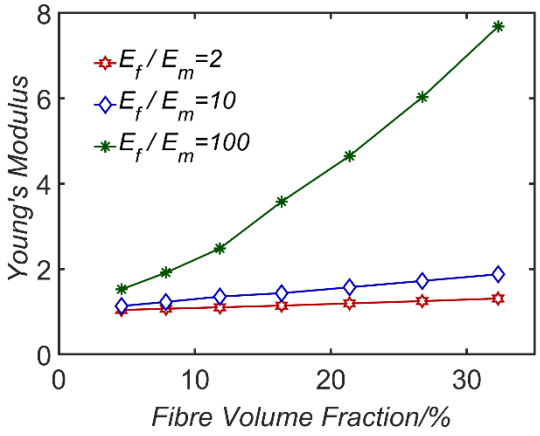

Figure 4-6. Effects of E_f/E_m on the relationship between the Young's modulus and the fibre volume fraction of the type I composites with $\nu_m = 0.1,\ \nu_f = 0.25$.

4.4 Discussion

4.4.1. Young's moduli compared to conventional particle composites

Negative Poisson's ratio has important applications and extensive research works have been done on the auxetic behaviour/properties of cellular/porous materials [80,82] and anisotropic materials [81,83,84,90,91,189]. Although cellular/porous materials [80,82] can be designed to have a large magnitude negative Poisson's ratio, they are obviously much weaker and softer compared to their counterpart solid or composite materials without any pore. Some single crystal materials [82,84,86], single layered graphene ribbons [88], and 2D puckered structure of $PdSe_2$ monolayer [89], and nanolayered graphene/Cu composites [90] also exhibit the auxetic behaviour, however, their properties are anisotropic. Moreover, they are very expensive and very hard to produce.

All the three different types of composites studied in this thesis do not contain any pore and their elastic properties are almost isotropic. Because of their negative Poisson's ratio behaviour, the unique indentation response of these auxetic composite makes them ideal materials for impact resistance applications such as helmet and body armour. As the Poisson's ratio of those composites can be tuned to zero or anywhere near zero, they can be used in biomedical application to imitate the Poisson's ratio of bones, tissue or

joints of human body. Besides, a shell with an overall Poisson's ratio of zero is optimal when object is moving in a barrel or tube because they can reduce the lateral expansion under the thrust force, thus lower the drag force. To enable the desired auxetic function in applications, the composites may need a sufficiently large stiffness. Here we compare the Young's moduli of the three different types of auxetic composites with the experimentally measured Young's moduli of their conventional counterpart isotropic particle composites [35,184,185]. Table 4-4 gives the elastic properties of the constituent materials of these conventional particle composites.

Table 4-4. The elastic properties of the constituent materials in particle composites.

Composites	E_f (MPa)	ν_f	E_m (MPa)	ν_m
SiC /Al [35]	410000	0.19	74000	0.33
Glass/Polystyrene [190]	70000	0.22	3250	0.34
Glass /Epoxy [185]	69000	0.15	3000	0.35

In order to compare the Young's moduli of auxetic interpenetrating composites with those of the conventional particle composites, the component properties E_f, E_m, ν_f, ν_m and the fibre volume fractions of the auxetic interpenetrating composites are chosen to be same as those given in table 4. Figure 4-7 shows the comparison between the Young's moduli of the three different types of auxetic interpenetrating composites and those of the particle composites, where the Young's moduli of the composites are normalised by the Voigt limit (i.e., $E_f V_f + E_m V_m$), V_f and V_m are the volume fractions of the fibre (or particle in literature) and the matrix, respectively. The fibre angles of the three types of auxetic composites are chosen as $\alpha = 20°$ for type I, and $\alpha = 12°$ for types II and III.

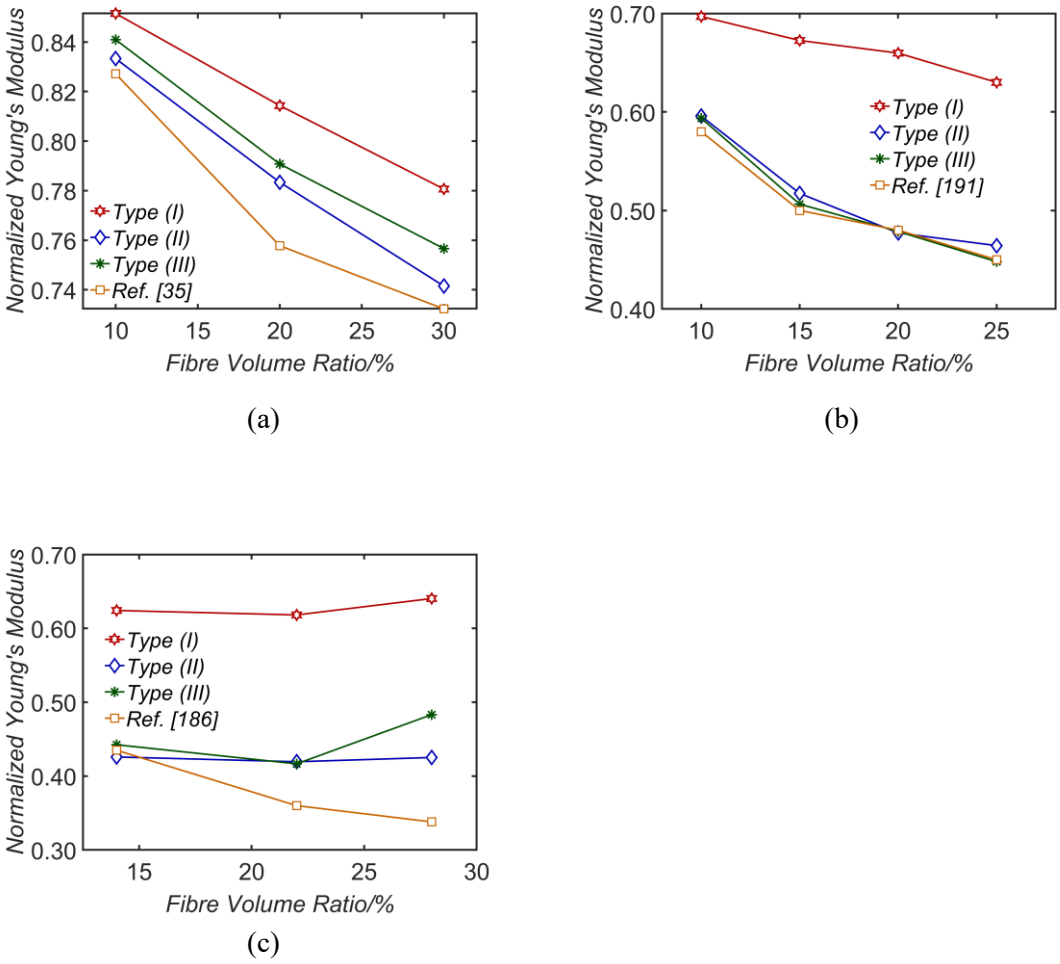

Figure 4-7. Comparison between the normalized Young's moduli of auxetic interpenetrating composites and those of the conventional particle composites. (a) with the SiC/Al particle composites [35], (b) with the glass/polystyrene particle composites [190], and (c) with the glass /epoxy particle composite [185]

As can be seen in Figure 4-7, the Young's moduli of all the three different types of auxetic interpenetrating composites are clearly larger than those of the conventional particle composites [35,184,185] ,and the type I interpenetrating composites obviously have the largest Young's moduli among the three different types of auxetic composites. Thus, the three types of composites can be used not only as functional materials (negative Poisson's ratio), but also as structural materials (high stiffness). It is noted that the stiffness of auxetic composites is usually smaller than that of non-auxetic interpenetrating composites. For example, the interpenetrating composites reinforced by a self-connected fibre network with a cubic lattice structure [75] which could have

an almost isotropic Young's modulus much larger than the Voight limit. Moreover, composites [74] reinforced by a perfect regular closed-cell foam with identical cubic cells of a uniform wall thickness are almost isotropic, and have the largest Young's modulus compared to any other type of isotropic composites.

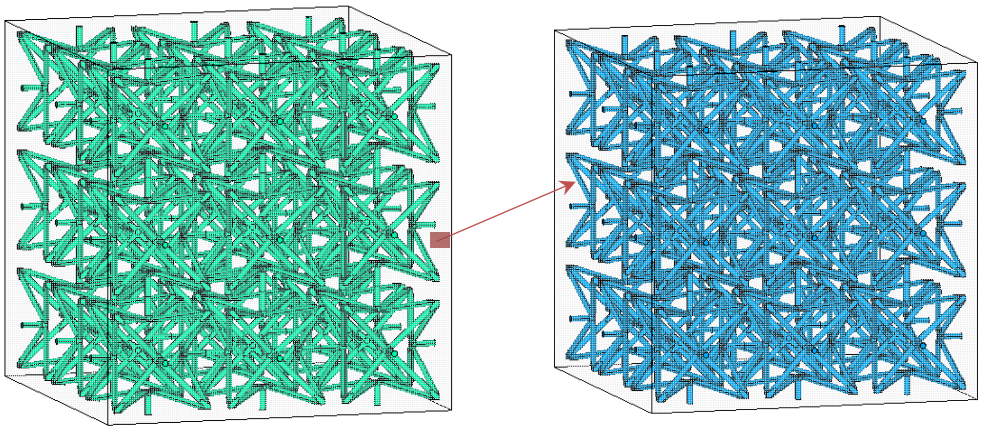

(a) level-2 composite (b) level-1 Composite

Figure 4-8. Illustration of the type-III hierarchical and self-similar composite in which the 'matrix' of the level-2 composite (a) is the level-1 composite (b).

4.4.2. Self-similar structures and structural hierarchy to enhance auxetic behaviour

Structural hierarchy has been demonstrated to be able to significantly enhance the mechanical properties of composites [74,75]. Here, the three types of interpenetrating composites can be assumed to be hierarchical and self-similar with a few levels of structural hierarchy, and the 'matrix' in a higher-level composite is made of the similar lower-level composite, as shown in Figure 4-8. The Young's modulus and Poisson's ratio of the three types of level-1 composites, in which the matrix is a single-phase solid material, are already obtained as illustrated in Figure 4-3 to Figure 4-7. To demonstrate the effects of structural hierarchy, we use the type III hierarchical and self-similar composites with a fixed fibre angle of $\alpha = 20°$ as example. The level-1 composite is made of two different single-phase solids, and their elastic properties are

$E_f/E_m = 1000$, $\nu_m = 0.1$ and $\nu_f = 0.25$. For the level-2 composites, the main strengthening fibre network is made of the same solid material (i.e., $E_f/E_m = 1000$ and $\nu_f = 0.25$) and the 'matrix' is made of self-similar level-1 composite whose Young's modulus and Poisson's ratio are obtained by simulation. Thus, the Poisson's ratio of the level-2 and level-3 hierarchical and self-similar type III composites can be obtained as shown in Figure 4-9. As can be seen, structural hierarchy can significantly enhance the auxetic behaviour of the composites and their negative Poisson's ratio could reach a large magnitude.

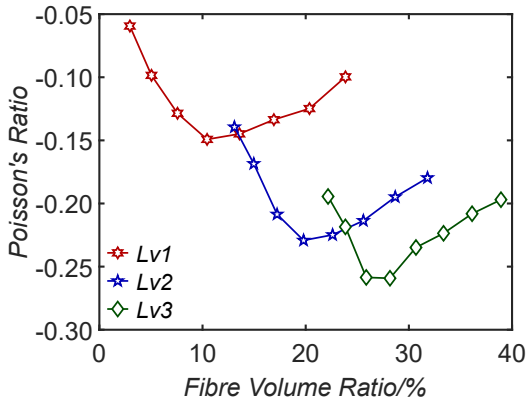

Figure 4-9. The relationship between the Poisson's ratio and the fibre volume fraction of hierarchical and self-similar type III composites with a fixed fibre angle of $\alpha = 20°$.

4.4.3. Possible explanation of different trend of auxetic behaviour with the concavity

As Figure 4-4 showed, a smaller fibre angle leads to more significant auxetic behaviour under small deformation in Type I and II. This is probably because when model (a) and (b) with different angle α are stretched within a same small deformation, a smaller fibre angle α will results a relatively larger deformation in the cross point of the fibres, leading to a larger deformation in the transverse section surfaces. As illustrated in Figure 4-10, three different lines represents the fibre located below the cubic RVE surfaces. If the fibre length is unchanged, the orbit of middle point of the fibre during deformation process is the circle located in the centre of the RVE facet. The same

longitude deformation a causes deformation of the fibre connection point b and c in small and large fibre angle α, seperately. It is obvious that $b > c$. Furthermore, the fibres with small angles are more closing to the RVE surface of the matrix. That may also enable the negative Poisson's ratio behaviour to be easier to occur.

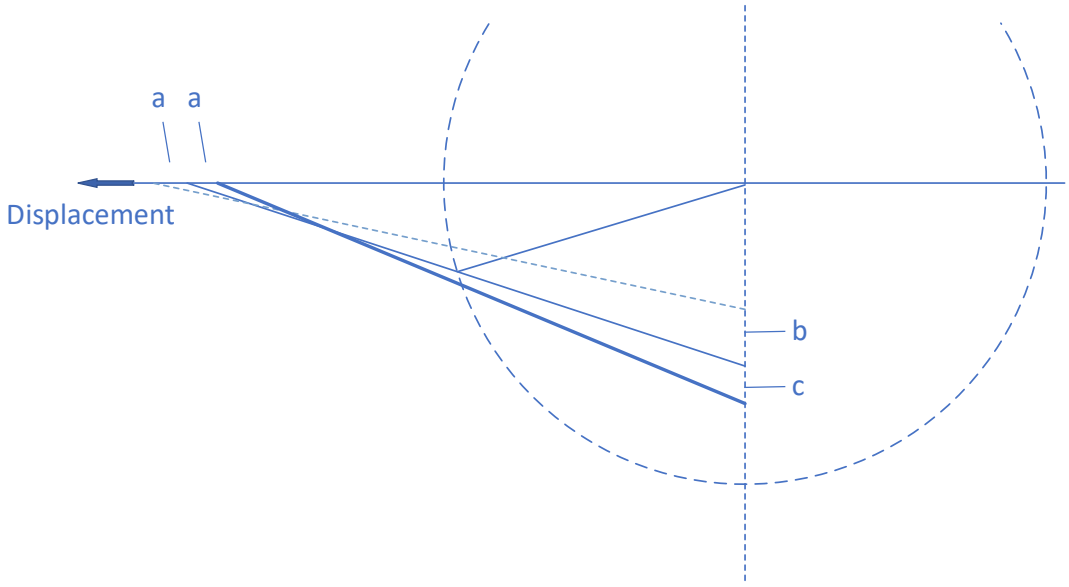

Figure 4-10. Illustration of fibre angle influence in Type I and Type II. Three different straight-line shapes in white represents the fibre located below the cubic RVE surfaces. The fibres are stretched more likely in the surface. With the same initial displacement a, the smaller fibre angle structure gets the larger overall deformation.

Conversely, larger absolute value of negative Poisson's ratio appears when the fibre angle is small in Type III. The reason for this phenomenon lies in the existence of face links. The face link is the only connection part between RVEs and the deformation of most RVEs begin at the face links when load is applied at the boundary of the composite structure. When tensile displacement load is applied, the deformation begins from the fibre connection point in the centres of the facets of each RVE. Based on the same analysis of auxetic structure Type I and Type II, the same longitude deformation a are initiated underneath the centres of the facets of each RVE, driven by the face links, as shown in Figure 4-11. The deformation of the vertices of the fibre connection points b and c. It is a reversed procedure and it is obvious that $c < b$. Moreover, the auxetic structure fibres in each RVE are relatively more 'deeply' embedded in the matrix and linked together by face links. Thus, the influence of the relative positions of fibres and

matrix are weakened compare to Type I and II. The larger fibre α causes a more intense negative Poisson's ratio behaviour.

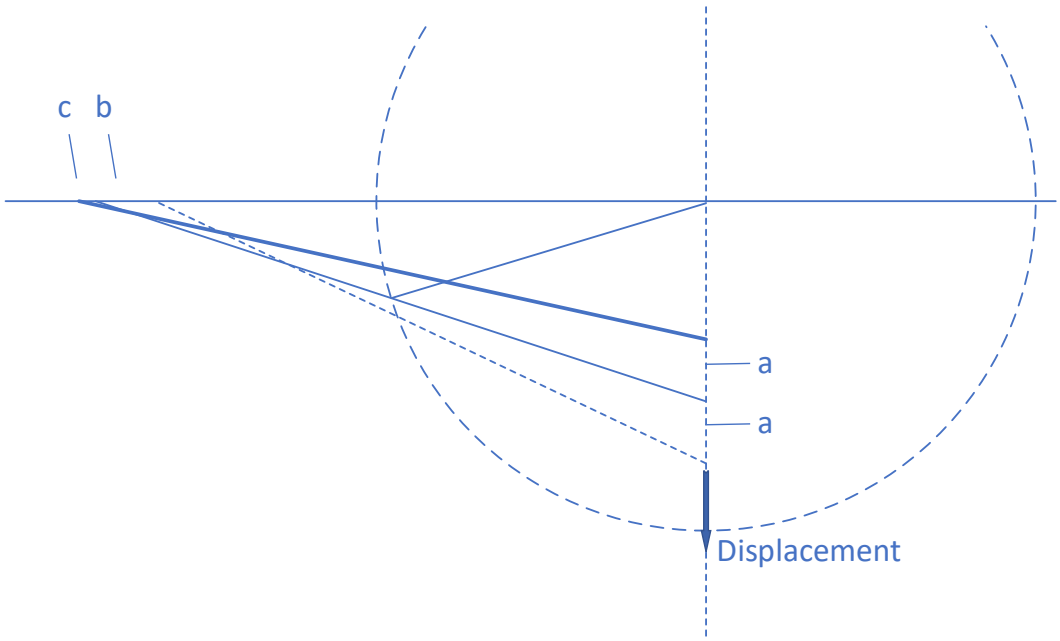

Figure 4-11. Illustration of fibre angle influence in Type III. Three different lines represents the fibre located below the cubic RVE surfaces. The connection point of the fibres is where the initial deformation begins. With the same initial displacement a, the larger fibre angle structure gets the larger overall deformation.

4.5 Conclusion

Most materials with a negative Poisson's ratio are either cellular/porous materials or highly anisotropic materials. Solid interpenetrating composites reinforced by three different types of fibre-networks are studied in this Chapter. The geometric structures are modelled by Boolean operations and meshed with full solid elements. The results of the Poisson's ratios of different structures show they all could have either a positive, or a negative, or a 'zero' Poisson's ratio. The magnitude of the Poisson's ratio depends on the combination between the fibre angle α, the type of the fibre-network, the fibre volume fraction, and the mechanical properties of the component materials: E_f/E_m, ν_f and ν_m. The degree of auxetic behaviour of the composite grows as E_f/E_m increases. The fibre angle α represents the concavity of the lattice reinforcement. A larger fibre

angle α can lead to large absolute value of negative Poisson's ratio in type I and type II structures, while a small fibre angle α can do the same in type III structure.

As the composites do not contain any pore in structure and the strengthening phase is a self-connected network, the Young's moduli of the three types of composites are obviously larger than those of the porous auxetic materials and conventional particle composites.

In addition, as all the three types of composites have cubic symmetry, their mechanical properties are almost isotropic. Moreover, structural hierarchy can significantly enhance the auxetic behaviour of the composites. Therefore, the three different types of auxetic interpenetrating composites could be used not only as functional materials, but also as structural materials in engineering applications.

Chapter 5 3D Voronoi network reinforced interpenetrating composites

5.1 Introduction

Although additive manufacturing gives us the possibility to precisely control the architectures and microstructures of materials, most of the open foams and fibre reinforced composites existing in nature or fabricated by other alternatives have randomly connected fibre network microstructures. The simplest way to model the random open foams and reinforcements in composites is based on idealised unit-cell structures. Simplified RVEs was used to predict the mechanical properties of open foams and composites. Warren *et al.* [191] presented a prediction of linear elastic properties of open-cell foams by single tetrahedral unit cell with four half-struts of length L in 1988. Nine year later in 1997, Warren *et al.* [192] studied the linear elastic behaviour of the Kelvin foam, which consists of 14-sided polyhedral cells containing six squares and eight hexagons, with open cell. A series of detailed research has been done by Zhu *et al.* [158,193,194] about the elastic properties, high strain compression analysis, and creep of open-cell foams with Kelvin open cells. However, a significant disadvantage of the unit-cell modelling approach is that it does not account for the natural variations in microstructure that are typical for most foam structures.

Modelling the real structures for the RVEs by random inclusion/fibre distribution methods is considered an improved approach to analyse the mechanical properties of composites than representing it with simple regular structures, as the random fibre distribution is closer to what the pattern of structures really like in most cases except additive manufacturing. For composites reinforced by unidirectional fibres, Yang *et al.* [195] modelled a non-uniform spatial arrangement of fibre reinforcements to generate the RVE of a ceramic matrix composite in 1997. The distribution of fibres in the transversal cross-section of the unidirectional fibre reinforced composite can be created by random sequential expansion [196] and random fibre removal [197]. For randomly

created fibres and its composites, novel fibre generation methods such as element-carving [198], and other different techniques [199–201] were introduced to model the random fibre distributions in different types of composites. The experimental image such as scanning electron microscopy and X-ray tomography could be as references in modelling the random fibre distribution in the open-cell foams and composites. 3D probabilistic model of fibres with random horizontal and vertical orientation θ and φ between 0 and π was generated based on structural information obtained from experiments. The fibre curve is generated by Kochanek's algorithm [202]. This model was used to represent the microstructure of fibrous networks in low density wood-based fibreboards [203].

Among various techniques, Delaunay triangulation and Voronoi tessellation are still the most popular and effective way to model a fabricated interpenetrating composite. In mathematics and computational geometry, a Delaunay triangulation for a given set **P** of discrete points in a plane is a triangulation DT(**P**) of the convex hull of the points in which every circumcircle of a triangle is an empty circle, that is to say, no point in **P** is inside the circumcircle of any triangle in DT(**P**). Delaunay triangulation is named after Boris Delaunay for his work on this topic from 1934 [204]. Delaunay triangulation of a random point set $\mathbf{P}_r$ is proper to represent the randomly connected fibre network as it maximizes the minimum angle of all the angles of the triangles in the triangulation. Thus, the fibres created based on the Delaunay triangulation of $\mathbf{P}_r$ could avoid triangles with extremely acute angles, hence a long/thin shape, which does not match the real circumstance and has undesirable properties when loading on a certain direction. A typical 2D Delaunay triangulation of 10 random points is shown in Figure 5-1. The circumcircles are shown in light grey colour. It can be seen that no point is inside the circumcircles of any triangle. For a set **P** of points in the 3D space, a Delaunay triangulation is a triangulation DT(**P**) such that no point in P is inside the circumsphere of any d-simplex in DT(**P**). As Delaunay triangulation can be done in 3D space, it can also be used to model the reinforcements of 3D composite materials.

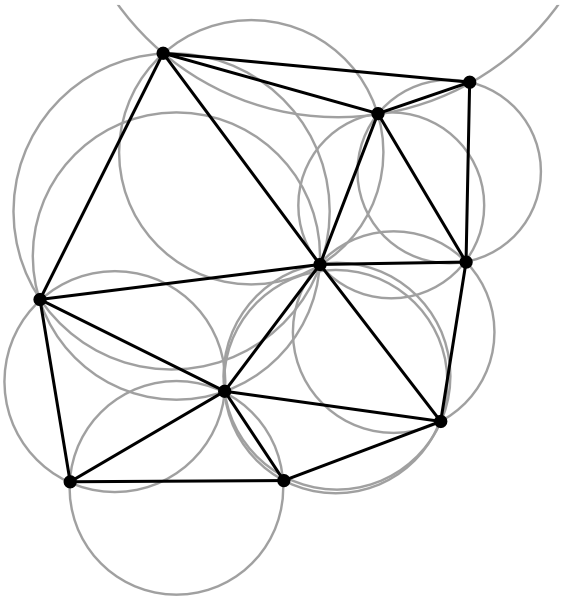

Figure 5-1. A 2D Delaunay triangulation of 10 random points with circumcircles shown.

The circumcentres of Delaunay triangles are the vertices of the Voronoi tessellation, which is also called Voronoi diagram or Voronoi partition. Figure 5-2 (a) shows the centres of circumcircles in red of the Delaunay triangulation DT(**P**) of a set of points **P**. Voronoi cells are shown in Figure 5-2 (b) in red as closed convex hulls of the points.

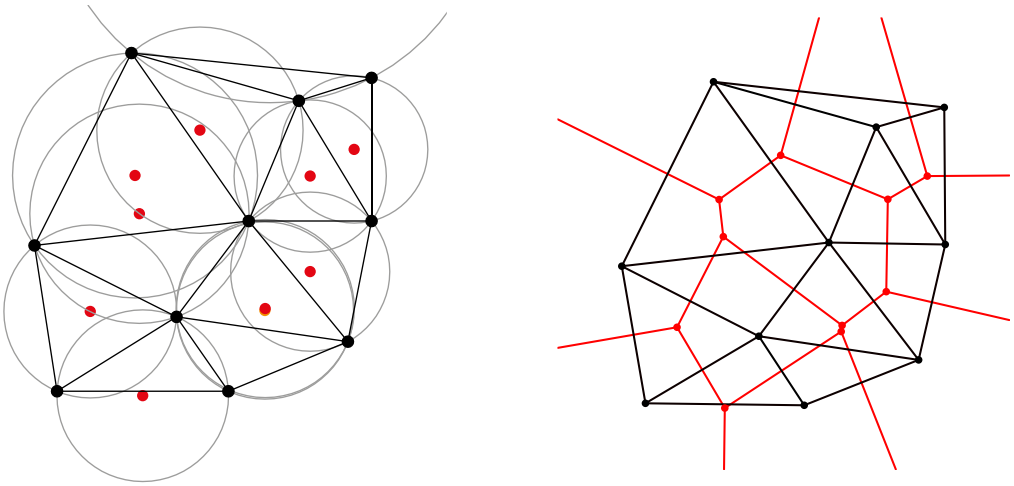

(a) (b)

Figure 5-2. (a) Delaunay triangulation with all the circumcircles and their centres (b) Voronoi diagram can be generated by connecting the centres of the circumcircles

In the schematic diagram of a 2D Voronoi tessellation of 1.0×1.0 box as Figure 5-3 shows, a finite set of points $\{p_1, ..., p_n\}$ in the plane are given. For each point p_i, its corresponding Voronoi cell R_i consists of every point in the plane whose distance to p_i is less than or equal to its distance to any other p_i. Or more precisely,

$$R_i = \{x \in \boldsymbol{X} | dist(x, p_i) \leq dist(x, p_j)\}, (i \neq j) \quad (5.1)$$

$\boldsymbol{X}$ is a metric space with distance function *dist*, in this chapter *dist* is the Euclidean distance function (Different distance functions to define various variations of Voronoi diagrams, for example Manhattan distance). Voronoi diagram is named after George Voronoy for his work on this domain from 1908 [205].

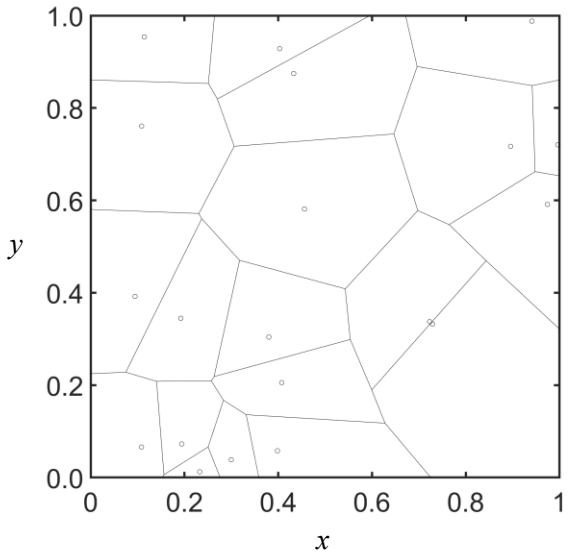

Figure 5-3. Schematic diagram of a 2D Voronoi tessellation of 20 random points with x, y coordinates from (0,0) to (1,1).

Based on similar definition, 3D Voronoi cells can be generated. A 3D Voronoi RVE containing a set of 64 points is shown in Figure 5-4.

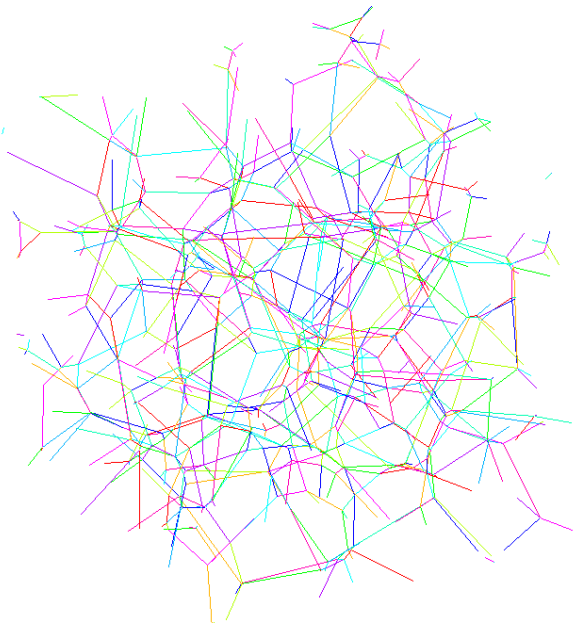

Figure 5-4. 3D Voronoi cells generated with 64 site points.

Van der Burg *et al.* [206] modelled foam structure by random Voronoi cells using finite element analysis. They started from regular body-centred cubic (BCC) and face-centred

cubic (FCC) lattice nuclei distributions, subsequently gave the nuclei positions an increasing random offset and constructed the random structure using the Voronoi procedure. Open-cell foams were depicted by Voronoi tessellation in order to investigate the effect of cell irregularity on the elastic properties of open foams [109]. Voronoi model was used to model the microstructure of fibrous materials and it is found that the strength of the fibrous material was linearly proportional to its volume fraction [207]. Voronoi model is also suitable for random fibre networks with crosslinks and inter-fibre adhesion. Negi and Picu [208] demonstrated that 2D networks of Delaunay and Voronoi suited the prediction of mechanical behaviour of these kind of materials. Lake *et al.* [209] and Zhang *et al.* [210,211] have proposed a 3D isotropic two-phase numerical model of collagen-agarose tissue in which a non-periodic Voronoi network is generated to represent collagen and a neo-Hookean solid to represent the matrix. An algorithm based on event-driven molecular dynamics theory was developed to rapidly generate periodic RVEs, and this technique is used to generate Voronoi RVEs for composite [212].

In this chapter, the microstructure of a randomly connected fibre network is modelled via controlled 3D Voronoi tessellation for periodicity. Assemble the fibre network with solid matrix, RVEs of 3D Voronoi two-phase interpenetrating composites with perfect periodicity are created. Automatic searching & coupling technique is used to speeds up the modelling of IPCs with large numbers of Voronoi fibres. The elastic properties of the 3D Voronoi fibre network reinforced IPCs are predict via finite element analysis. The effect of numbers and irregularity of the Voronoi fibres in an RVE on the mechanical properties of the composite is discussed. Moreover, the influence of mechanical properties of the constituent materials to those of the IPCs is considered.

5.2 Geometric structures and computational methods

5.2.1 Voronoi fibre network construction

In this chapter, we intend to create an isotropic 3D Voronoi fibre network reinforced IPC. Cubic RVEs with a length L is selected for periodicity of the materials. In real foams, the cross-section of the struts is a plateau border and the area of the cross-section is variable along the strut length, thickening continuously as the vertices are approached. For simplicity of the model, all the struts are assumed to have the same and constant plateau border cross-section with diameter d. Uniformly distributed random numbers are generated in an $L \times L \times L$ cubic RVE space for the x, y, and z coordinates of the first point for Voronoi tessellation. After the first point is specified, each subsequent random point is accepted only if it is greater than a minimum allowable distance δ from any existing point, until required number of points n are seeded in the cube. The point set w_0 consists of n points is copied to the rounded $(3 \times 3 \times 3 - 1)$ cubic spaces to form an $3L \times 3L \times 3L$ RVE construction space for fibre periodicity. A new point set w of $27 \times n$ points is formed and then the Voronoi tessellation is executed based on the new point set w. A simplified 2D version of this technique are also demonstrated for illustration, as Figure 5-5 (b) shows. The $3L \times 3L$ RVE construction area containing 3×3 cubic squares.

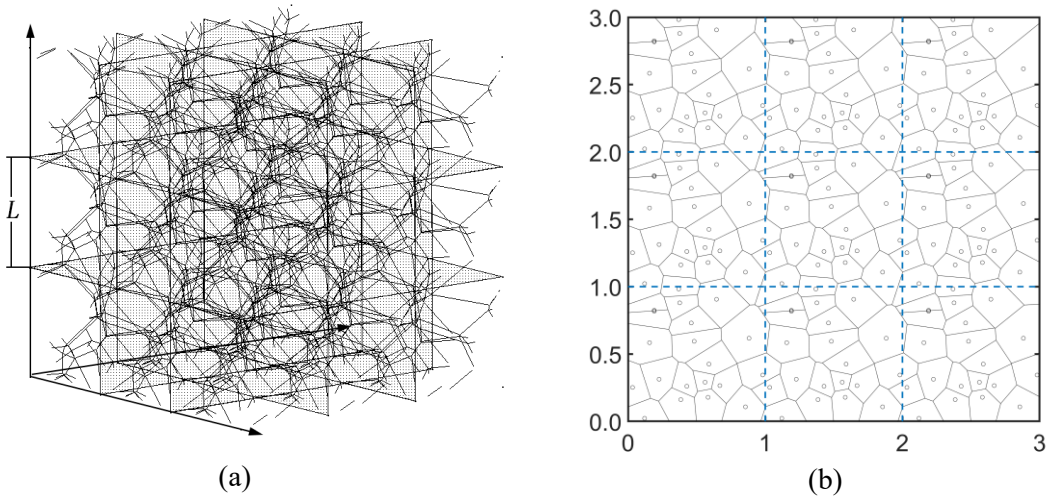

(a) (b)

Figure 5-5. The Voronoi diagram of points in construction areas. The points are copied from random RVE to (a) $3 \times 3 \times 3$ cubic spaces and (b) 3×3 square areas.

As the distribution of points in each cubic area of the $3 \times 3 \times 3$ cubic spaces are copied form the middle one, they are the same. Thus, this technique ensures the perfect fibre reinforcement periodicity on every six facets of the middle RVE.

The uniformly distributed random Voronoi points are generated in $3L \times 3L \times 3L$ space in MATLAB. After this, two different ways to give the points a Voronoi tessellation and to put the tessellation results into ANSYS APDL automatically are achieved. The first one is to generate the Voronoi tessellation via a random search method. The Voronoi tessellation and APDL coding is completed in MATLAB. The second alternative draws the help from the QuickHull algorithm for convex hulls [213]. A free convex hull software QHull from qhull.org is used to quickly compute the Voronoi diagram of the point sets generated. Then the results of Voronoi diagram are sent into ANSYS via APDL codes for RVE modelling and solving. As the point set size is not very big for the QuickHull algorithm, the time saving is not obvious.

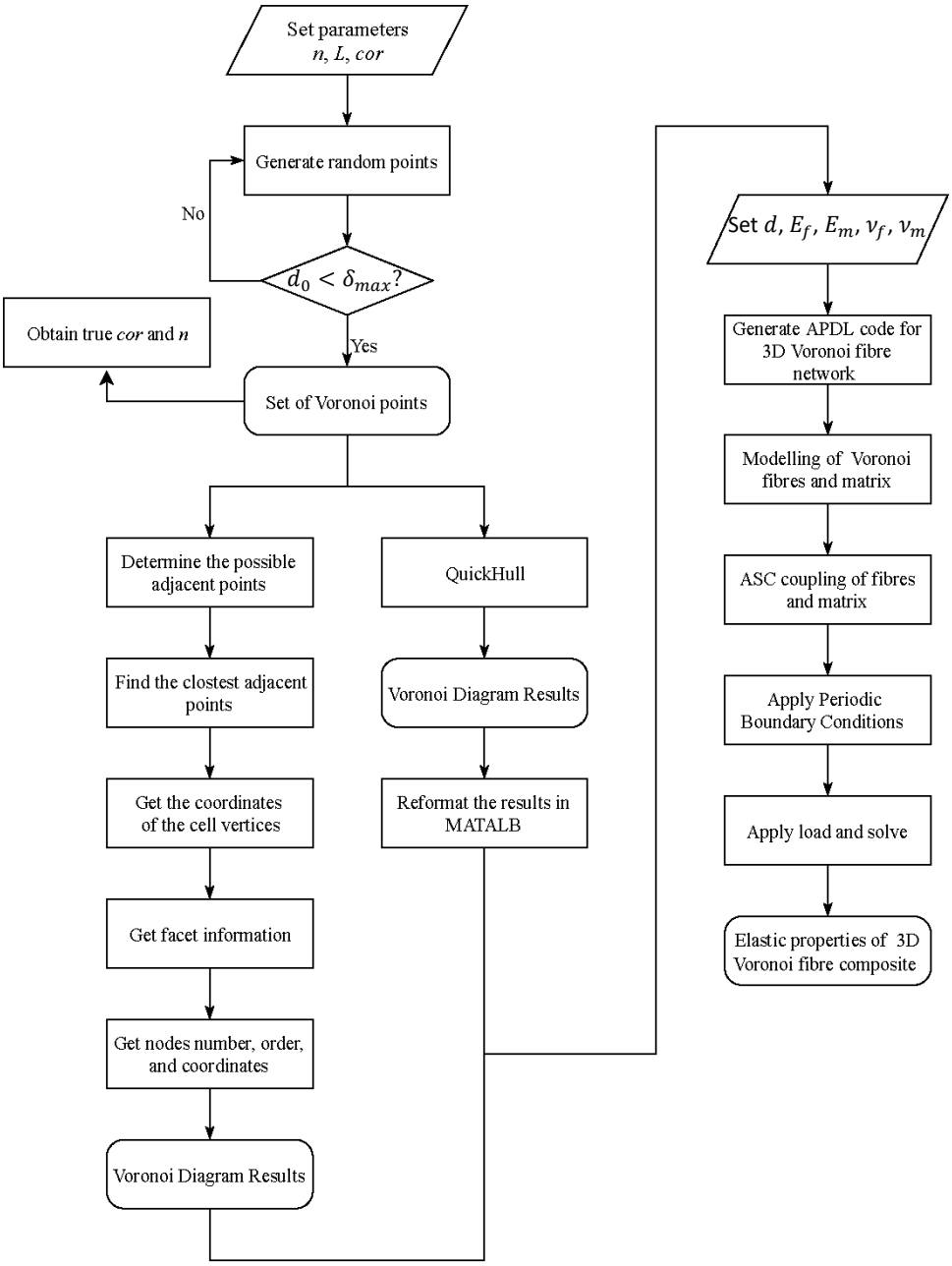

Figure 5-6. Flowchart of build the 3D Voronoi fibre reinforced composites RVE and calculate them in ANSYS.

5.2.2 Coefficient of regularity

As mentioned before, a minimum allowable distance δ is introduced to control distance between the points seeded for Voronoi tessellation. δ can be used to control the degree of irregularity. A fully regular 3D Voronoi tessellation is effectively a cubic lattice of

tetrakaidekahedral cells. To construct a regular lattice with n identical tetrakaidekahedral cells in the volume V_0, a minimum distance d_0 between any two adjacent points is given by [109],

$$d_0 = \frac{\sqrt{6}}{2}\left(\frac{V_0}{n\sqrt{2}}\right)^{1/3} \tag{5.2}$$

To obtain n cells by tessellating a space of volume V_0 with Voronoi tessellation, the maximum δ should be less than d_0; otherwise, it will result in a lack of cells. In this cubic RVE case, to construct a random Voronoi tessellation with n cells in an $L \times L \times L$ cubic RVE space, the maximum δ should be

$$\delta_{max} = \frac{\sqrt{6}}{2}\frac{L}{2^{1/6}n^{1/3}} \tag{5.3}$$

The coefficient of regularity a 3D Voronoi tessellation with n cells in an $L \times L \times L$ cubic RVE space can be denoted as

$$cor = \frac{\delta}{\delta_{max}} \tag{5.4}$$

For a fully regular Voronoi tessellation with tetrakaidekahedral cells, $cor = 1$; while for a completely random one, $cor = 0$; The method to define coefficient of regularity coincident with the Voronoi network regularity control in reference [109].

5.3.3 Pre-process techniques for finite element analysis

The 3D Voronoi network is designed as the reinforcement of the composite structure. Beam elements is used to represent the 3D Voronoi fibre reinforcement instead of solid elements used in the previous 2 chapters. If two or more solid cylinder struts crosses with a small angle, e.g. less than 10°, cross section surfaces of curved silver triangles with very sharp angles will be created. The meshing quality to both fibres and the matrix would be very low with solid elements due to the sharp surfaces introduced in some of the joints of the fibres at the vertices of Voronoi cells with small angles. Manually control those angles are possible, but not coincident with really reinforcement foam fabricated. Moreover, the test shows that even a model with 50 fibres, which is far from enough to establish a transversely isotropic structure, generates approximately 1~2

million solid elements [214]. Such many elements dramatically increase the pre-processing time and slow down the computing speed. Therefore, beam element is a better option in representing Voronoi fibres with much fewer meshing elements. As there are no overlaps in a Voronoi fibre network, it will be discussed later that the result variation between beam elements and its solid counterparts is not significate in predicting the mechanical properties of 3D Voronoi fibre reinforced IPCs. A solid circle cross section is used to represent the diameter of the fibres. Rigid connection is applied on the vertices of the Voronoi cells to link all the fibres together. Part of a periodic 3D Voronoi fibre network generated from 27 Voronoi points meshed with beam elements is shown in Figure 5-7.

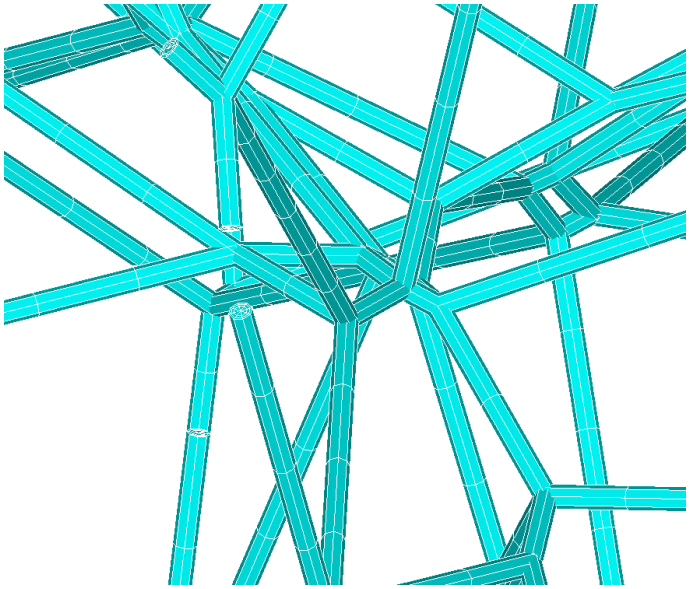

Figure 5-7. 3D Voronoi fibre network meshed with beam element. This figure is plotted from x axis perspective of the fibre network.

An $L \times L \times L$ solid cube with the same size as the RVE representing the matrix is modelled to match the 3D Voronoi fibre network. The matrix is meshed by SOLID186 cuboid elements and is embedded by the 3D Voronoi fibre network. However, the fibre network and the matrix are still independent from each other with no bond or constraint on their nodes after meshing. Constraints must be applied to the corresponding nodes of the fibre network and the matrix to ensure that they have the same translation displacements to transfer load between fibres and matrix. A two-step automatic

searching & coupling (ASC) technique [215] is applied to constrain the nodes on 3D Voronoi fibre network to the most proper nodes of the solid matrix: finding the nearest matrix nodes to every fibre nodes; then coupling the fibre nodes with the matrix nodes found.

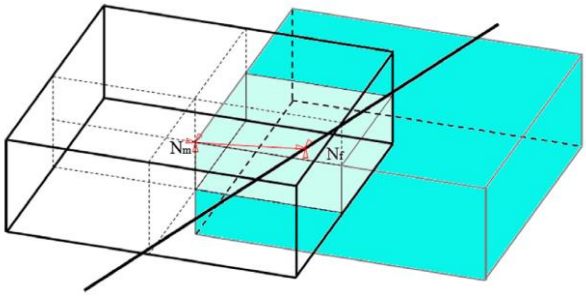

Figure 5-8. The sketch for the ASC technology [215].

As Figure 5-8 shows, N_f represent a node on one of the fibres and N_m is the corresponding node closest to node N_f. For each N_f, the node N_m is found by searching a node with the smallest distance between N_f and the nodes of the matrix. After that, each pair of nodes N_m and N_f are coupled by a constraint equation. The process can be indicated by coupling the translational degree of freedoms U_f of the node N_f and the corresponding translational degree of freedoms U_m of a matrix node N_m as

$$U_f = U_m \tag{5.5}$$

When N_m lies on the facets, edges, or vertex of an RVE, the constraint equation of periodic boundary condition is also applied on N_m and the matrix node $N_{m'}$ as

$$U_m - U_{m'} = U_j - U_{j'} \tag{5.6}$$

Where U_m and $U_{m'}$ are the translational degree of freedoms of N_m and N'_m, and U_j and $U_{j'}$ are the translational degree of freedoms of another pair of nodes which locate on the same facets of the RVE. To remove the over-constraint caused by Equation 5.5 and Equation 5.6, we substitute Equation 5.5 into Equation 5.6 to have

$$U_f - U_{m'} = U_j - U_{j'} \tag{5.7}$$

By this procedure the over-constraint is eliminated. Therefore, ASC technique can avoid the conflict between PBC and the fibre/matrix nodes coupling, and PBC can be successfully applied on the RVEs. By the aforementioned procedures the fibre network and matrix are assembled together, and the interpenetrating composite is constructed. In order to compensate the additional stiffness introduced by the beam element representing the fibres embedded in the solid element representing the matrix, the Young's modulus of fibre is modified as reference [215] shows

$$\overline{E}_f = E_f - E_m \tag{5.8}$$

A simple validation is conducted by using a composite structure with only one beam in the middle of a cubic RVE. Both the ASC technique and full solid model as Figure 5-9 shows are used to compare the Young's moduli results. $E_m = 1$, $E_f = 10$, $\nu_m = 0.3$ and $\nu_f = 0.2$ are used in this validation. The element size of the fibres and the matrix are denoted as es_f and es_m. In this case, es_f=2 and es_m=1.

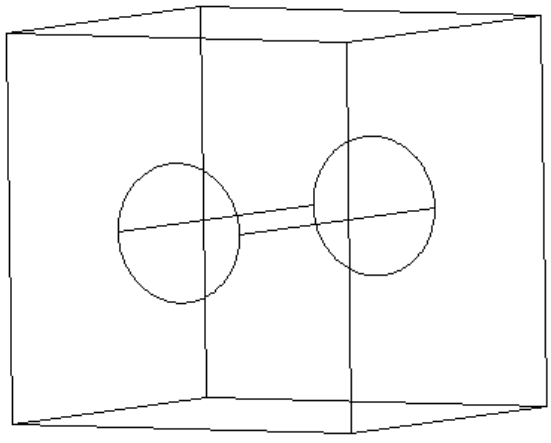

(a)

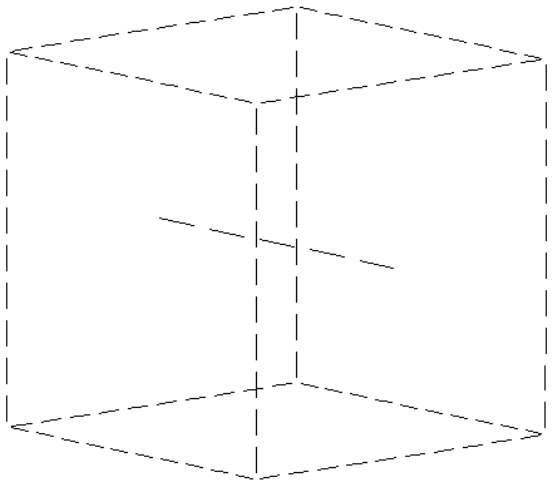

(b)

Figure 5-9. Simple validation model with single beam in the cubic matrix. (a) full solid model. (b) ASC model.

With the same denotation in Chapter 3, a small uniaxial translational load of 0.1% of the RVE length L along x axis is applied on face F_{xp} of both ASC model and solid model. The opposite face F_{xn} is fixed.

The results of the Young's moduli of the composite are listed in Table 5-1 below.

Table 5-1. Validation results of Young's moduli obtained from ASC and full solid model.

Volume fraction / Model	5%	10%	15%	20%	25%	30%
Full solid	1.4507	1.9013	*2.3518*	2.8022	3.2525	3.7028
ASC	1.4824	1.9321	2.3817	2.8314	3.2810	3.7307
Difference	2.19%	1.62%	1.27%	1.04%	0.88%	0.75%

It can bees seen from the results that the difference between full solid model and ASC technique is around 1% to 2%, which is acceptable.

It is also necessary to take the accuracy of bending into consideration when using ASC technique.

To validate this, a small normalized uniaxial force load of 1 on face F_{xp} along z axis is applied on face F_{xp} of both ASC model and solid model. The opposite face F_{xn} is fixed. The results of the displacement along z axis on face F_{xp} are listed in Table 5-2 below.

Table 5-2. Validation results of Young's moduli obtained from ASC and full solid model.

Volume fraction / Model	5%	10%	15%	20%	25%	30%
Full solid	1.2350	1.0833	0.9368	0.8024	0.6870	0.5904
ASC	1.2158	0.9667	0.8373	0.6872	0.5741	0.4730
Difference	1.58%	8.33%	11.88%	16.76%	19.66%	24.82%

It can bees seen from the results that the difference between full solid model and ASC technique varies from 1.6% to 24%. It is acceptable when the fibre volume fraction is smaller than 20%.

An RVE of 3D Voronoi fibre network created by 64 Voronoi points is show in Figure 5-10 (a). RVE of 3D Voronoi fibre network constrained with the matrix created by 12 Voronoi points is show in Figure 5-10 (b).

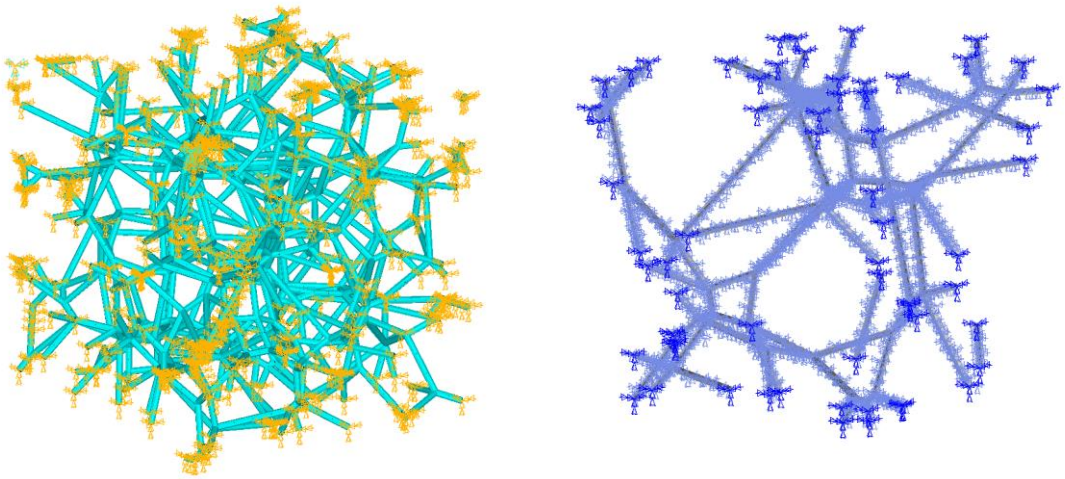

(a) (b)

Figure 5-10 RVE of 3D Voronoi fibre networks: (a) 3D Voronoi fibre network created by 64 Voronoi points. The rotational degrees of freedom of the beam element nodes on facets, edges and vertices of the RVEs are constrained, shown in yellow. (b) 3D Voronoi fibre network created by 12 Voronoi points. This small points number is selected to show to ASC coupling (in light blue) of the fibre nodes to the matrix nodes (not shown).

A general periodic boundary condition is added at each vertex, edge, and facet of the cubic RVE, as Chapter 3.2 showed. In addition, it is worth to mention that the nodes created by solid elements have no rotational degrees of freedom. However, the nodes created by beam elements outputs both translations and rotations after solving. As there are six degrees of freedom in beam fibres while only three degrees of freedom in the solid matrix, the rotational degrees of freedom of the fibre nodes which are couple on the facets, edges or vertices of the RVEs have to be constrained in the same periodic way as the translational degrees to achieve a perfect PBC.

In order to predict the elastic performance of the composites by tracking how Young's Modulus of the composite E_c is affected by different constituent material properties and volume fractions. $E_m = 1$ is assumed for generality and simplicity.

The parameters used in this chapter are listed in Table 5-3.

Table 5-3. Parameters of constituent materials for the elasticity of 3D Voronoi reinforced IPCs.

E_f	5	10	50	100	
ν_f	0.1	0.2	0.49	0.05	0.05
ν_m	0.3	0.3	0.05	0.49	-0.8
VF_f	1%	5%	10%	15%	20%

5.3 Results

5.3.1 Accuracy and mesh sensitivity of ASC technique

The coupling quality of the nodes of the fibres and matrix is largely affected by the element size. When meshed with large elements, it is more possible that the distance between closest N_m for N_f is too far to obtain proper results. However, the element size used in mesh cannot be too small as the solving time of the model is unacceptable for a very large meshed model. RVE length $L = 30$ is used in all these Voronoi fibre networks. To give an overview of the effect of element size used in the mesh of fibres and matrix on the mechanical properties of the composite, different combinations of es_f and es_m are considered in this section. Instead of different sizes of element used in the matrix and fibres, the ratio between the fibre and matrix is what matters most. The ratio between the element sizes of matrix and fibre with the length of the cube affects the result as well. Different element sizes of the fibres with beam elements are given in Table 5-4, while the element size of the matrix is set as 1. The coefficient of regularity is chosen to be $cor = 0.5$. The number of Voronoi points and cells presenting the number of fibres and volume fraction used in the mesh sensitivity check are $n = 4 \times 4 \times 4 = 64$ and $f_f = 10\%$, respectively. The other parameter such as mechanical properties of the constituent materials are specified as $E_m = 1$, $E_f = 100$, $\nu_m = 0.3$ and $\nu_f = 0.1$.

Table 5-4. Element sizes used in Mesh Group 1

Mesh Number	*Mesh 1*	*Mesh 2*	*Mesh 3*	*Mesh 4*	*Mesh 5*	*Mesh 6*	*Mesh 7*	*Mesh 8*	*Mesh 9*	*Mesh 10*
es_f	0.0625	0.125	0.25	0.5	1	2	4	8	16	32
es_m	1	1	1	1	1	1	1	1	1	1

With the element size combination of Mesh Group 1 shown in Table 5-4, the Young's moduli of the same RVE in *x* direction E_x are listed in Table 5-5. A more direct illustration is given in Figure 5-11 (a).

Table 5-5. Young's moduli obtained by solving the models with mesh group 1.

Mesh Number	*Mesh 1*	*Mesh 2*	*Mesh 3*	*Mesh 4*	*Mesh 5*	*Mesh 6*	*Mesh 7*	*Mesh 8*	*Mesh 9*	*Mesh 10*
Young's moduli of the composite	59.79	30.22	15.44	8.32	4.51	2.58	2.01	1.95	1.95	1.95

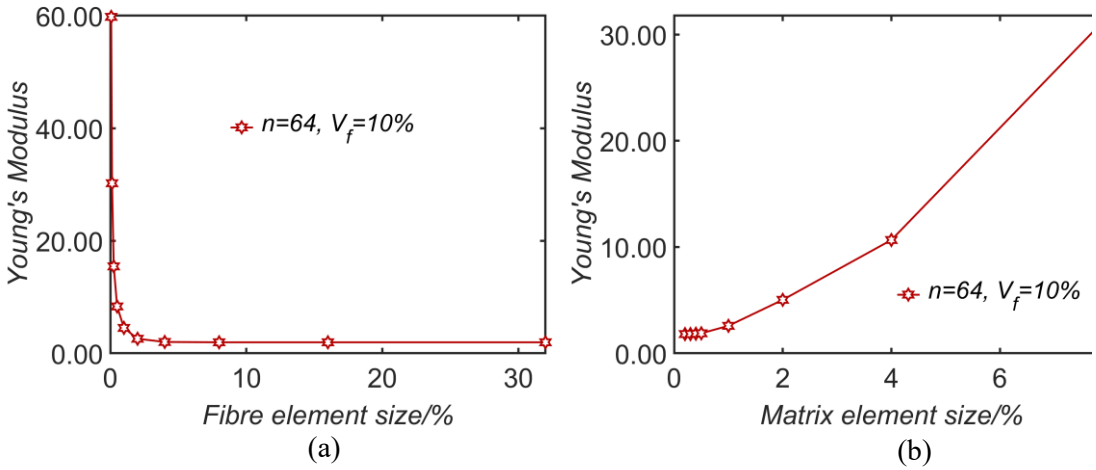

Figure 5-11. Mesh sensitivity of ASC technique for 3D Voronoi fibre network reinforced IPCs (a) Young's moduli of the composite as a function of fibre element size. (b) Young's moduli of the composite as a function of matrix element size.

It can be seen that if fibre element size is relatively small while the matrix element size is relatively large, the Young's Moduli of the composite obtained can be extraordinarily large. It is almost impossible for a random fibre reinforced composite with fibre volume fraction $V_f = 10\%$ to reach that a large number, almost 5 times larger than its Voigt limit $(E_c)_{Voigt} = 10.9$. This can be caused by the big difference between fibre element size and matrix element size, which lead to the constraint of different nodes on the fibres to the same nodes on the matrix. When the fibre element size is as small as around 0.1 while the matrix size is 1 as the mesh 1 and mesh 2 shown in Table 5-4, that means 10 nodes of the fibre will be constrained on the same node of the matrix. That is highly over constrained than that to represent a normal fibre-matrix interface, thus lead to the extreme overestimation of the fibre stiffness in Figure 5-11 a. When the fibre mesh size is large enough (larger than 5 in Figure 5-11 a), even larger than the length of most of the fibres, the fibres are all meshed with a single beam element. As the mesh condition is the same for one element per fibre, the results are steady. Another mesh group is given in Table 5-6 as the element size of the fibre remains unchanged while the element size of the matrix varies from 1/10 of the fibre element size and 4 times of the fibre element size. The results are provided in Figure 5-11 (b).

Table 5-6. Young's moduli obtained by Mesh Group 2

Mesh Number	*Mesh 1*	*Mesh 2*	*Mesh 3*	*Mesh 4*	*Mesh 5*	*Mesh 6*	*Mesh 7*	*Mesh 8*
es_f	2	2	2	2	2	2	2	2
es_m	0.2	0.3	0.4	0.5	1	2	4	8
Young's moduli of the composite	1.805	1.809	1.838	1.878	2.583	5.030	10.661	31.774

According to Table 5-5 and Table 5-6 above, rules of element size can be summarized. Firstly, a proper element size combination of the two constituent materials must be with a relatively large $es_f\ /es_m$ to make the ASC coupling nodes as close as possible. This can avoid overestimation of the elastic properties of the composite. Secondly, the es_f need to be small enough to give a good description of the fibres. Finally, as the es_f need to be small enough and $es_f\ /es_m$ need to be large, the corresponding es_m need to a small number as well. However, it cannot be too small for the FE analysis will take too long to finish solution.

Following these three rules, four different combinations of es_f and es_m are selected in Table 5-7. ASC technique with these es_f and es_m combinations are compared with pure solid models of structures Type I and Type III used in Chapter 3.

Table 5-7. Three different combinations of es_f and es_m

Combination number / Element size	Set 1	Set 3	Set 4
es_f	2	1	1
es_m	1	0.5	0.2

Figure 5-12 illustrates the RVEs of Type I and Type III built by ASC technique with beam elements for the fibres and solid elements for the matrix.

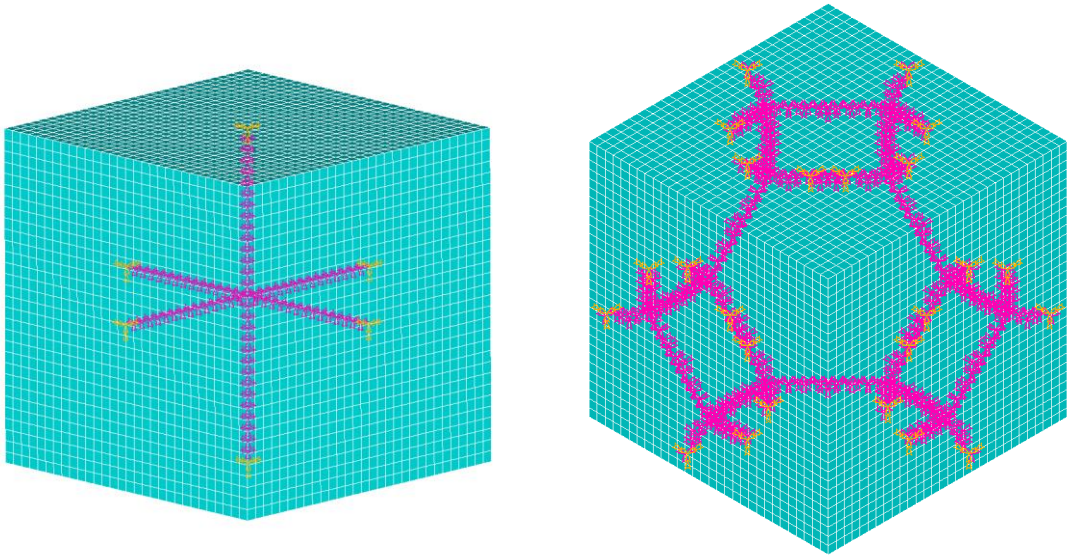

(a) (b)

Figure 5-12. Illustrations of RVEs of Type I and Type III structures built by ASC technique with beam elements for the fibres and solid elements for the matrix.

It is worthwhile to mention that Type III structure cannot be modelled with the same RVE selection as that in chapter 3 because solid element fibres can be intersected in axial direction while the beam element fibres cannot.

Figure 5-13 gives a comparison of the composite elastic moduli predicted by ASC coupled models and full solid models.

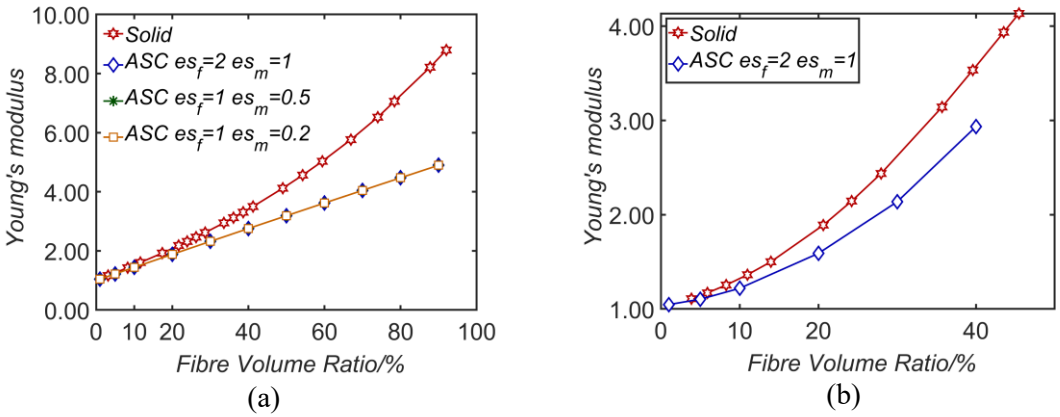

Figure 5-13. Comparisons of E_c predicted by ASC coupled models and full solid models. (a) regular structured model Type I. (b) regular structured model Type III.

In Figure 5-13 (a), the prediction of E_c under different es_f and es_m settings are almost exactly the same. However, in Figure 5-13 (a), the difference between the full solid model and ASC model becomes larger as the fibre volume fraction increases. As we only consider volume fractions between 1% and 20%, the accuracy of ASC technique is acceptable. The largest difference between the results of solid model and ASC model is less than 10% in Figure 5-13 (a) and is less than 13% in Figure 5-13 (b), when $es_f = 2$ and $es_m = 1$. The results are slight better when $es_f = 1$ and $es_m = 0.5$, but the calculations time is much longer. In summary, a combination of element sizes $es_f = 2$ and $es_m = 1$ is proper for the simulations.

5.3.2 Impact of random fibre distribution

The 3D Voronoi fibre structures are constructed by randomly generated points in $L \times L \times L$ space. All the fibre networks are different in structure with all the same parameters such as cor, fibre density and the mechanical properties of constituent materials. Therefore, the elastic behaviour of the RVEs of the composite varies from specimen to specimen. To test the impact of random fibre distributions to the elastic properties of the 3D Voronoi fibre reinforced composites, ANSYS batch model for

massive calculation is used. Means and standard variances of the elastic properties are obtained from a number of independent models with the same parameters. This will determine the Voronoi points needed to obtain a nearly isotropic RVE to represent the composite. 10 random models of the 3D Voronoi fibre network composite RVEs constructed by $n = 4 \times 4 \times 4 = 64$ and $n = 6 \times 6 \times 6 = 216$ Voronoi points are created and solved to obtain the Young's moduli of the composite. The volume fractions of the fibres are chosen as 1% and 10%. The elastic properties of the constituent materials are $E_m = 1$, $E_f = 100$, $\nu_m = 0.3$ and $\nu_f = 0.1$. The Young's moduli of the composites constructed with 64 Voronoi points with 1% fibre volume fraction are listed in Table 5-8. The standard variances St_{Var} of the Young's moduli E_{cx}, E_{cy}, and E_{cz} obtained from 10 RVEs constructed by 64 Voronoi points with 1% fibre volume fraction are around 1%, small enough to be ignored in the prediction of the mechanical properties of the composite. In addition, the standard variances between the Young's moduli E_{cx}, E_{cy}, and E_{cz} obtained from each RVEs are also small enough. Most of them are less than 1%.

Table 5-8. Young's moduli of 10 3D Voronoi fibre network composite RVEs constructed with 64 Voronoi points and 1% fibre volume fraction

	Sets										
	1	2	3	4	5	6	7	8	9	10	St_{Var}
E_{cx}	1.164	1.160	1.160	1.152	1.154	1.158	1.153	1.144	1.144	1.173	0.009
E_{cy}	1.167	1.151	1.160	1.137	1.145	1.162	1.145	1.152	1.152	1.167	0.010
E_{cz}	1.163	1.172	1.153	1.148	1.163	1.174	1.140	1.163	1.160	1.146	0.011
St_{Var}	0.002	0.011	0.004	0.009	0.009	0.008	0.007	0.010	0.008	0.014	-

For 10% fibre volume fractions, the Young's moduli of the composites constructed with 64 Voronoi points are listed in Table 5-9. From Table 5-9, the standard variances of the Young's moduli E_{cx}, E_{cy}, and E_{cz} obtained from 10 RVEs constructed by 64 Voronoi points at 10% fibre volume fraction are larger than those obtained at 1% fibre volume fraction. However, the figures are still small enough to be ignored in the prediction of

the mechanical properties of the composite. In addition, the standard variances between the Young's moduli E_{cx}, E_{cy}, and E_{cz} obtained from each RVEs are also small enough. Most of them are less than 5%.

Table 5-9. Young's moduli of 10 3D Voronoi fibre network composite RVEs constructed with 64 Voronoi points and 10% fibre volume fraction.

	Sets										
	1	2	3	4	5	6	7	8	9	10	St_{Var}
E_{cx}	2.648	2.642	2.566	2.538	2.679	2.579	2.575	2.691	2.588	2.532	0.057
E_{cy}	2.579	2.588	2.585	2.665	2.578	2.663	2.542	2.565	2.668	2.674	0.051
E_{cz}	2.637	2.502	2.553	2.586	2.655	2.652	2.659	2.635	2.655	2.700	0.059
St_{Var}	0.037	0.071	0.016	0.064	0.053	0.046	0.060	0.063	0.043	0.090	-

The Young's moduli of the RVEs constructed with same parameters but 216 Voronoi points at 1% and 10% fibre volume fractions are listed in Table 5-10 and Table 5-11.

Table 5-10. Young's moduli of 10 3D Voronoi fibre network composite RVEs constructed with 216 Voronoi points and 1% fibre volume fraction.

	Sets										
	1	2	3	4	5	6	7	8	9	10	St_{Var}
E_{cx}	1.179	1.180	1.173	1.175	1.172	1.178	1.181	1.178	1.180	1.180	0.0032
E_{cy}	1.173	1.182	1.181	1.180	1.179	1.180	1.175	1.176	1.175	1.173	0.0034
E_{cz}	1.173	1.178	1.176	1.172	1.178	1.180	1.180	1.172	1.179	1.173	0.0032
St_{Var}	0.004	0.002	0.004	0.004	0.004	0.001	0.003	0.003	0.003	0.004	-

Table 5-11. Young's moduli of 10 3D Voronoi fibre network composite RVEs constructed with 216 Voronoi points and 10% fibre volume fraction.

	Sets										
	1	2	3	4	5	6	7	8	9	10	St_{Var}
E_{cx}	2.706	2.713	2.691	2.718	2.711	2.709	2.712	2.696	2.716	2.700	0.0087
E_{cy}	2.704	2.712	2.692	2.710	2.692	2.699	2.707	2.712	2.692	2.710	0.0084
E_{cz}	2.716	2.691	2.713	2.693	2.693	2.709	2.712	2.719	2.700	2.707	0.0104
St_{Var}	0.007	0.013	0.013	0.013	0.011	0.006	0.003	0.011	0.012	0.005	-

This discussion is summarized in Figure 5-14 below. The standard variances of the Young's moduli E_{cx}, E_{cy}, and E_{cz} obtained from 10 RVEs constructed by 216 Voronoi points are relatively smaller than those obtained from 64 Voronoi points. However, the RVE model size of the 216 Voronoi points is more than 4 times larger than the RVE model size of 64 Voronoi points (16MB to 4MB). It needs to be emphasized that the solving time of the 216 Voronoi points model is more than 10 times larger than that of the 64 Voronoi points model. The standard variances between Young's moduli E_{cx}, E_{cy}, and E_{cz} also reduce from 64 Voronoi points to 216 Voronoi points. However, as the standard variances are small, but the 64 and 216 cell 3D Voronoi fibre composites can both be regarded as nearly isotropic.

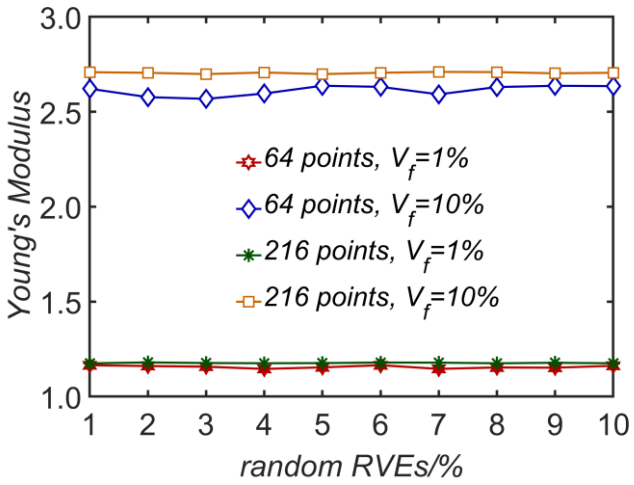

Figure 5-14. Young's moduli of 10 random RVEs from four combinations of Voronoi points and volume fractions

5.3.3 Impact of number of fibres in an RVE

In order to review the impact of fibre numbers in an RVE, composites with the same volume fraction but different numbers of Voronoi fibres in same RVEs need to be modelled. For beam elements, the volume fraction of the fibre is determined by both the total fibre length and fibre cross section diameter. The shape and dimensions of the cross section can be defined in ANSYS. It is assumed that al the fibres have the same cross section with diameter d. The total fibre length can be precisely calculated by commercial computer aided analysis software such as ANSYS before mesh is generated. Therefore, the volume fraction of the fibres can be calculated by

$$VF_f = \frac{Volume\ fraction\ of\ the\ fibres}{Total\ Volume} = \frac{l_t \times \pi \times \left(\frac{d}{2}\right)^2}{L^3} \tag{5.9}$$

where l_t is the total fibre length calculated by ANSYS after fibre entity modelling. Then the fibre diameter can be derived as

$$d = 2 \times \sqrt[2]{\frac{VF_f \times L^3}{l_t \times \pi}} \tag{5.10}$$

The influence of the intersection part is small enough to be ignored. Then we can control the fibre volume fractions of RVEs with different fibre density to be with same by define different fibre cross section diameters.

Different fibre density is achieved by build networks with different number of Voronoi points. Figure 5-15 shows the fibre density difference between four type of 3D Voronoi fibre network reinforced composites created by $n = 3 \times 3 \times 3 = 27$, $n = 4 \times 4 \times 4 = 64$, $n = 6 \times 6 \times 6 = 216$ and $n = 7 \times 7 \times 7 = 343$ Voronoi points. For transparency the matrices are not shown on the figures. Elastic properties of the constituent materials are $E_m = 1$, $E_f/E_m = 100$ and 2, $\nu_m = 0.3$, $\nu_f = 0.1$.

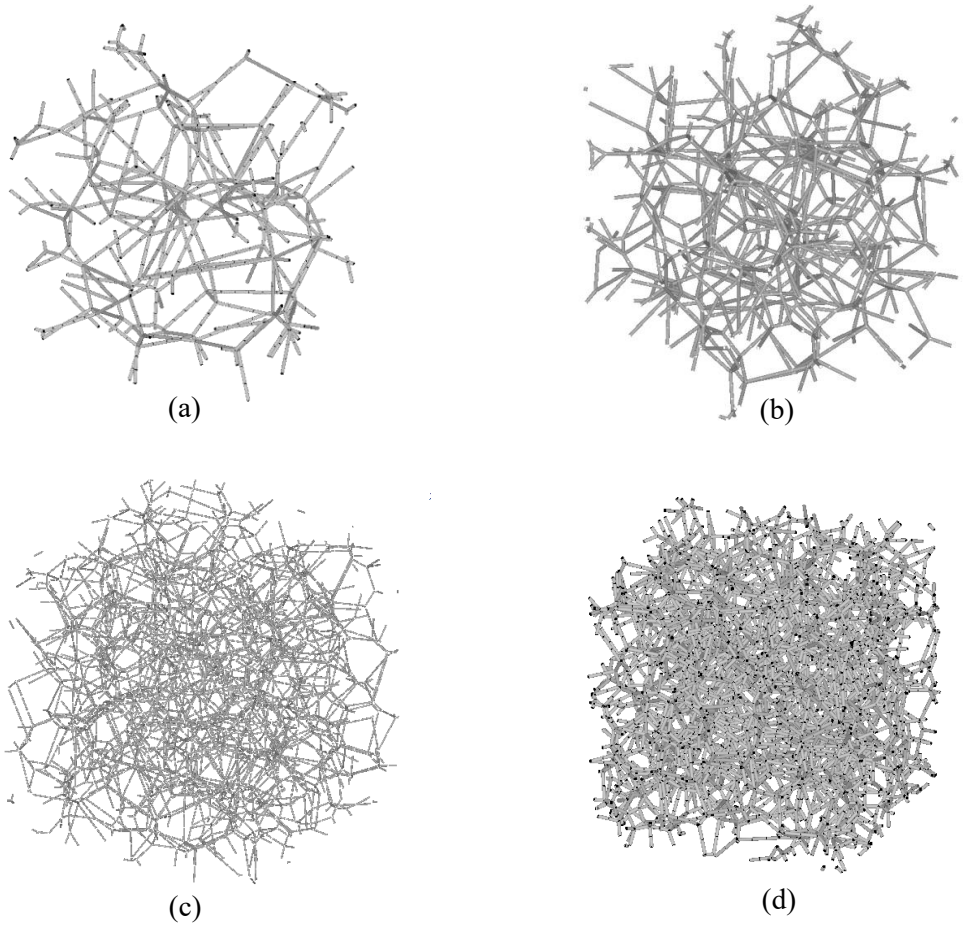

Figure 5-15. Fibre density of four types of 3D Voronoi fibre network reinforced composites created by different number of Voronoi points: (a) Type I: fibre network create from 27 points, (b) Type II: fibre network create from 64 points, (c) Type III: fibre network create from 216 points, (d) Type IV: fibre network create from 343 points.

To reach the same fibre volume fractions, the radius (*d/2*) of the fibres for each type of the four 3D Voronoi composites are given in Table 5-12. The total fibre length l_t varies in different rando models even the other parameters are the same. Therefore, the fibre diameter is also different in order to reach the same fibre volume fractions. Table 5-12 is presented regarding one of the 10 random models of each Type.

Table 5-12. Radius of the fibres in four types of RVEs of 3D Voronoi IPCs*.

	1%	5%	10%	15%	20%
d/2 Type I	0.2349	0.5253	0.7430	0.9099	1.0507
d/2 Type II	0.1768	0.3954	0.5592	0.6848	0.7908
d/2 Type III	0.1177	0.2633	0.3723	0.4560	0.5266
d/2 Type IV	0.1006	0.2250	0.3182	0.3897	0.4500

*The numbers listed above is calculated by 1 RVE under each Type and fibre volume fraction combination

The Young's moduli of each volume fraction and Voronoi points combination such as Type I 1% and Type IV 10% are all calculated by statistical average of 10 random models.

Table 5-13. Young's moduli of different types of 3D Voronoi fibre reinforced composites.

	1%	5%	10%	15%	20%
E_c Type I	1.140	1.616	2.344	3.092	3.938
E_c Type II	1.167	1.747	2.629	3.515	4.515
E_c Type III	1.186	1.869	2.716	3.786	4.805
E_c Type IV	1.206	1.906	2.905	3.951	5.091

It is noticed that the Young's moduli of the composites built with more fibres larger than those which have less fibres with same volume fractions. For example, the Young's moduli of the composites build with 216 Voronoi points are larger than those acquired from the 64 Voronoi points ones when their volume fractions are both 10%. The reason may lie in that the increase of fibres creates more contact areas. Because when two different fibre networks have the same volume, longer fibres with smaller

cross section diameters have larger surface areas. A simple schematic figure is given below as Figure 5-16 shows.

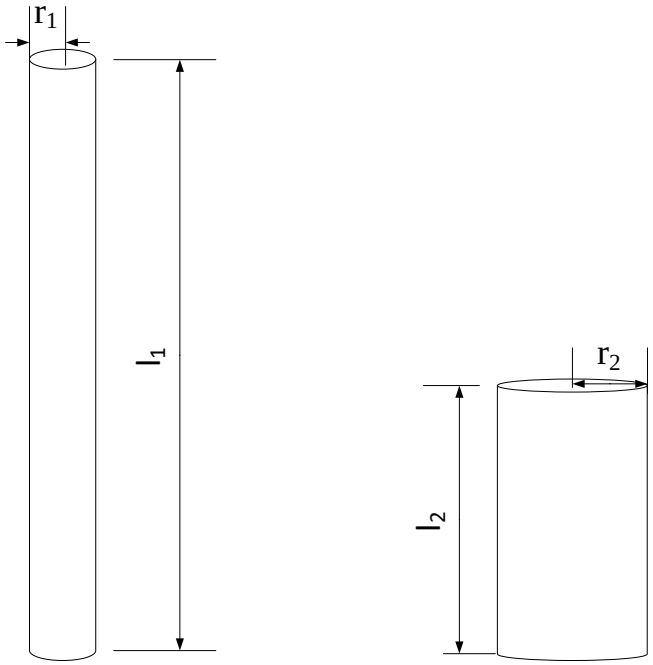

Figure 5-16. A possible explanation of why the Young's moduli of the composite at the same volume fraction with more fibres are larger than those which have less fibres.

It is obvious that given that the fibre volume fraction is the same and the fibres are all with same cross-section diameter, more random fibres means a larger total fibre length. If $\pi r_1^2 l_1 = \pi r_2^2 l_2$ and $l_1 > l_2$, than it can be referred that the surface area $4\pi r_1 l_1 > 4\pi r_2 l_2$. In the perspective of FE analysis, more fibres can get more meshed elements, thus more nodes. Then more couplings of the node pairs are created in the boundary conditions of the FE model. By increasing the fibre density, the elastic performance of 3D Voronoi fibre reinforced composite can be enhanced with same volume of reinforcement material, thus improve its weight-stiffness ratio. When the fibre volume fraction goes large, the effect of fibre density on the Young's moduli of the composite is enlarged. The Young's moduli of these composites are given in Figure 5-17. The vertical error bars represent the standard variances of the Young's moduli of 10 different random RVEs. The different of the Young's moduli of Type I is large, while that difference is very small when the point number reaches 216 and 343 (a standard

variance from 3‰ to 5‰ at 216 Voronoi points and less than 0.5‰ at 343 Voronoi points, almost fully invisible in Figure 5-17).

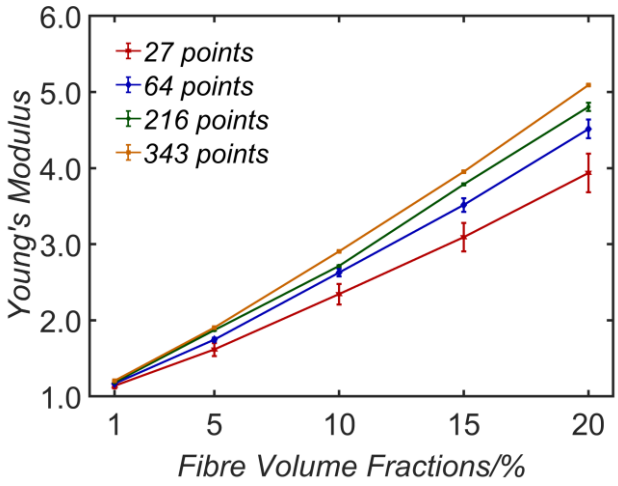

Figure 5-17. Effect of the fibre density of 3D Voronoi IPCs with same fibre volume fraction on their Young's moduli.

5.3.4 Effect of coefficient of regularity on elastic modulus

The coefficient of regularity determines the randomness of the distribution of Voronoi points. Therefore, the fibre distribution is largely affected by the coefficient of regularity. To reveal the effect of *cor* on the elastic properties of 3D Voronoi fibre reinforced composite, four different *cor*s are considered as Table 5-14 shows.

Table 5-14. coefficient of regularities of the 3D Voronoi fibre reinforced composite

cor	0.1	0.3	0.5	0.7

An illustration of 3D Voronoi fibre reinforcement build with 64 Voronoi points at different *cor*s are shown in Figure 5-18, while 3D Voronoi fibre reinforcement build with 27 and 216 Voronoi points at different *cor*s are shown in Figure 5-19 and Figure 5-20. As an RVE of 3D Voronoi fibre build with 64 Voronoi points contains around

1000 fibres, the regularity factor shows little difference regarding the microstructures of the RVEs.

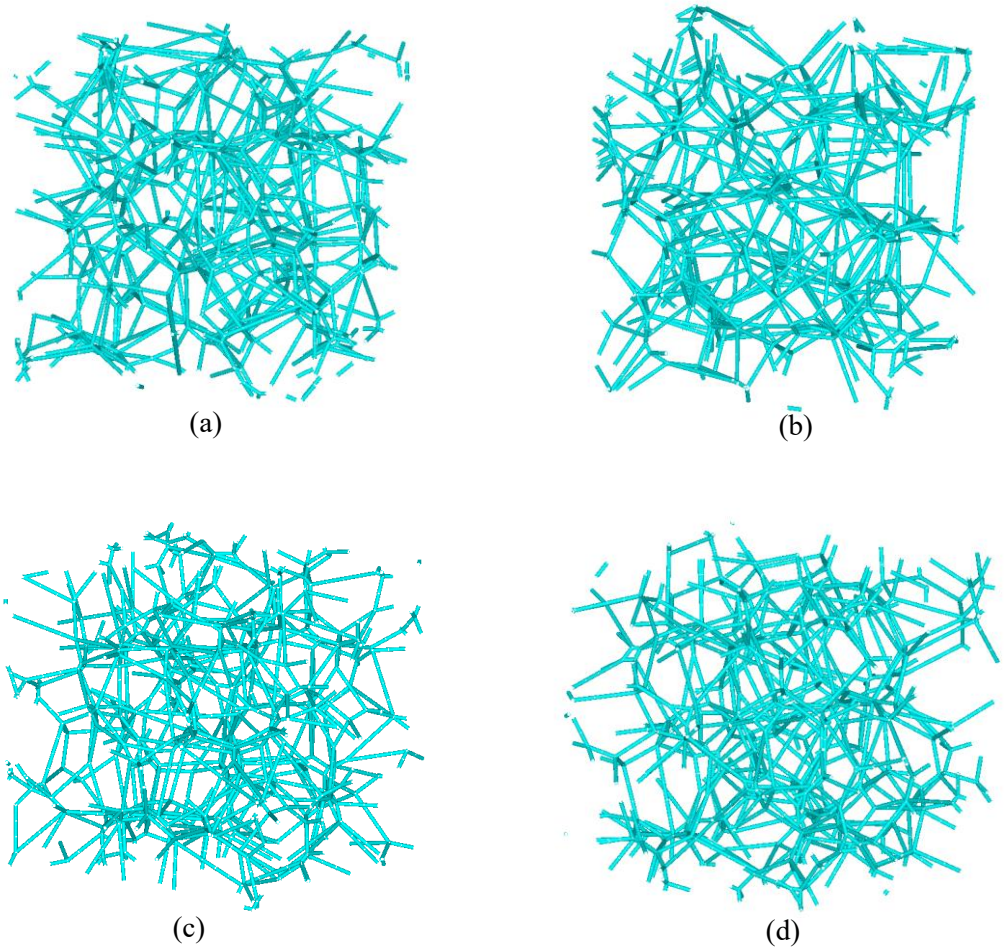

Figure 5-18. 3D Voronoi fibres network build with 64 Voronoi points at different *cor*s: (a) $cor = 0.1$; (b) $cor = 0.3$; (c) $cor = 0.5$; (d) $cor = 0.7$;

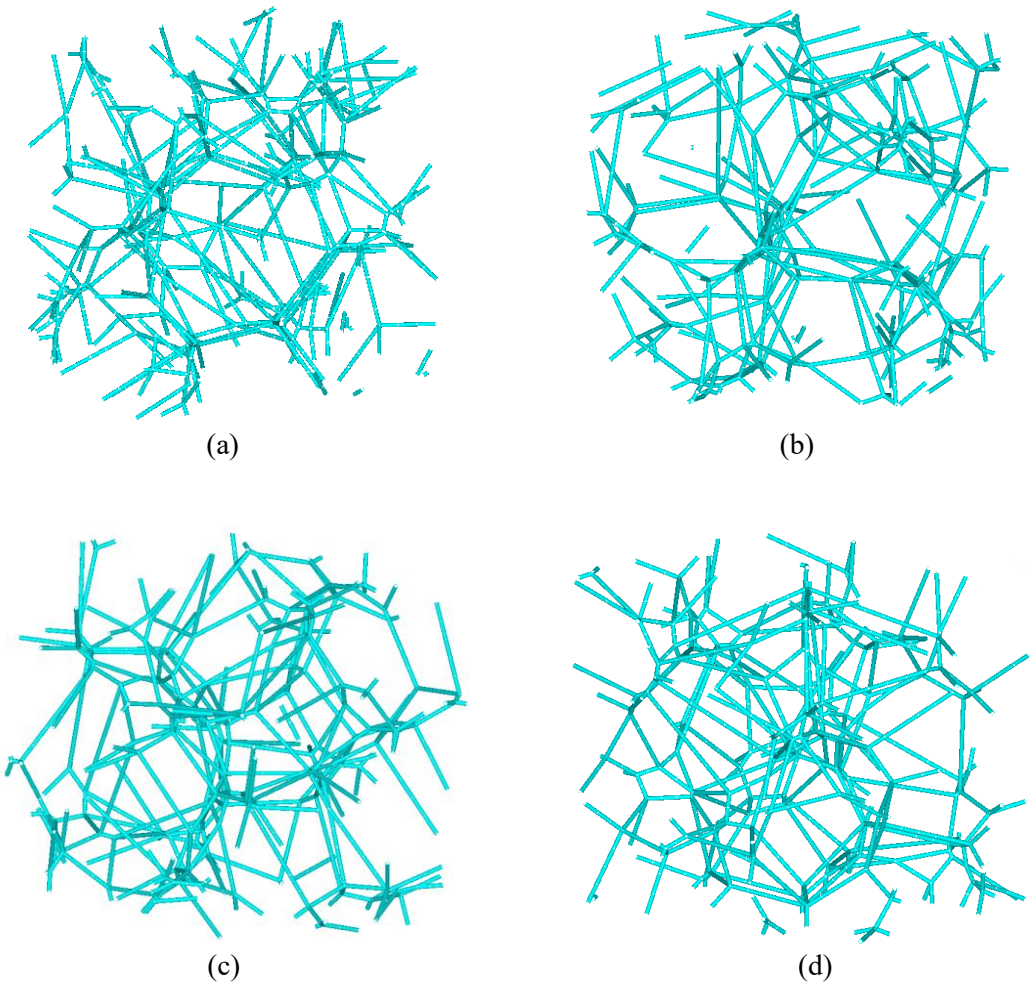

Figure 5-19. 3D Voronoi fibres network build with 27 Voronoi points at different *cor*s: (a) $cor = 0.1$; (b) $cor = 0.3$; (c) $cor = 0.5$; (d) $cor = 0.7$;

1

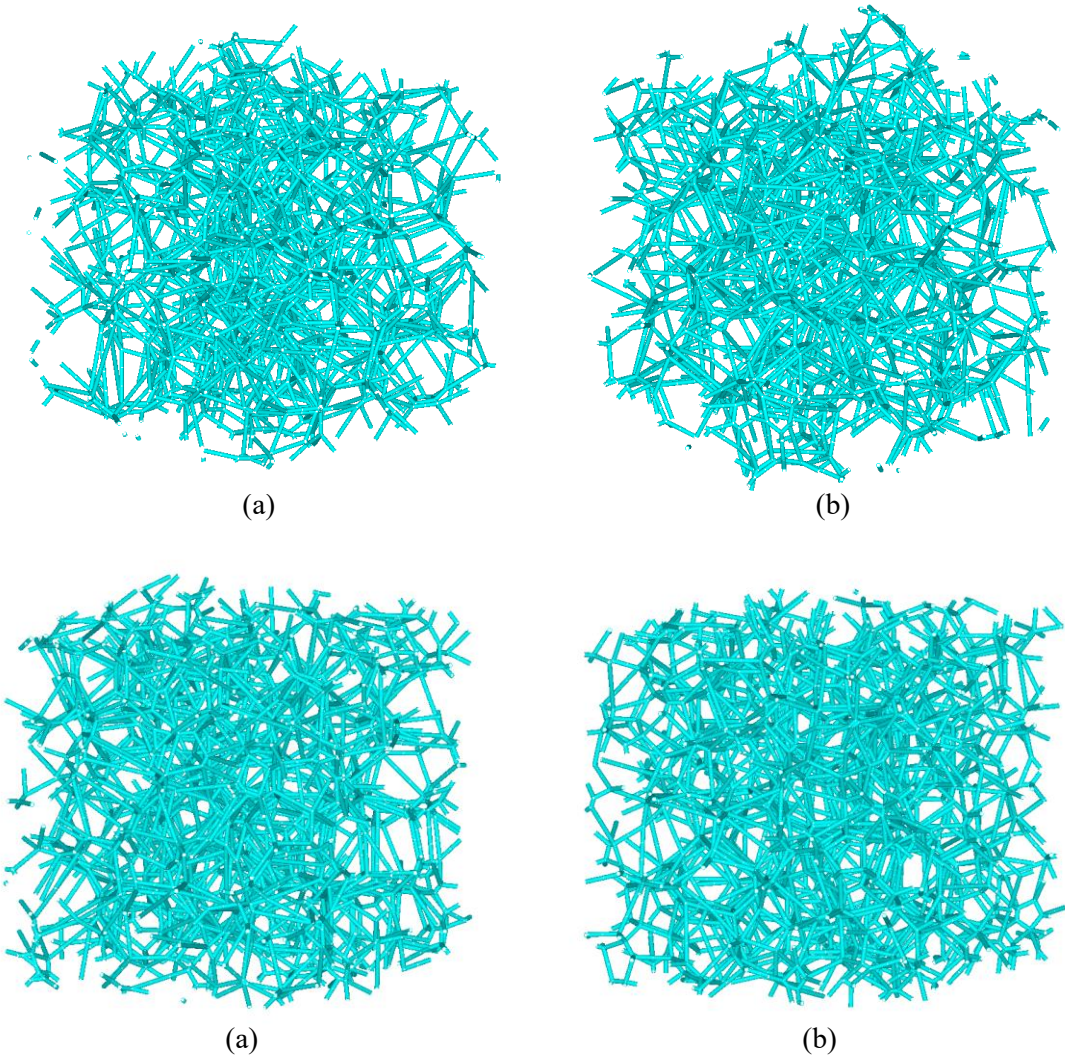

Figure 5-20. 3D Voronoi fibres network build with 343 Voronoi points at different *cor*s: (a) $cor = 0.1$; (b) $cor = 0.3$; (c) $cor = 0.5$; (d) $cor = 0.7$;

The structure different between different *cor*s is hard to observe in RVE models. To determine the effect of *cor*s to the elastic properties of the 3D Voronoi fibre reinforced composite, the Young's moduli of the composites with different *cor*s as a function of the fibre volume fractions are calculated by statistical average of 10 random models. The elastic properties of the constituent materials are $E_m = 1$, $E_f = 100$, $\nu_m = 0.3$ and $\nu_f = 0.1$. The error bars are the standard variances of the Young's moduli in x, y and z directions of the 10 models (30 Young's moduli).

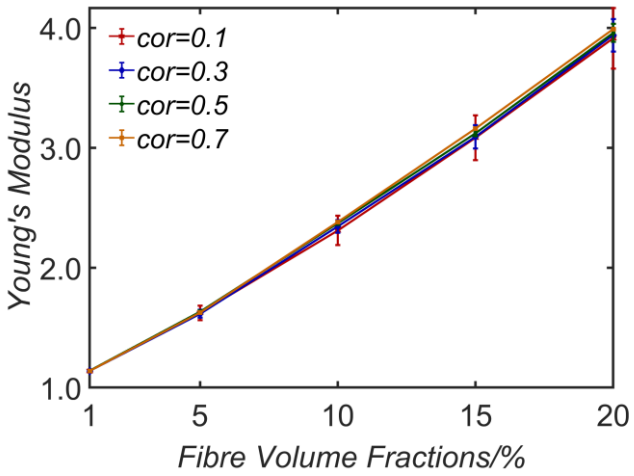

Figure 5-21. Young's moduli of the composites with different *cor*s as a function of the fibre volume fractions, RVEs are create with 27 Voronoi cells.

Figure 5-21 shows that even the number of Voronoi cells is as small as 27 ($3 \times 3 \times 3$), the Young's moduli of the composite obtained by the average of 10 random models are not with too much difference between different *cor*s. As the *cor* increases, the Young's moduli of the composite increase a very small amount in the same fibre volume fractions. The Young's moduli of the composite at $cor = 0.7$ and $f_f = 20\%$ is 1.8% larger than that at $cor = 0.1$ and $f_f = 20\%$. However, *cor*s can affect the standard variance between random models and the standard variance between x, y and z directions.

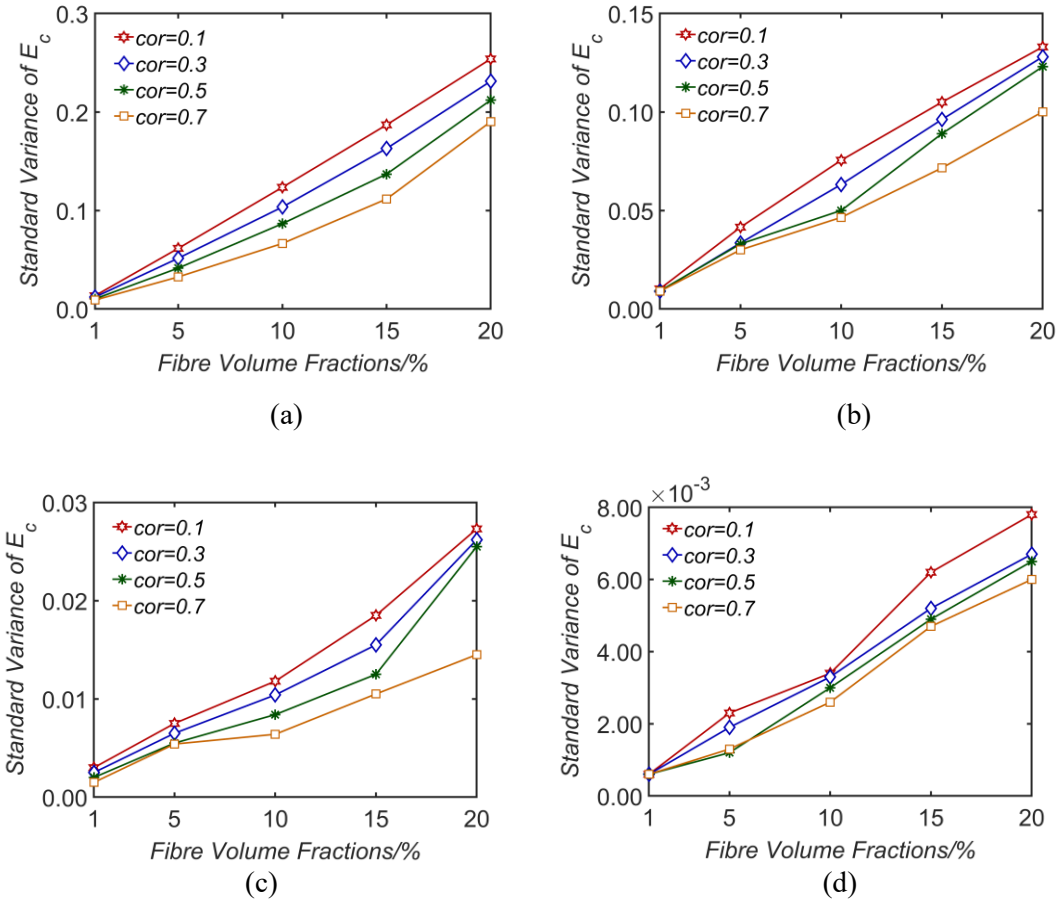

Figure 5-22. the standard variance of RVE's Young's moduli between random RVEs: (a) 27 cells (b) 64 cells (c) 216 cells (d) 343 cells.

It can be seen from each subfigure in Figure 5-22 that the standard variance of RVE's Young's moduli becomes smaller when *cor* is larger. The most important factor to determine the stability of E_c is the fibre number. As the Voronoi increases, the standard variance of E_c decreases in order of magnitude.

5.3.5. Influence of Young's moduli of the constituent materials on the Young's moduli of the composite

In order to find the influence of the elastic properties of constituent materials, their Young's moduli E_f and E_m are considered. Young's modulus of the matrix E_m is fixed as $E_m = 1$ for generality, while Young's moduli of the fibre E_f are chosen as $E_f =$

$5, 10, 50$ and 100. The combination of constituent's Poisson's ratios ν_f and ν_m is kept constant at $\nu_f = 0.1$ and $\nu_m = 0.3$. The coefficient of regularity is $cor = 0.5$ in this case. As the RVEs of 3D Voronoi fibre reinforced composite is nearly isotropic, the Young's moduli of the composite E_c is calculated by averaging the E_{cx}, E_{cy} and E_{cz}. For time consuming issue in calculation, the of Young's moduli of the composite E_c is calculated by a mean of 10 random RVEs when Voronoi cell is less than 100 and by 1 random RVE when over 100. The prediction of Young's moduli of the composite E_c as a function of the fibre volume fraction is given in Figure 5-23 (a) to (d) with different fibre densities.

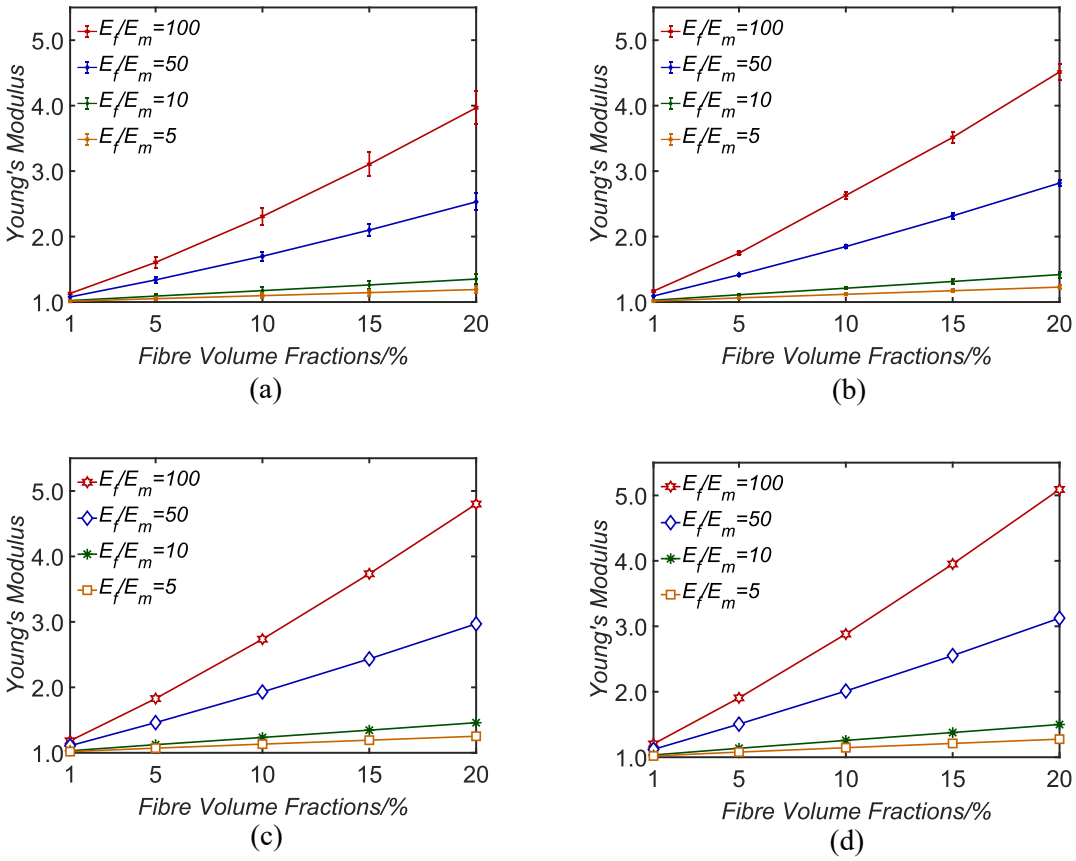

Figure 5-23. Young's moduli of the composite E_c as a function of the fibre volume fraction (a) 27 Voronoi cells. (b) 64 Voronoi cells. (c) 216 Voronoi cells. (d) 343 Voronoi cells.

Figure 5-23 shows that the Young's moduli of the composite increases with the increase of the fibre volume fraction when $E_f/E_m > 1$. The larger the volume fractions are, the

bigger differences between small and large E_f/E_m combinations will be. Moreover, the error bars in Figure 5-23 (a) and (b) shows that the standard variance of the Young' modulus E_c also goes larger when E_f/E_m is larger. The standard variances of E_c are not shown in Figure 5-23 (c) and (d) as they are too small to show in the figures and thus can be ignored. Therefore, only one random RVE is considered in each of these two subfigures. Besides, it can be observed that the Young's moduli obtained with larger fibre densities are larger than those with small fibre densities. A comparison is given in Figure 5-24 below.

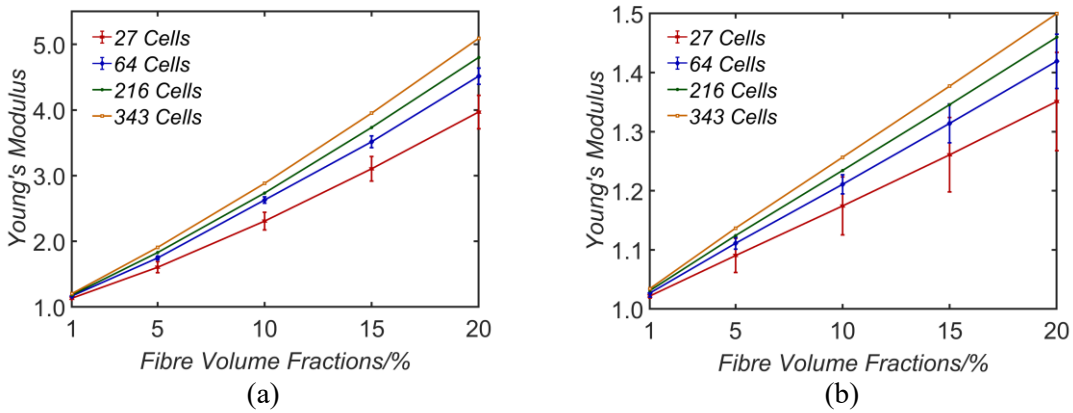

Figure 5-24. Comparison of the effect of the combination of E_f/E_m and Voronoi cell number on the relationship between E_c and VF_f; (a) $E_f/E_m = 100$. (b) $E_f/E_m = 10$

The difference between the Young's modulus of the composite E_c is as large as 20% when $E_f/E_m = 100$ and $f_f = 20\%$, as Figure 5-24 (a) shows. In Figure 5-24 (b), when $E_f/E_m = 10$, the standard variances of E_c are relatively large, indicating that a statistical approach to predict the mechanical properties of the 3D Voronoi composite with low fibre numbers and low fibre/matrix stiffness ratio is necessary. In addition, normalized Young's modulus $E_n = E_c/E_{cVoight}$ is used to determine the impact of E_f/E_m on stiffness of the composite, as Figure 5-25 shows. The standard variances of E_c is also normalized by the corresponding Voigt limit. When $E_f/E_m = 5$, the normalized Young's modulus E_n is the largest among those with different E_f/E_m values. This means that E_n get larger value when the stiffness of the fibre and the matrix

is close to each other. This is also coincident with the results in Chapter 3 and Chapter 4.

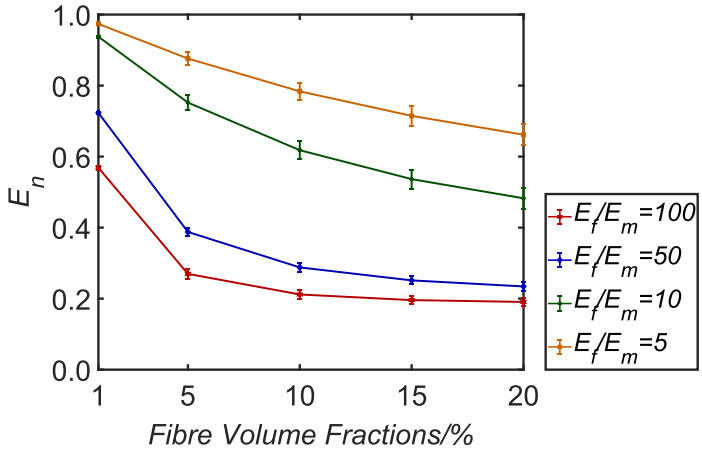

(a)

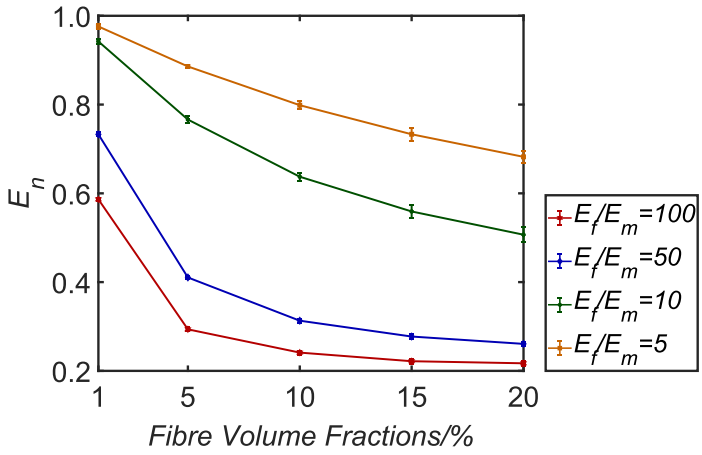

(b)

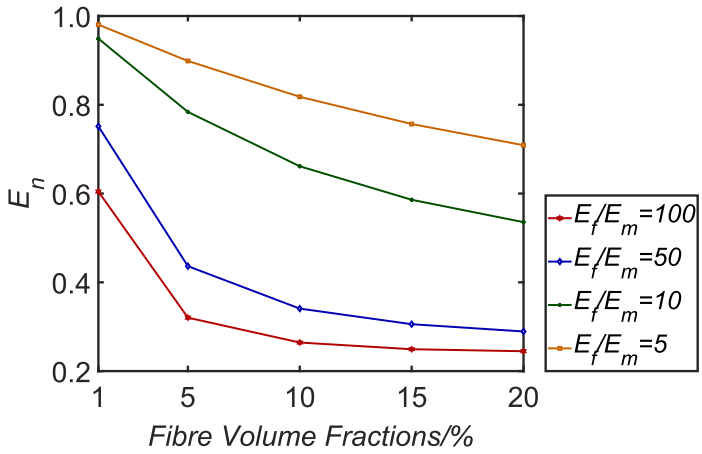

(c)

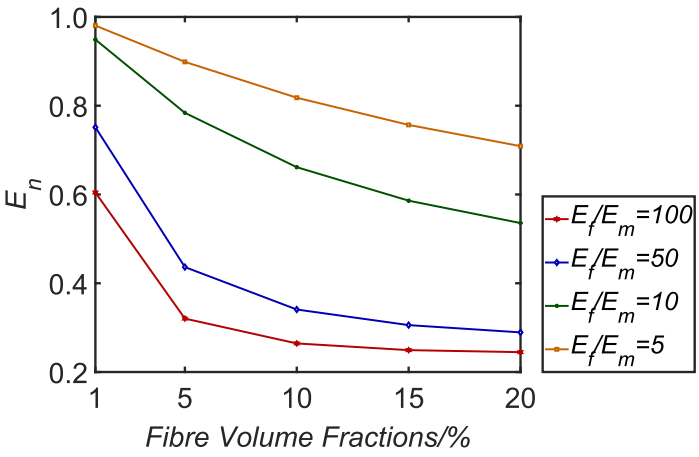

(d)

Figure 5-25. Normalized Young's moduli of the composite E_c as a function of the fibre volume fraction (a) 27 Voronoi cells. (b) 64 Voronoi cells. (c) 216 Voronoi cells. (d) 343 Voronoi cells.

5.3.6 Influence of the Poisson's ratio of constituent material's

Poisson's ratios of the constituent materials have also been proved to be one of the important factors in the prediction of the mechanical properties of the composite. To check the effect of different Poisson's ratios of the constituent materials on the elastic moduli of the composite, different combinations of ν_f and ν_m ($\nu_f = 0.1$, $\nu_m = 0.3$; $\nu_f = 0.2$, $\nu_m = 0.3$; $\nu_f = 0.05$, $\nu_m = 0.49$; $\nu_f = 0.49$, $\nu_m = 0.05$; $\nu_f = 0.06$, $\nu_m = -0.6$; $\nu_f = 0.05$, $\nu_m = -0.8$) are considered. Young's modulus of the matrix E_m is fixed as $E_m = 1$ for generality, while Young's modulus of the fibre E_f is chosen as $E_f = 100$ and $E_f = 2$. The number of Voronoi cells in one RVE is fixed at 64 and the coefficient of regularity is $cor = 0.5$ in this case.

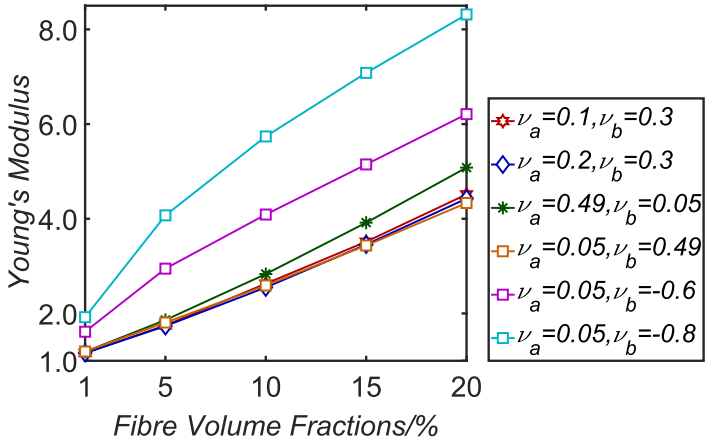

(a)

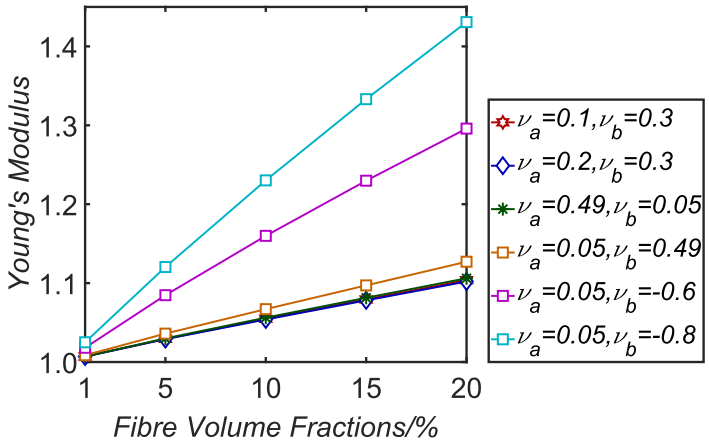

(b)

Figure 5-26. Young's moduli of the composite E_c with different constituent material Poisson's ratio combinations; (a) $E_f = 100$; (b) $E_f = 2$.

It can be seen in Figure 5-26 that the E_c obtained when $\nu_f = 0.2$, $\nu_m = 0.3$ is slightly larger the that when $\nu_f = 0.1$, $\nu_m = 0.3$. However, the different between the two is very small compared with difference between $\nu_f = 0.05$, $\nu_m = 0.49$. When the Poisson's ratio of the matrix goes to negative, the elastic moduli of the composite is significantly enhanced. Normalized Young's modulus $E_n = E_c/E_{cVoight}$ is also used to check in influence of different Poisson's ratio combinations on the Young's moduli of the composite E_c.

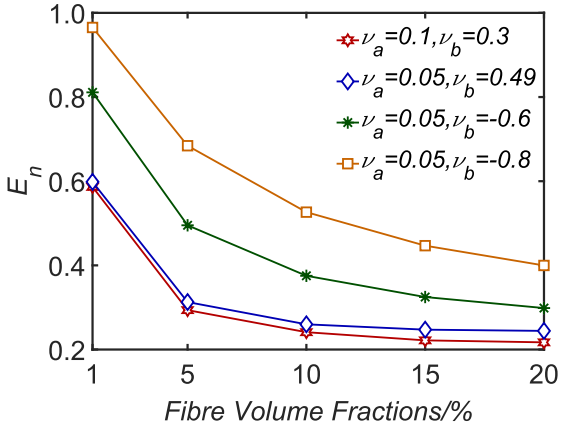

(a)

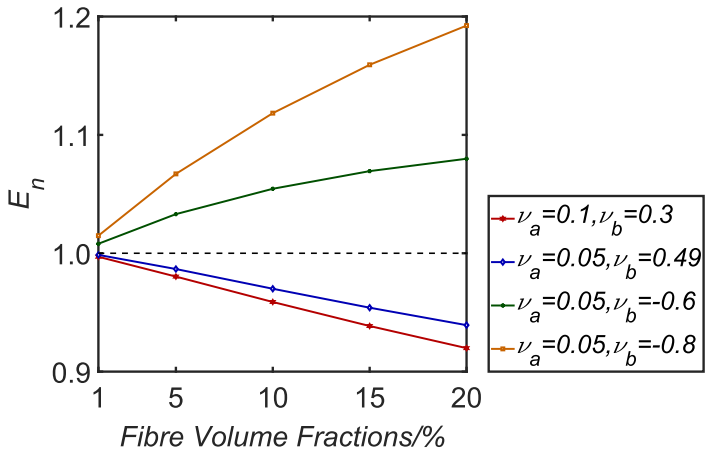

Figure 5-27. Normalized Young's moduli of the composite E_c with different constituent material Poisson's ratio combinations; (a) $E_f = 100$; (b) $E_f = 2$.

Figure 5-27 shows that when Poisson's ratio of the matrix goes to negative, the composite outperformed those with positive Poisson's ratio constituents in stiffness. The normalized Young's moduli of the composite are large than 1 when $E_f/E_m = 2$ and $\nu_m = -0.6$ or -0.8, which means the Young's modulus of the 3D Voronoi fibre reinforced composite can reach and surpass the Voigt limit under proper combination of mechanical properties of the constituent materials.

5.4 Discussion

In order to validate the simulation results and to show the advantage of the 3D Voronoi fibre reinforced composite in terms of elastic properties, we compared the Young's moduli obtained in this Chapter to those obtained from different types of particle and fibre reinforced composites, both experimentally and numerically.

For the random particle and short fibre reinforced composites [198], aspect ratios $\xi = 1$ (which means sphere particle reinforcement) and $\xi = 5$ (which means short fibres reinforcement), is selected. The reinforcement volume fraction is $f_r = 0.2$. Other parameters are $E_r = 70$ GPa, $\nu_r = 0.2$ and $E_m = 3$ GPa, $\nu_r = 0.35$ for the reinforcements and fibres, respectively. The geometry of this work is shown in Figure 5-28 (a) and (b). Completely random oriented fibre reinforcement which can construct an isotropic composite is also considered in the 4th case of Babu *et al.*'s work [200]. The constituent materials considered in that study was AS4 carbon fibre and 3501-6 Epoxy matrix. The elastic properties of the constituent materials are $E_{r1} = 225$GPa, $E_{r2} = 15$GPa, $\nu_r = 0.2$ and $E_m = 4.2$GPa, $\nu_r = 0.35$. The volume fractions were $f_r = 15.23\%$, 19.23% and 21.64% for RVE generation in Babu *et al.*'s work. The geometry of this work is shown in Figure 5-28 (c).

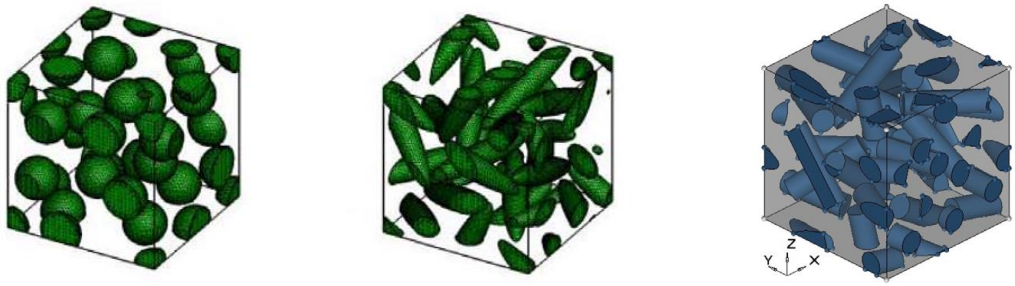

(a) (b) (c)

Figure 5-28. The RVE geometric models of isotropic discrete fibre reinforced composite: (a) Ref [198], $\xi = 1$. (b) Ref [198], $\xi = 5$. (c) Ref [200], Case 4.

The same parameters are applied to the 3D Voronoi network reinforced model, coefficient of regularity $cor = 0.5$, number of Voronoi cell $n = 64$. The comparisons

in terms of Young's moduli of the composite with those in reference [198] are presented in Table 5-15 and the comparisons with reference [200] are presented in Figure 5-29.

Table 5-15. Young's moduli of the composite in reference [198] and 3D Voronoi fibre reinforced composite.

Composite	$VF_r = 0.2$	E_c
Reference [198], $\xi = 1$	0.2	6.6233
Reference [198], $\xi = 5$	0.2	6.7700
3D Voronoi composite	0.2	7.8970

From Table 5-15 we can infer that the Young's moduli E_c is 16.7% larger than that of the random short fibre reinforced fibre composite in reference [198] when aspect ratio $\xi = 5$. Besides, the Young's moduli E_c is far larger than those predicted in reference [200] with same volume fractions as Figure 5-29 shows.

Furthermore, it is necessary to compare different lattice structure reinforced composites in this thesis to determine which one have the best elastic performance under different constituent materials.

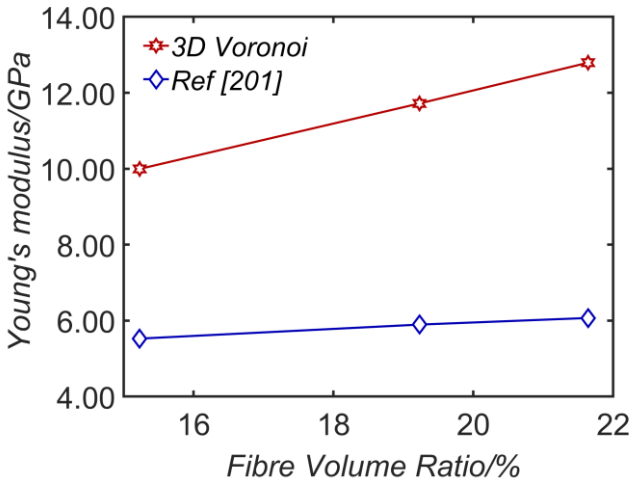

Figure 5-29. Young's moduli of the composite in reference [200], case 4 and 3D Voronoi fibre reinforced composite.

To compare the Young's moduli of the composites, the regular lattice structured IPCs type I and type III discussed in Chapter 3, auxetic lattice structured IPCs type II and type III discussed in Chapter 4 with fibre concavity angle $\alpha = 18°$ and the 3D Voronoi composite created with coefficient of regularity $cor = 0.5$ and Voronoi cell number $n = 64$ in this Chapter are listed for comparison below in Figure 5-30.

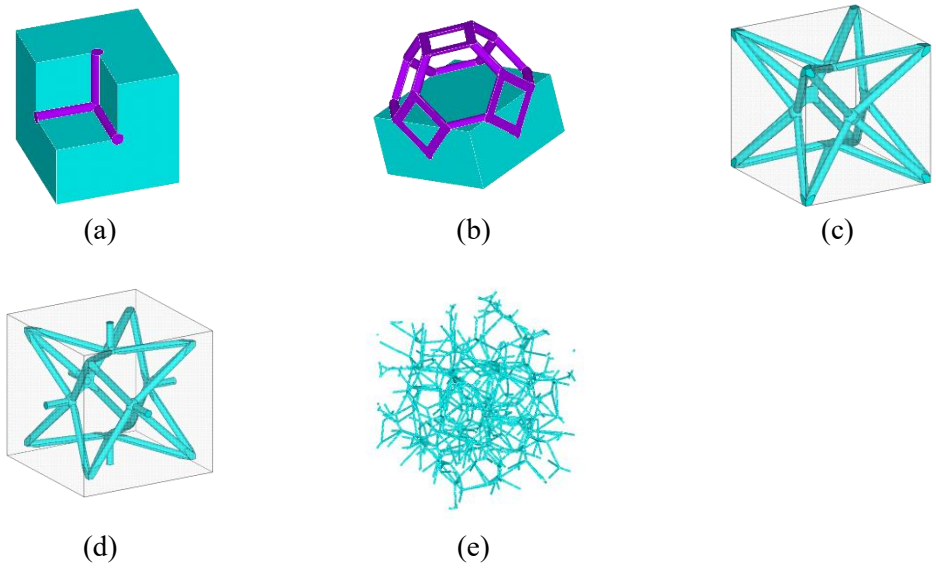

Figure 5-30. RVEs of lattice structure reinforced interpenetrating composites listed for comparison. (a) regular lattice reinforced IPC type I; (b) regular lattice reinforced IPC type III; (c) auxetic lattice reinforced IPC type II; (d) auxetic lattice reinforced IPC type III; (e) 3D Voronoi fibre network reinforced IPC type II (matrix not shown).

Four sets of parameters for the constituent materials as listed in Table 5-16: the first two sets represent strong fibre and polymer matrix combination such as carbon/epoxy or aluminium/epoxy; the last two sets represent metal-metal or polymer-polymer composites which the fibres and the matrix have closer mechanical properties.

Table 5-16. Three sets of constituent material parameters.

	E_f	E_m	ν_f	ν_m
Set 1	100	1	0.1	0.3
Set 2	100	1	0.1	-0.5
Set 3	5	1	0.1	0.3
Set 4	5	1	0.1	-0.5

The Young's moduli of different types of IPCs are plotted in Figure 5-31.

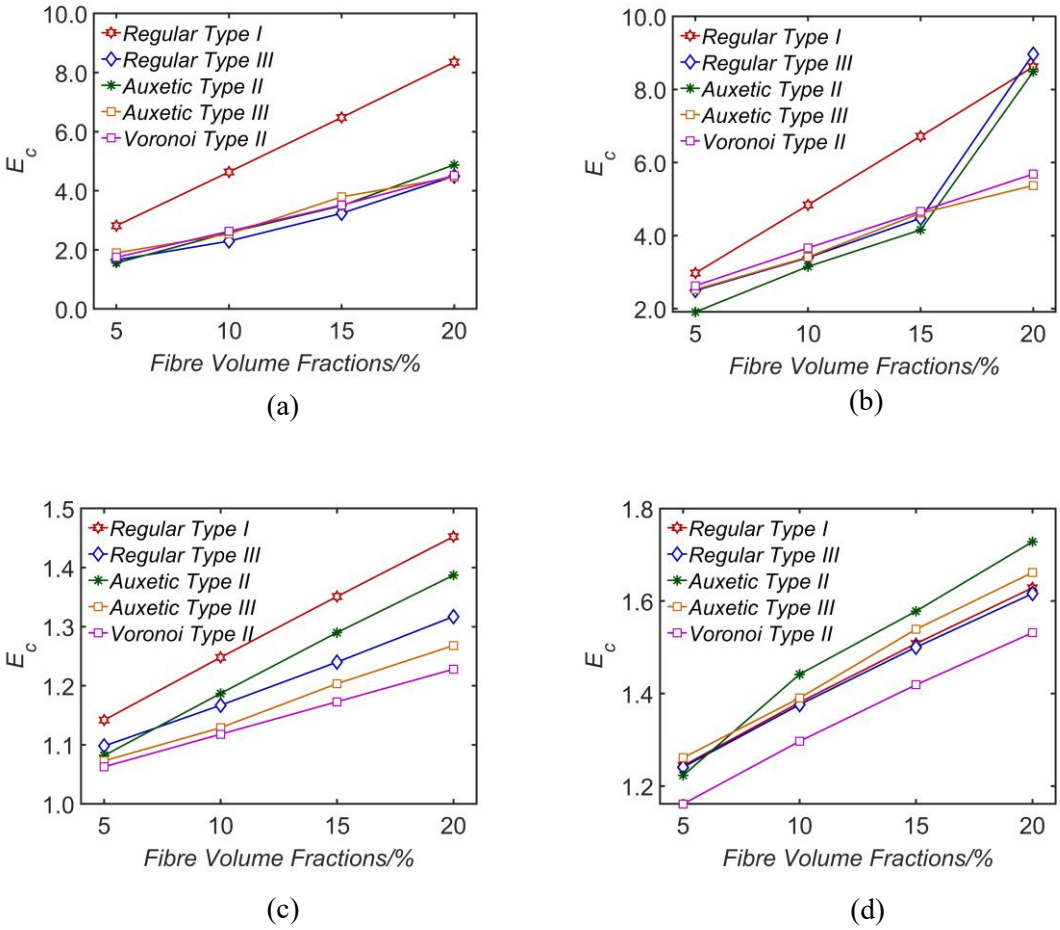

Figure 5-31. The Young's moduli of different types of IPCs constructed with same constituent materials. (a) $E_f/E_m = 100$, $\nu_f = 0.1$, $\nu_m = 0.3$ (b) $E_f/E_m = 100$, $\nu_f = 0.1$, $\nu_m = -0.5$ (c) $E_f/E_m = 5$, $\nu_f = 0.1$, $\nu_m = 0.3$ (d) $E_f/E_m = 5$, $\nu_f = 0.1$, $\nu_m = -0.5$.

An overview of Figure 5-31 (a), (b) and (c) shows that the best structure in terms of stiffness is apparently the type I of regular cubic lattice reinforced composites when ν_f and ν_m is positive. When ν_m is negative, the stiffness of regular lattice reinforced composite type I is the largest among those of different IPC structures at 5%, 10% and 15% fibre volume fractions. However, the stiffness regular lattice reinforced composite type III and that of auxetic IPC type II come close to the stiffness of regular IPC type I at 20% volume fractions. The only condition to consider other type of IPCs to be the best is when $E_f/E_m = 5$, $\nu_f = 0.1$, $\nu_m = -0.5$. Interestingly, the auxetic interpenetrating composite type II and regular lattice reinforced IPC type III show the similar stiffness behaviour, while the stiffness as a function of the fibre volume fraction

of auxetic interpenetrating composite type III and that of the 3D Voronoi fibre network reinforced composite type II ($cor = 0.5$, $n = 64$) are similar. This can be found in all the subfigures of Figure 5-31, especially in (b) and (d).

The normalized Young's moduli E_n is also considered in this comparison as Figure 5-32 shows.

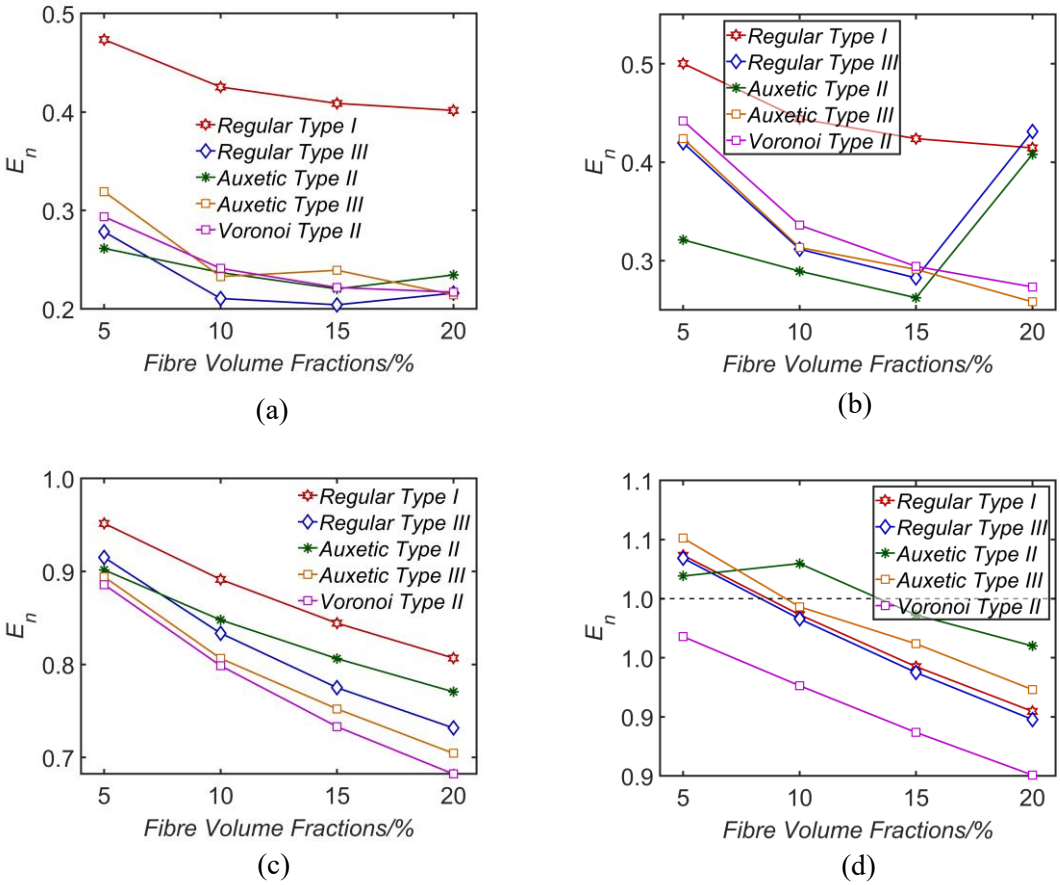

Figure 5-32. Normalized Young's moduli of different types of IPCs constructed with same constituent materials. (a) $E_f/E_m = 100$, $\nu_f = 0.1$, $\nu_m = 0.3$ (b) $E_f/E_m = 100$, $\nu_f = 0.1$, $\nu_m = -0.5$ (c) $E_f/E_m = 5$, $\nu_f = 0.1$, $\nu_m = 0.3$ (d) $E_f/E_m = 5$, $\nu_f = 0.1$, $\nu_m = -0.5$

The results of E_n are the same in terms of structure rankings with the results of E_c. However, it can be seen that the normalized Young's moduli of different types of the composites are under 1.0 except the restrict condition when $f_f = 5\%$, $E_f/E_m = 5$, $\nu_f = 0.1$ and $\nu_m = -0.5$.

5.5 Conclusion

In this chapter, the 3D Voronoi fibre network is generated via Voronoi tessellation and is used as the reinforcement of the composite. Compared to regular lattice structures studied in Chapter 3 and Chapter 4, the 3D Voronoi network could give a better description of some fabricated interpenetrating composites. The periodicity of the random fibre network is ensured by filling multiple tessellation space with groups of Voronoi points. and then divided them into fully periodic RVEs. Furthermore, the coefficient of regularity *cor* and fibre numbers contained in an RVEs *n* is defined when constructing the Voronoi fibre network. In order to reduce pre-processing and solving time of the composite models, beam element instead of solid elements used in Chapter 3 and Chapter 4 is applied to the fibres. Afterwards, an automatic searching & coupling (ASC) technique is introduced to coupling the nodes of the nodes of fibres and matrix as Boolean operation cannot be done between line (beam fibre) and volumes (matrix). The periodic boundary conditions stated in Chapter 3 is modifies to adapt the ASC technique to avoid the over constraints which would occur when applying PBCs at both beam fibres and matrix. The total fibre length is confirmed to be different between every random RVEs even the Voronoi cell number is the same. Thus, the fibre volume fractions as a function of total fibre length corresponding to individual RVE and fibre diameter is given.

The mesh sensitivity of fibre and matrix is discussed. A reasonable element size ratio of es_f/es_m is determined. Moreover, the best es_f is found by comparing the ASC RVEs to full solid RVEs. The impact of random fibre distribution, number of fibres in an RVE and the coefficient of regularity is discussed. It is found the when the number of fibres in an RVE is large, which means more Voronoi cells in an RVE, the effect of coefficient of regularity on the Young's moduli of the composite E_c is reduced. However, when there are less fibres in an RVE, the random fibre distribution and coefficient of regularity make a relatively big different on the mechanical properties of the composite.

The 3D Voronoi fibre reinforced composite is nearly isotropic. The stiffness of the composite shows a linear relation with the fibre volume fraction. The Young's modulus of the composite E_c increase as E_f and E_{m} increase. However, the study of the normalized Young's moduli E_n indicates that E_n increases when E_f/E_{m} approaches 1 and $|\nu_f - \nu_m|$ get the largest possible value. However, as the volume fraction is limited up to 20%, no peak of E_n is found in the range of 1% to 20% fibre volume fraction and E_n increases with the increase of fibre volume fraction.

The comparison of existing journal results of random fibre reinforced composites shows that the 3D Voronoi composite performs better than the discrete particle and short fibre reinforced composites in terms of elastic moduli. To determine the best structure in different given conditions, the structures investigated in Chapter 3, 4 and 5 is compared in terms of the stiffness. It is found that regular lattice structure type I is the most effective structure in build high stiffness composites in small fibre volume fractions. The auxetic IPC type II and regular lattice reinforced IPC type III shows the similar elastic behaviour as the fibre volume fraction changes, while the stiffness as a function of the fibre volume fraction of auxetic interpenetrating composite type III and that of the 3D Voronoi fibre network reinforced composite type II ($cor = 0.5, n = 64$) are similar.

Chapter 6 Conclusions and further work

6.1 Conclusions

This thesis numerically predicts the elastic properties of different types of quasi-isotropic fibre network reinforced interpenetrating composites. Representative volume elements and periodic boundary conditions are customized and applied.

For regular lattice structured interpenetrating composites, four different types of IPC structures are considered. It is found that the Young's modulus of the composite rises as a function of the reinforcement volume fraction. At the same time, the Young's modulus of the composite E_c also becomes larger when E_f and E_{m} goes larger. However, the study of the normalized Young's moduli E_n indicates that E_c is larger when E_f/E_{m} approaches 1 $|\nu_f - \nu_m|$ get the largest possible value. The largest normalized Young's modulus can be obtained in a fibre volume fraction around 30% to 40%. The elastic properties of the composites have strong relationship with the Poisson's ration of the two constituent materials. The Young's modulus of different types of composites can be much larger than the HS upper limit and can drastically exceed the Voigt limit when the Poisson's ratio of the matrix is negative and the Young's moduli of the two phases are close enough. This are coincident with the analytical results by Zhu, Fan and Zhang [74] in 2015. By comparing the normalized Young's moduli E_n, we can see that the tetrakaidekahedron structure (Type III) performs well with negative Poisson's ratio matrix. On the contrary, the simplest cross-cubic model performs the best with positive Poisson's ration matrix. These kind of latticed interpenetrating composites are better than its conventional counterparts like particle and unidirectional fibre reinforced composites.

As negative Poisson's ratio matrices are considered in regular lattice structured IPCs, the possibility to tune the Poisson's ratio of the composite to negative, or zero is studied. To solve the congenital disadvantages such as weak stiffness of porous auxetic

materials, solid interpenetrating composites reinforced by three different types of fibre-networks are studied. They all could have a positive, negative, or 'zero' Poisson's ratio. The magnitude of the Poisson's ratio depends on the combination between the fibre angle α, the type of the fibre-network, the fibre volume fraction, and the mechanical properties of the component materials: E_f/E_m, ν_f and ν_m. A smaller fibre angle α leads to lager auxetic behaviour in Type I and Type II composites with no face-links in their structure, while the absolute value of the negative Poisson's ratio is large with a relatively larger fibre angle α under its structural limit. The largest the absolute value of negative Poisson's ratio is around -0.3 for an auxetic interpenetrating composite with common constituent materials. In addition, as all the three types of composites have cubic symmetry, their mechanical properties are almost isotropic. Moreover, structural hierarchy can significantly enhance the auxetic behaviour of the composites. Therefore, the three different types of auxetic interpenetrating composites could be used not only as functional materials, but also as structural materials in engineering applications. As the composites do not contain any pore in structure and the strengthening phase is a self-connected network, the Young's moduli of the three types of composites are obviously larger than those of the conventional particle composites. This result provides an alternative to manufacture non-porous negative and zero Poisson's ratio materials, which have many applications as functional materials and biomaterials.

Furthermore, to simulate natural and fabricated random fibre networks and their composites, 3D Voronoi fibre network reinforced composite is investigated. Periodic 3D Voronoi fibre network is generated from random points by both random search and QuickHull Voronoi tessellation and embedding to solid matrix in FE model. It is tested that ASC coupling with beam element fibres and solid element matrix is valid in predicting the mechanical property of the Voronoi fibre composite. It is found that the fibre number and coefficient of regularity can both affect the isotropy of the composite. Larger fibre number *n* and coefficient of regularity *cor* can result in a more isotropic structure. The effect of the Young's modulus and Poisson's ratio of the constituent materials on the mechanical properties of the 3D Voronoi fibre reinforced composite is

similar as that of the regular lattice structure. A linear relationship between the Young's modulus of the composite and the fibre volume fraction is found and the Young's modulus of the composite can also surpass the Voigt limit under negative Poisson's ratio matrix. The relationship between normalized stiffness of the composite and the elastic properties of the constituent materials also shares the same trend with the regular latticed structures.

6.2 Future work

This thesis investigated the elastic properties of different types of fibre network reinforced composites including regular lattice structured ones, negative Poisson's ratio ones and 3D Voronoi ones. They are compared and discussed to answer the 'which is the best' question under different conditions. As the work of this thesis are mostly done by simulation, convincible validation methods are worth investigating. For example, the build the structures discussed in this thesis by 3D printing and then validate the results by tensile test would be a good choice.

Apart from validation work, there are also three directions for the future work.

The first perspective is from the mechanical and physical properties of the composite. Only elastic properties are considered in this thesis. The elastoplastic and viscoelastic properties of the cellular fibre network reinforced composite could be considered under the same RVE models and boundary conditions. Besides, the thermal and electrical conductivity of the composite is worth to be examined as cellular fibre network reinforced composite is also good candidate in thermal and electrical industries. Furthermore, the fracture toughness would also be a very important research direction.

The second direction is the architectures and microstructures of the composite. Only 6 regular structures and 1 randomly created structure are considered in this thesis. However, a lot of different structures are promising in various applications. Future work could be done to determine what kind of cellular fibre structure is best under given conditions and targets. For example, which lattice structure has the best stiffness if 3D

printed by VeroWhite and TangoPlus under 10% of VeroWhite? It is possible for some of these questions to be converted as an optimization problem with constraints. Traditional mechanics as well as modern machine learn methods maybe alternative approaches to these problems.

The third direction is the interfaces between the fibres and matrix of these models. The corresponding nodes in the same positions of the interfaces are coupled in solid-solid fibre and matrix models, while a few of those nodes coupled in beam-solid fibre and matrix models are not in the same position. Although the accuracy of these two methods are both good, it is obvious that they represent slightly different interfaces. Furthermore, the accuracy of full coupled interfaces varies when representing different type of material combinations. Coating and other treatment of the fibre may affect the interfaces as well.

References

[1] D.R. Clarke, Interpenetrating Phase Composites, J. Am. Ceram. Soc. 75 (1992) 739–758. doi:10.1111/j.1151-2916.1992.tb04138.x.

[2] R.M. Jones, Mechanics Of Composite Materials, Taylor & Francis, 1998. https://books.google.co.uk/books?id=oMph2kNG3yAC.

[3] T. Kjeilen, Sumer - LookLex Encyclopaedia, (2019). http://i-cias.com/e.o/sumer.htm#culture.

[4] J.E. Gordon, The new science of strong materials: or why you don't fall through the floor, Expanded E, Princeton University Press, Princeton, 2006.

[5] C.T. Herakovich, Mechanics of composites: A historical review, Mech. Res. Commun. 41 (2012) 1–20. doi:10.1016/j.mechrescom.2012.01.006.

[6] A. Moropoulou, A. Bakolas, S. Anagnostopoulou, Composite materials in ancient structures, Cem. Concr. Compos. 27 (2005) 295–300. doi:10.1016/j.cemconcomp.2004.02.018.

[7] L.H. Baekeland, The synthesis, constitution, and uses of bakelite, Ind. Eng. Chem. 1 (1909) 149–161. doi:10.1021/ie50003a004.

[8] S. McBeath, Competition car composites: a practical handbook, Haynes Publishing, 2000.

[9] D.F. Adams, Engineering composite materials, Composites. 18 (1987) 261. doi:10.1016/0010-4361(87)90420-4.

[10] J.P. Kruth, M.C. Leu, T. Nakagawa, Progress in additive manufacturing and rapid prototyping, CIRP Ann. - Manuf. Technol. 47 (1998) 525–540. doi:10.1016/S0007-8506(07)63240-5.

[11] T.T. Wohlers, Rapid Prototyping & Tooling: state of the industry: annual worldwide progress report, Wohlers Associates, 1997.

[12] B. Kieback, A. Neubrand, H. Riedel, Processing techniques for functionally graded materials, Mater. Sci. Eng. A. 362 (2003) 81–106. doi:10.1016/S0921-5093(03)00578-1.

[13] M.Y. Zhou, J.T. Xi, J.Q. Yan, Modeling and processing of functionally graded materials for rapid prototyping, J. Mater. Process. Technol. 146 (2004) 396–402. doi:10.1016/j.jmatprotec.2003.11.034.

[14] J. Huang, G.M. Fadel, V.Y. Blouin, M. Grujicic, Bi-objective optimization design of functionally gradient materials, Mater. Des. 23 (2002) 657–666. doi:10.1016/S0261-3069(02)00048-1.

[15] N. Chawla, K.K. Chawla, Metal Matrix Composites, Springer, 2006. https://books.google.co.uk/books?id=gU1tagimjIcC.

[16] Z. Hashin, S. Shtrikman, A Variational approach to the theory of the effective magnetic permeability of multiphase materials, J. Appl. Phys. 33 (1962) 3125–3131. doi:10.1063/1.1728579.

[17] T. Mori, K. Tanaka, Average stress in matrix and average elastic energy of materials with misfitting inclusions, Acta Metall. 21 (1973) 571–574.

[18] Z. Hashin, S. Shtrikman, A variational approach to the theory of the elastic behaviour of multiphase materials, J. Mech. Phys. Solids. 11 (1963).

[19] A. Reuss, Calculation of the flow limit of mixed crystals on the basis of the plasticity

condition for single crystals., ZAMM-Journal Appl. Math. Mech. 9 (1929) 49–58.

[20] Y. Benveniste, A new approach to the application of Mori-Tanaka's theory in composite materials, Mech. Mater. 6 (1987) 147–157.

[21] C. Singhal, Q. Murtaza, Parvej, Microwave Sintering of Advanced Composites Materials: A Review, Mater. Today Proc. 5 (2018) 24287–24298. doi:10.1016/j.matpr.2018.10.224.

[22] Z. Quan, A. Wu, M. Keefe, X. Qin, J. Yu, J. Suhr, J.H. Byun, B.S. Kim, T.W. Chou, Additive manufacturing of multi-directional preforms for composites: Opportunities and challenges, Mater. Today. 18 (2015) 503–512. doi:10.1016/j.mattod.2015.05.001.

[23] S. Ramakrishna, J. Mayer, E. Wintermantel, Kam. W. Leong, Biomedical applications of polymer-composite materilas: a review, Composites Science and Technology. 61 (2003) 861–865. doi:10.1109/isemc.2002.1032709.

[24] S. Stankovich, D.A. Dikin, G.H.B. Dommett, K.M. Kohlhaas, E.J. Zimney, E.A. Stach, R.D. Piner, S.B.T. Nguyen, R.S. Ruoff, Graphene-based composite materials, Nature. 442 (2006) 282–286. doi:10.1038/nature04969.

[25] E. Lau, C. Zhu, R.T. Abraham, W. Jiang, A critical review on nanotube and nanotube/nanoclay related polymer composite materials, Compos. Part B. 7 (2006) 425–436.

[26] T. Zeuner, P. Stojanov, P.R. Sahm, H. Ruppert, A. Engels, Developing trends in disc brake technology for rail application, Mater. Sci. Technol. 14 (1998) 857–863. doi:10.1179/mst.1998.14.9-10.857.

[27] J. Ding, C. Cui, Y. Sun, J. Ding, L. Zhao, S. Cui, Microstructures and mechanical properties of in-situ CaB6 ceramic particles reinforced Al-Cu-Mn composite, Ceram. Int. (2019) 1–8. doi:10.1016/j.ceramint.2019.07.165.

[28] M.K. Akbari, H.R. Baharvandi, O. Mirzaee, Investigation of particle size and reinforcement content on mechanical properties and fracture behavior of A356-Al2O3 composite fabricated by vortex method, J. Compos. Mater. 48 (2014) 3315–3330. doi:10.1177/0021998313507618.

[29] D.J. Lloyd, Particle reinforced aluminium and magnesium matrix composites, Int. Mater. Rev. 39 (1994) 1–23. doi:10.1179/imr.1994.39.1.1.

[30] C.H. Chen, C.H. Cheng, Effective elastic moduli of misoriented short-fiber composites, Int. J. Solids Struct. 33 (1996) 2519–2539. doi:10.1016/0020-7683(95)00160-3.

[31] H. Frohlich, R. Sack, Theory of the rheological properties of dispersions., Proc. R. Soc. Lond. A. Math. Phys. Sci. 185 (1946) 415–430.

[32] P.R. Marur, Estimation of effective elastic properties and interface stress concentrations in particulate composites by unit cell methods, Acta Mater. 52 (2004) 1263–1270. doi:10.1016/j.actamat.2003.11.010.

[33] J.D. Eshelby, The determination of the elastic field of an ellipsoidal inclusion, and related problems, Math. Phys. Eng. Sci. 241 (1957). doi:10.1017/S0305004100053366.

[34] T. Mura, Micromechanics of Defects in Solids, Springer Netherlands, 1987.

[35] N. Chawla, R.S. Sidhu, V. V. Ganesh, Three-dimensional visualization and microstructure-based modeling of deformation in particle-reinforced composites, Acta Mater. 54 (2006) 1541–1548. doi:10.1016/j.actamat.2005.11.027.

[36] J. Segurado, J. Llorca, A numerical approximation to the elastic properties of sphere-reinforced composites, J. Mech. Phys. Solids. 50 (2002) 2107–2121. doi:10.1016/S0022-5096(02)00021-2.

[37] H.J. Böhm, A. Eckschlager, W. Han, Multi-inclusion unit cell models for metal matrix composites with randomly oriented discontinuous reinforcements, Comput. Mater. Sci. 25 (2002) 42–53. doi:10.1016/S0927-0256(02)00248-3.

[38] S. Kari, H. Berger, R. Rodriguez-Ramos, U. Gabbert, Computational evaluation of effective material properties of composites reinforced by randomly distributed spherical particles, Compos. Struct. 77 (2007) 223–231. doi:10.1016/j.compstruct.2005.07.003.

[39] Y. Hua, L. Gu, Prediction of the thermomechanical behavior of particle-reinforced metal matrix composites, Compos. Part B Eng. 45 (2013) 1464–1470. doi:10.1016/j.compositesb.2012.09.056.

[40] S.C. Tjong, Novel nanoparticle-reinforced metal matrix composites with enhanced mechanical properties, Adv. Eng. Mater. 9 (2007) 639–652. doi:10.1002/adem.200700106.

[41] Z. Sadeghian, B. Lotfi, M.H. Enayati, P. Beiss, Microstructural and mechanical evaluation of Al-TiB2 nanostructured composite fabricated by mechanical alloying, J. Alloys Compd. 509 (2011) 7758–7763. doi:10.1016/j.jallcom.2011.04.145.

[42] S. Bathula, M. Saravanan, A. Dhar, Nanoindentation and Wear Characteristics of Al 5083/SiCp Nanocomposites Synthesized by High Energy Ball Milling and Spark Plasma Sintering, J. Mater. Sci. Technol. 28 (2012) 969–975. doi:10.1016/S1005-0302(12)60160-1.

[43] H. Hammesfahe, Glass Cloth or Fabric, US patent US232122A, 1880.

[44] A. Kelly, W.R. Tyson, Tensile Fibre-Reinforced Metals : Copper/Tungsten and Copper/Molybsenum, J. Mech. Phys. Solids. 13 (1965) 329–350.

[45] W.G. Glasser, Viscoelasticity of biomaterials, American Chemical Society, United States, 1992. http://inis.iaea.org/search/search.aspx?orig_q=RN:24063180.

[46] V.G. Geethamma, R. Joseph, S. Thomas, Short coir fiber-reinforced natural rubber composites: Effects of fiber length, orientation, and alkali treatment, J. Appl. Polym. Sci. 55 (1995) 583–594. doi:10.1002/app.1995.070550405.

[47] K. Joseph, S. Varghese, G. Kalaprasad, S. Thomas, L. Prasannakumari, P. Koshy, C. Pavithran, Influence of interfacial adhesion on the mechanical properties and fracture behaviour of short sisal fibre reinforced polymer composites, Eur. Polym. J. 32 (1996) 1243–1250. doi:10.1016/S0014-3057(96)00051-1.

[48] K.L. Pickering, M.G.A. Efendy, T.M. Le, A review of recent developments in natural fibre composites and their mechanical performance, Compos. Part A Appl. Sci. Manuf. 83 (2016) 98–112. doi:10.1016/j.compositesa.2015.08.038.

[49] D.U. Shah, Natural fibre composites: Comprehensive Ashby-type materials selection charts, Mater. Des. 62 (2014) 21–31. doi:10.1016/j.matdes.2014.05.002.

[50] B. Alcock, N.O. Cabrera, N.M. Barkoula, J. Loos, T. Peijs, The mechanical properties of unidirectional all-polypropylene composites, Compos. Part A Appl. Sci. Manuf. 37 (2006) 716–726. doi:10.1016/j.compositesa.2005.07.002.

[51] J.L. Thomason, M.A. Vlug, Influence of fibre length and concentration on the properties of glass fibre-reinforced polypropylene: 1. Tensile and flexural modulus, Compos. Part A Appl. Sci. Manuf. 27 (1996) 477–484. doi:10.1016/1359-835X(95)00065-A.

[52] C. González, J. Llorca, Micromechanical modelling of deformation and failure in Ti-6Al-4V/SiC composites, Acta Mater. 49 (2001) 3505–3519. doi:10.1016/S1359-6454(01)00246-4.

[53] C. González, J. LLorca, Mechanical behavior of unidirectional fiber-reinforced polymers under transverse compression: Microscopic mechanisms and modeling, Compos. Sci. Technol. 67 (2007) 2795–2806. doi:10.1016/j.compscitech.2007.02.001.

[54] M.C. Breslin, J. Ringnalda, L. X, M. Fuller, J. Seeger, G.S. Daehn, T. Otani, H.L. Fraser, Processing , microstructure , and properties of co-continuous alumina- aluminum composites, Mater. Sci. Eng. A. 195 (1995) 113–119.

[55] G.S. Daehn, B. Starck, L. Xu, K.F. Elfishawy, J. Ringnalda, H.L. Fraser, Elastic and

plastic behavior of a co-continuous alumina/aluminum composite, Acta Mater. 44 (1996) 249–261. doi:10.1016/1359-6454(95)00138-8.

[56] H.X. Peng, Z. Fan, J.R.G. Evans, Bi-continuous metal matrix composites, Mater. Sci. Eng. A. 303 (2001) 37–45. doi:10.1016/S0921-5093(00)01879-7.

[57] R. Jhaver, H. Tippur, Processing, compression response and finite element modeling of syntactic foam based interpenetrating phase composite (IPC), Mater. Sci. Eng. A. 499 (2009) 507–517. doi:10.1016/j.msea.2008.09.042.

[58] R.J. Moon, M. Tilbrook, M. Hoffman, A. Neubrand, Al-Al_2O_3 composites with interpenetrating network structures: Composite modulus estimation, J. Am. Ceram. Soc. 88 (2005) 666–674. doi:10.1111/j.1551-2916.2005.00115.x.

[59] W. Kreher, W. Pompe, Internal stresses in heterogeneous solids, Akademie-Verlag, 1989. https://books.google.co.uk/books?id=wuJ1AAAAIAAJ.

[60] M.T. Tilbrook, R.J. Moon, M. Hoffman, On the mechanical properties of alumina-epoxy composites with an interpenetrating network structure, Mater. Sci. Eng. A. 393 (2005) 170–178. doi:10.1016/j.msea.2004.10.004.

[61] C. San Marchi, M. Kouzeli, R. Rao, J.A. Lewis, D.C. Dunand, Alumina-aluminum interpenetrating-phase composites with three-dimensional periodic architecture, Scr. Mater. 49 (2003) 861–866. doi:10.1016/S1359-6462(03)00441-X.

[62] Z. Poniznik, V. Salit, M. Basista, D. Gross, Effective elastic properties of interpenetrating phase composites, Comput. Mater. Sci. 44 (2008) 813–820. doi:10.1016/j.commatsci.2008.06.010.

[63] F. Xie, Z. Lu, Z. Yuan, Numerical analysis of elastic and elastoplastic behavior of interpenetrating phase composites, Comput. Mater. Sci. 97 (2015) 94–101. doi:10.1016/j.commatsci.2014.10.021.

[64] D. Manfredi, M. Pavese, S. Biamino, P. Fino, C. Badini, Preparation and properties of NiAl(Si)/Al2O3 co-continuous composites obtained by reactive metal penetration, Compos. Sci. Technol. 69 (2009) 1777–1782. doi:10.1016/j.compscitech.2008.10.012.

[65] O. Al-Ketan, R.K.A. Al-Rub, R. Rowshan, Mechanical Properties of a New Type of Architected Interpenetrating Phase Composite Materials, Adv. Mater. Technol. 2 (2017) 1600235. doi:10.1002/admt.201600235.

[66] O. Al-Ketan, M. Adel Assad, R.K. Abu Al-Rub, Mechanical properties of periodic interpenetrating phase composites with novel architected microstructures, Compos. Struct. 176 (2017) 9–19. doi:10.1016/j.compstruct.2017.05.026.

[67] D.W. Abueidda, R.K. Abu Al-Rub, A.S. Dalaq, D.W. Lee, K.A. Khan, I. Jasiuk, Effective conductivities and elastic moduli of novel foams with triply periodic minimal surfaces, Mech. Mater. 95 (2016) 102–115. doi:10.1016/j.mechmat.2016.01.004.

[68] D.W. Abueidda, A.S. Dalaq, R.K. Abu Al-Rub, H.A. Younes, Finite element predictions of effective multifunctional properties of interpenetrating phase composites with novel triply periodic solid shell architectured reinforcements, Int. J. Mech. Sci. 92 (2015) 80–89. doi:10.1016/j.ijmecsci.2014.12.004.

[69] D.W. Abueidda, R.K. Abu Al-Rub, A.S. Dalaq, H.A. Younes, A.A. Al Ghaferi, T.K. Shah, Electrical conductivity of 3D periodic architectured interpenetrating phase composites with carbon nanostructured-epoxy reinforcements, Compos. Sci. Technol. 118 (2015) 127–134. doi:10.1016/j.compscitech.2015.08.021.

[70] D.W. Abueidda, A.S. Dalaq, R.K. Abu Al-Rub, I. Jasiuk, Micromechanical finite element predictions of a reduced coefficient of thermal expansion for 3D periodic architectured interpenetrating phase composites, Compos. Struct. 133 (2015) 85–97. doi:10.1016/j.compstruct.2015.06.082.

[71] L.H. Sperling, V. Mishra, The Current Status of Interpenetrating Polvrner Networks, Polym. Adv. Technol. 7 (1996) 197–208.

[72] D. Klempner, L.H. Sperling, L.A. Utracki, Interpenetrating Polymer Networks, American Chemical Society, Washington, DC, 1994.

[73] L.H. Sperling, Interpenetrating Polymer Networks and Related Materials, Springer US, 2012. https://books.google.co.uk/books?id=kPzpBwAAQBAJ.

[74] H.X. Zhu, T.X. Fan, D. Zhang, Composite materials with enhanced dimensionless Young's modulus and desired Poisson's ratio, Sci. Rep. 5 (2015) 1–8. doi:10.1038/srep14103.

[75] H. Zhu, T. Fan, C. Xu, D. Zhang, Nano-structured interpenetrating composites with enhanced Young's modulus and desired Poisson's ratio, Compos. Part A Appl. Sci. Manuf. 91 (2016) 195–202. doi:10.1016/j.compositesa.2016.10.006.

[76] H. Zhu, T. Fan, D. Zhang, Composite Materials with Enhanced Conductivities, Adv. Eng. Mater. 18 (2016) 1174–1180. doi:10.1002/adem.201500482.

[77] H. Zhu, T. Fan, Q. Peng, D. Zhang, Giant Thermal Expansion in 2D and 3D Cellular Materials, Adv. Mater. 30 (2018). doi:10.1002/adma.201705048.

[78] A.E.H. Love, A treatise on the mathematical theory of elasticity, Cambridge University Press, 1892.

[79] L.D. Landau and E.M. Lifshitz, Theory Of Elasticity, Pergamon Press, 1970.

[80] K.E. Evans, A. Alderson, Auxetic materials: Functional materials and structures from lateral thinking!, Adv. Mater. 12 (2000) 617–628. doi:10.1002/(SICI)1521-4095(200005)12:9<617::AID-ADMA617>3.0.CO;2-3.

[81] Y. Li, The anisotropic behavior of Poisson's ratio, Young's modulus, and shear modulus in hexagonal materials, Phys. Status Solidi. 38 (1976) 171–175.

[82] Lakes Roderic, Foam Structures with a Negative Poisson ' s Ratio, Science (80-.). 235 (1987) 1038–1040.

[83] R.H. Baughman, J.M. Shacklette, A.A. Zakhidov, S. Stafstrom, Negative Poisson's ratios as a common feature of cubic metals, Nature. 392 (1998) 362–365. doi:10.1006/expr.1996.0064.

[84] J.N. Grima, R. Jackson, A. Alderson, K.E. Evans, Do Zeolites Have Negative Poisson's Ratios?, Adv. Mater. 12 (2000) 1912–1918. doi:10.1002/1521-4095(200012)12:24<1912::AID-ADMA1912>3.0.CO;2-7.

[85] J.N. Grima, R. Gatt, V. Zammit, J.J. Williams, K.E. Evans, A. Alderson, R.I. Walton, Natrolite: A zeolite with negative Poisson's ratios, J. Appl. Phys. 101 (2007) 1–4. doi:10.1063/1.2718879.

[86] A. Yeganeh-haeri, D.J. Weidner, J.B. Parise, A Silicon Dioxide with a Elasticity of α-Cristobalite : Negative Poisson ' s Ratio, Science (80-.). 257 (1992) 650–652.

[87] F. Song, J. Zhou, X. Xu, Y. Xu, Y. Bai, Effect of a negative poisson ratio in the tension of ceramics, Phys. Rev. Lett. 100 (2008) 1–4. doi:10.1103/PhysRevLett.100.245502.

[88] J.W. Jiang, H.S. Park, Negative Poisson's Ratio in Single-Layer Graphene Ribbons, Nano Lett. 16 (2016) 2657–2662. doi:10.1021/acs.nanolett.6b00311.

[89] G. Liu, Q. Zeng, P. Zhu, R. Quhe, P. Lu, Negative Poisson's ratio in monolayer PdSe2, Comput. Mater. Sci. 160 (2019) 309–314. doi:10.1016/j.commatsci.2019.01.024.

[90] C. Zhang, C. Lu, L. Pei, J. Li, R. Wang, K. Tieu, The negative Poisson's ratio and strengthening mechanism of nanolayered graphene/Cu composites, Carbon N. Y. 143 (2018) 125–137. doi:10.1016/j.carbon.2018.10.097.

[91] S. Neelakantan, W. Bosbach, J. Woodhouse, A.E. Markaki, Characterization and deformation response of orthotropic fibre networks with auxetic out-of-plane behaviour, Acta Mater. 66 (2014) 326–339. doi:10.1016/j.actamat.2013.11.020.

[92] R.S. Lakes, K. Elms, Indentability of Conventional and Negative Poisson's Ratio Foams,

J. Compos. Mater. 27 (1993) 1193–1202. doi:10.1177/002199839302701203.

[93] L.L. Hu, M.Z. Zhou, H. Deng, Dynamic indentation of auxetic and non-auxetic honeycombs under large deformation, Compos. Struct. 207 (2019) 323–330. doi:10.1016/j.compstruct.2018.09.066.

[94] W. Liu, J. Huang, X. Deng, Z. Lin, L. Zhang, Crashworthiness analysis of cylindrical tubes filled with conventional and negative Poisson's ratio foams, Thin-Walled Struct. 131 (2018) 297–308. doi:10.1016/j.tws.2018.07.004.

[95] Q. Gao, X. Zhao, C. Wang, L. Wang, Z. Ma, Multi-objective crashworthiness optimization for an auxetic cylindrical structure under axial impact loading, Mater. Des. 143 (2018) 120–130. doi:10.1016/j.matdes.2018.01.063.

[96] J.B. Choi, R.S. Lakes, Fracture toughness of re-entrant foam materials with a negative Poisson's ratio: Experiment and analysis, Int. J. Fract. 80 (1996) 73–83. doi:10.1007/BF00036481.

[97] G.N. Greaves, A.L. Greer, R.S. Lakes, T. Rouxel, Poisson's ratio and modern materials, Nat. Mater. 10 (2011) 823–837. doi:10.1038/nmat3134.

[98] R.S. Lakes, Design considerations for materials with negative Poisson's ratios, J. Mech. Des. 115 (1993) 696–700. doi:10.1115/1.2919256.

[99] R. Lakes, Deformation mechanisms in negative Poisson's ratio materials: structural aspects, J. Mater. Sci. 26 (1991) 2287–2292. doi:10.1007/BF01130170.

[100] A. Alderson, K.L. Alderson, Auxetic materials, Proc. Inst. Mech. Eng. Part G J. Aerosp. Eng. 221 (2007) 565–575. doi:10.1243/09544100JAERO185.

[101] Q. Liu, Literature Review: Materials with Negative Poisson's Ratios and Potential Applications to Aerospace and Defence, 2006.

[102] Z. Wang, H. hu, Auxetic materials and their potential applications in textiles, Text. Res. J. 84 (2014) 1600–1611. doi:10.1177/0040517512449051.

[103] Z. Ge, H. Hu, Innovative three-dimensional fabric structure with negative Poisson's ratio for composite reinforcement, Text. Res. J. 83 (2013) 543–550. doi:10.1177/0040517512454185.

[104] Y. Liu, H. Hu, J.K.C. Lam, S. Liu, Negative Poisson's Ratio Weft-knitted Fabrics, Text. Res. J. 80 (2010) 856–863. doi:10.1177/0040517509349788.

[105] H. Hu, Z. Wang, S. Liu, Development of auxetic fabrics using flat knitting technology, Text. Res. J. 81 (2011) 1493–1502. doi:10.1177/0040517511404594.

[106] G.E. Stavroulakis, Auxetic behaviour: Appearance and engineering applications, Phys. Status Solidi Basic Res. 242 (2005) 710–720. doi:10.1002/pssb.200460388.

[107] Y. Liu, H. Hu, A review on auxetic structures and polymeric materials, Sci. Res. Essays. 5 (2010) 508–511. doi:10.1103/PhysRevLett.98.117601.

[108] H.X. Zhu, N.J. Mills, The in-plane non-linear compression of regular honeycombs, Int. J. Solids Struct. 37 (2000) 1931–1949. doi:10.1016/S0020-7683(98)00324-2.

[109] H.X. Zhu, A.H. Windle, Effects of Cell Irregularity on the Elastic Properties of Open-Cell Foams, Acta Mater. 50 (2002) 1041–1052. doi:DOI: 10.1016/j.ympev.2010.03.012.

[110] H.X. Zhu, S.M. Thorpe, A.H. Windle, The effect of cell irregularity on the high strain compression of 2D Voronoi honeycombs, Int. J. Solids Struct. 43 (2006) 1061–1078. doi:10.1016/j.ijsolstr.2005.05.008.

[111] S. Rawal, Metal-matrix composites for space applications, Jom. 53 (2001) 14–17. doi:10.1007/s11837-001-0139-z.

[112] G.B.V. Kumar, C.S.P. Rao, N. Selvaraj, Mechanical and Tribological Behavior of Particulate Reinforced Aluminum Metal Matrix Composites – a review, J. Miner. Mater. Charact. Eng. 10 (2011) 59–91. doi:10.4236/jmmce.2011.101005.

[113] M. Li, K. Ma, L. Jiang, H. Yang, E.J. Lavernia, L. Zhang, J.M. Schoenung, Synthesis and mechanical behavior of nanostructured Al 5083/n-TiB2 metal matrix composites, Mater. Sci. Eng. A. 656 (2016) 241–248. doi:10.1016/j.msea.2016.01.031.

[114] Y.M. Shabana, B.L. Karihaloo, H.X. Zhu, S. Kulasegaram, Influence of processing defects on the measured properties of Cu-Al 2 O 3 composites: A forensic investigation, Compos. Part A Appl. Sci. Manuf. 46 (2013) 140–146. doi:10.1016/j.compositesa.2012.11.004.

[115] L.J. Huang, L. Geng, H.X. Peng, K. Balasubramaniam, G.S. Wang, Effects of sintering parameters on the microstructure and tensile properties of in situ TiBw/Ti6Al4V composites with a novel network architecture, Mater. Des. 32 (2011) 3347–3353. doi:10.1016/j.matdes.2011.02.023.

[116] E.A. Friis, R.S. Lakes, J.B. Park, Negative Poisson's ratio polymeric and metallic foams, J. Mater. Sci. 23 (1988) 4406–4414. doi:10.1007/BF00551939.

[117] K.E. Evans, B.D. Caddock, Microporous materials with negative Poisson's ratios I: Microstructure and mechanical properties, J. Phys. D. Appl. Phys. 22 (1989) 1877–1882. http://iopscience.iop.org/0022-3727/22/12/012.

[118] J.N. Grima, V. Zammit, R. Gatt, A. Alderson, K.E. Evans, Auxetic behaviour from rotating semi-rigid units, Phys. Status Solidi Basic Res. 244 (2007) 866–882. doi:10.1002/pssb.200572706.

[119] J.N. Grima, L. Oliveri, D. Attard, B. Ellul, R. Gatt, G. Cicala, G. Recca, Hexagonal honeycombs with zero Poisson's ratios and enhanced stiffness, Adv. Eng. Mater. 12 (2010) 855–862. doi:10.1002/adem.201000140.

[120] U.D. Larsen, O. Sigmund, S. Bouwstra, Design and fabrication of compliant micromechanisms and structures with negative Poisson's ratio, J. Microelectromechanical Syst. 6 (1997) 99–106. doi:10.1109/84.585787.

[121] M. Shokri Rad, Y. Prawoto, Z. Ahmad, Analytical solution and finite element approach to the 3D re-entrant structures of auxetic materials, Mech. Mater. 74 (2014) 76–87. doi:10.1016/j.mechmat.2014.03.012.

[122] S. Hengsbach, A.D. Lantada, Direct laser writing of auxetic structures: Present capabilities and challenges, Smart Mater. Struct. 23 (2014). doi:10.1088/0964-1726/23/8/085033.

[123] J.N. Grima, D. Attard, R.N. Cassar, L. Farrugia, L. Trapani, R. Gatt, On the mechanical properties and auxetic potential of various organic networked polymers, Mol. Simul. 34 (2008) 1149–1158. doi:10.1080/08927020802512187.

[124] J.N. Grima, A. Alderson, K.E. Evans, Negative Poisson's Ratios From Rotating Rectangles, Comput. Methods Sci. Technol. 10 (2004) 137–145. doi:10.12921/cmst.2004.10.02.137-145.

[125] J.N. Grima, P.S. Farrugia, R. Gatt, D. Attard, On the auxetic properties of rotating rhombi and parallelograms: A preliminary investigation, Phys. Status Solidi Basic Res. 245 (2008) 521–529. doi:10.1002/pssb.200777705.

[126] J.N. Grima, K.E. Evans, Auxetic behavior from rotating triangles, J. Mater. Sci. 41 (2006) 3193–3196. doi:10.1007/s10853-006-6339-8.

[127] A. Alderson, K.E. Evans, Rotation and dilation deformation mechanisms for auxetic behaviour in the α-cristobalite tetrahedral framework structure, Phys. Chem. Miner. 28 (2001) 711–718. doi:10.1007/s002690100209.

[128] K. Muto, R.W. Bailey, K.J. Mitchell, Nominated Lecture: Special Requirements for the Design of Nuclear Power Stations to Withstand Earthquakes, Proc. Inst. Mech. Eng. 177 (1963) 155–203. doi:10.1243/pime_proc_1963_177_018_02.

[129] K.E. Evans, M.A. Nkansah, I.J. Hutchinson, S.C. Rogers, Molecular network design, Nautre. 353 (1991) 10065.

[130] J.N. Grima, K.E. Evans, Self expanding molecular networks, Chem. Commun. (2000) 1531–1532. doi:10.1039/b004305m.

[131] J.N. Grima, D. Attard, Molecular networks with a near zero Poisson's ratio, Phys. Status Solidi Basic Res. 248 (2011) 111–116. doi:10.1002/pssb.201083979.

[132] J.N. Grima, J.J. Williams, R. Gatt, K.E. Evans, Modelling of auxetic networked polymers built from calix[4]arene building blocks, Mol. Simul. 31 (2005) 907–913. doi:10.1080/08927020500392114.

[133] J.N. Grima, J.J. Williams, K.E. Evans, Networked calix[4]arene polymers with unusual mechanical properties, Chem. Commun. 1 (2005) 4065–4067. doi:10.1039/b505839b.

[134] G.W. Milton, Composite materials with poisson's ratios close to - 1, J. Mech. Phys. Solids. 40 (1992) 1105–1137. doi:10.1016/0022-5096(92)90063-8.

[135] C.P. Chen, R.S. Lakes, Viscoelastic behaviour of composite materials with conventional- or negative-Poisson's-ratio foam as one phase, J. Mater. Sci. 28 (1993) 4288–4298. doi:10.1007/BF01154934.

[136] K.L. Alderson, V.R. Simkins, V.L. Coenen, P.J. Davies, A. Alderson, K.E. Evans, How to make auxetic fibre reinforced composites, Phys. Status Solidi Basic Res. 242 (2005) 509–518. doi:10.1002/pssb.200460371.

[137] S. Jayanty, J. Crowe, L. Berhan, Auxetic fibre networks and their composites, Phys. Status Solidi Basic Res. 248 (2011) 73–81. doi:10.1002/pssb.201083973.

[138] L. Zhou, L. Jiang, H. Hu, Auxetic composites made of 3D textile structure and polyurethane foam, Phys. Status Solidi Basic Res. 253 (2016) 1331–1341. doi:10.1002/pssb.201552768.

[139] Z. Ge, H. Hu, Y. Liu, A finite element analysis of a 3D auxetic textile structure for composite reinforcement, Smart Mater. Struct. 22 (2013). doi:10.1088/0964-1726/22/8/084005.

[140] A.A. Poźniak, K.W. Wojciechowski, J.N. Grima, L. Mizzi, Planar auxeticity from elliptic inclusions, Compos. Part B Eng. 94 (2016) 379–388. doi:10.1016/j.compositesb.2016.03.003.

[141] T.A. Schaedler, W.B. Carter, Architected Cellular Materials, Annu. Rev. Mater. Res. 46 (2016) 187–210. doi:10.1146/annurev-matsci-070115-031624.

[142] J. Schwerdtfeger, P. Heinl, R.F. Singer, C. Körner, Auxetic cellular structures through selective electron-beam melting, Phys. Status Solidi Basic Res. 247 (2010) 269–272. doi:10.1002/pssb.200945513.

[143] A. Lorato, P. Innocenti, F. Scarpa, A. Alderson, K.L. Alderson, K.M. Zied, N. Ravirala, W. Miller, C.W. Smith, K.E. Evans, The transverse elastic properties of chiral honeycombs, Compos. Sci. Technol. 70 (2010) 1057–1063. doi:10.1016/j.compscitech.2009.07.008.

[144] X. Wang, M. Jiang, Z. Zhou, J. Gou, D. Hui, 3D printing of polymer matrix composites: A review and prospective, Compos. Part B Eng. 110 (2017) 442–458. doi:10.1016/j.compositesb.2016.11.034.

[145] T. Fíla, P. Zlámal, O. Jiroušek, J. Falta, P. Koudelka, D. Kytýř, T. Doktor, J. Valach, Impact Testing of Polymer-filled Auxetics Using Split Hopkinson Pressure Bar, Adv. Eng. Mater. 19 (2017) 1–13. doi:10.1002/adem.201700076.

[146] T. Li, Y. Chen, X. Hu, Y. Li, L. Wang, Exploiting negative Poisson's ratio to design 3D-printed composites with enhanced mechanical properties, Mater. Des. 142 (2018) 247–258. doi:10.1016/j.matdes.2018.01.034.

[147] P. Subramani, S. Rana, B. Ghiassi, R. Fangueiro, D. V. Oliveira, P.B. Lourenco, J. Xavier, Development and characterization of novel auxetic structures based on re-entrant hexagon design produced from braided composites, Compos. Part B Eng. 93 (2016)

132–142. doi:10.1016/j.compositesb.2016.02.058.

[148] N. Pan, Z. Sun, Characterizing the structure and geometry of fibrous materials, Therm. Moisture Transp. Fibrous Mater. (2006) 3–41. doi:10.1533/9781845692261.1.3.

[149] L.J.S. Bradbury, The Use of Fibrous Materials in Loudspeaker Enclosures, J. Audio Eng. Soc. 24 (1976) 162–170. http://www.aes.org/e-lib/browse.cfm?elib=2632.

[150] N. Voronina, Improved empirical model of sound propagation through a fibrous material, Appl. Acoust. 48 (1996) 121–132. doi:10.1016/0003-682X(95)00055-E.

[151] L.J. Gibson, M.F. Ashby, Cellular Solids: Structure and Properties, Cambridge University Press, 1999. https://books.google.co.uk/books?id=rzVIBAAAQBAJ.

[152] C. Redenbach, A. Liebscher, Random Tessellations and their Application to the Modelling of Cellular Materials, in: V. Schmidt (Ed.), Stoch. Geom. Spat. Stat. Random Fields Model. Algorithms, Springer International Publishing, Cham, 2015: pp. 73–93. doi:10.1007/978-3-319-10064-7_3.

[153] R. Cowan, Properties of ergodic random mosaic processes, Math. Nachrichten. 97 (1980) 89–102. doi:10.1002/mana.19800970109.

[154] E.N. Gilbert, Random plane networks and needle-shaped crystals, Appl. Undergrad. Math. Eng. (1967).

[155] C. Redenbach, Microstructure models for cellular materials, Comput. Mater. Sci. 44 (2009) 1397–1407. doi:10.1016/j.commatsci.2008.09.018.

[156] J.R.H. and A.H. H.X.Zhu, Windel, Effects of cell irregularity on the elastic properties of open-cell foams, 50 (2016) 1041–1052. doi:10.1016/S1359-6454(00)00282-2.

[157] H.X. Zhu, J.R. Hobdell, A.H. Windle, Effects of cell irregularity on the elastic properties of 2D Voronoi honeycombs, J. Mech. Phys. Solids. 49 (2001) 857–870. doi:10.1016/S0022-5096(00)00046-6.

[158] H.X. Zhu, J.F. Knott, N.J. Mills, Analysis of the elastic properties of open-cell foams with tetrakaidecahedral cells, J. Mech. Phys. Solids. 45 (1997) 319–343. doi:10.1016/S0022-5096(96)00090-7.

[159] C. Chen, T.J. Lu, N.A. Fleck, Effect of imperfections on the yielding of two-dimensional foams, J. Mech. Phys. Solids. 47 (1999) 2235–2272. doi:10.1016/S0022-5096(99)00030-7.

[160] T.F. Zhao, M.Z. Jin, C.Q. Chen, A phenomenological elastoplastic model for porous metal fiber sintered sheets, Mater. Sci. Eng. A. 582 (2013) 188–193. doi:10.1016/j.msea.2013.06.042.

[161] C.M. Van Wyk, 20—Note on the compressibility of wool, J. Text. Inst. Trans. 37 (1946) T285–T292.

[162] H.L. Cox, The elasticity and strength of paper and other fibrous materials, Br. J. Appl. Phys. 3 (1952) 72–79. doi:10.1088/0508-3443/3/3/302.

[163] O. Kallmes, G. Bernier, The Structure of Paper, IV: The Free Fiber Length of a Multiplanar Sheet, Tappi. 46 (1963) 108.

[164] O. Kallmes, H. Corte, The structure of paper, I. The statistical geometry of an ideal two dimensional fiber network, Tappi J. 43 (1960) 737–752.

[165] O. Kallmes Corte, H. and Bernier, G., The structure of paper. Part B: The bonding states of fibers in randomly formed papers, Tappi. 46(8) (1963) 493–502.

[166] O. Kallmes, A comprehensive view of the structure of paper, Theory Des. Wood Fiber Compos. Mater. 3 (1972) 157.

[167] R.S. Seth, Fracture resistance: a failure criterion for paper, Tappi. 58 (1975) 112–117.

[168] R.S. Seth, D.H. Page, The problem of using Page's equation to determine loss in shear

strength of fiber-fiber bonds upon pulp drying, Tappi J. (1996).

[169] D.H. Page, A quantitative theory of the strength of wet webs, J. Pulp Pap. Sci. 19 (1993) J175–J176.

[170] D.H. Page, R.S. Seth, Structure and the Elastic-Modulus of Paper, in: Abstr. Pap. Am. Chem. Soc., AMER CHEMICAL SOC 1155 16TH ST, NW, WASHINGTON, DC 20036, 1980: pp. 27-CELL.

[171] A.K. Mohanty, M. Misra, G. Hinrichsen, Biofibres, biodegradable polymers and biocomposites: An overview, Macromol. Mater. Eng. 276. 277 (2000) 1–24.

[172] C. Sivakandhan, G. Murali, N. Tamiloli, L. Ravikumar, Studies on mechanical properties of sisal and jute fiber hybrid sandwich composite, Mater. Today Proc. (2019). doi:10.1016/j.matpr.2019.06.374.

[173] P. V. Joseph, M.S. Rabello, L.H.C. Mattoso, K. Joseph, S. Thomas, Environmental effects on the degradation behaviour of sisal fibre reinforced polypropylene composites, Compos. Sci. Technol. 62 (2002) 1357–1372. doi:10.1016/S0266-3538(02)00080-5.

[174] S. Chaitanya, I. Singh, J. Il Song, Recyclability analysis of PLA/Sisal fiber biocomposites, Compos. Part B Eng. 173 (2019) 106895. doi:10.1016/j.compositesb.2019.05.106.

[175] K.Y. Lee, P. Bharadia, J.J. Blaker, A. Bismarck, Short sisal fibre reinforced bacterial cellulose polylactide nanocomposites using hairy sisal fibres as reinforcement, Compos. Part A Appl. Sci. Manuf. 43 (2012) 2065–2074. doi:10.1016/j.compositesa.2012.06.013.

[176] P. Ducheyne, E. Aernoudt, P. De Meester, The mechanical behaviour of porous austenitic stainless steel fibre structures, J. Mater. Sci. 13 (1978) 2650–2658. doi:10.1007/BF02402752.

[177] W. Zhou, Y. Tang, M. Pan, X. Wei, J. Xiang, Experimental investigation on uniaxial tensile properties of high-porosity metal fiber sintered sheet, Mater. Sci. Eng. A. 525 (2009) 133–137. doi:10.1016/j.msea.2009.06.025.

[178] M.Z. Jin, C.Q. Chen, T.J. Lu, The mechanical behavior of porous metal fiber sintered sheets, J. Mech. Phys. Solids. 61 (2013) 161–174. doi:10.1016/j.jmps.2012.08.006.

[179] T. Kanit, S. Forest, I. Galliet, V. Mounoury, D. Jeulin, Determination of the size of the representative volume element for random composites: Statistical and numerical approach, Int. J. Solids Struct. 40 (2003) 3647–3679. doi:10.1016/S0020-7683(03)00143-4.

[180] I.M. Gitman, H. Askes, L.J. Sluys, Representative volume: Existence and size determination, Eng. Fract. Mech. 74 (2007) 2518–2534. doi:10.1016/j.engfracmech.2006.12.021.

[181] X.F. Wang, X.W. Wang, G.M. Zhou, C.W. Zhou, Multi-scale analyses of 3D woven composite based on periodicity boundary conditions, J. Compos. Mater. 41 (2007) 1773–1788. doi:10.1177/0021998306069891.

[182] Z. Xia, Y. Zhang, F. Ellyin, A unified periodical boundary conditions for representative volume elements of composites and applications, Int. J. Solids Struct. 40 (2003) 1907–1921. doi:10.1016/S0020-7683(03)00024-6.

[183] Z. Xia, C. Zhou, Q. Yong, X. Wang, On selection of repeated unit cell model and application of unified periodic boundary conditions in micro-mechanical analysis of composites, Int. J. Solids Struct. 43 (2006) 266–278. doi:10.1016/j.ijsolstr.2005.03.055.

[184] M.E.J. Dekkers, D. Heikens, The effect of interfacial adhesion on the tensile behavior of polystyrene–glass-bead composite.pdf, J. Appl. Polym. Sci. 28 (1983) 3809–3815.

[185] C.-E. Rousseau, H. Tippur, Compositionally graded materials with cracks normal to the elastic gradient, Acta Mater. 48 (2000) 4021–4033. doi:10.1016/S1359-6454(00)00202-0.

[186] C. Periasamy, H. V. Tippur, Experimental measurements and numerical modeling of dynamic compression response of an interpenetrating phase composite foam, Mech. Res. Commun. 43 (2012) 57–65. doi:10.1016/j.mechrescom.2012.03.002.

[187] X. Li, Z. Zhang, L. Qin, X. Yang, Z. Feng, Y. Wang, H. Miao, L. He, X. Gong, Measuring Mechanical Properties of the 3D Carbon/Carbon Composite Using Automated Grid Method, J. Test. Eval. 41 (2013) 20120006. doi:10.1520/jte20120006.

[188] T. Parsonage, Beryllium metal matrix composites for aerospace and commercial applications, Mater. Sci. Technol. 16 (2013) 732–738. doi:10.1179/026708300101508522.

[189] F. Song, J. Zhou, X. Xu, Y. Xu, Y. Bai, Effect of a negative poisson ratio in the tension of ceramics, Phys. Rev. Lett. 100 (2008) 1–4. doi:10.1103/PhysRevLett.100.245502.

[190] M.E.J. Dekkers, D. Heikens, The effect of interfacial adhesion on the tensile behavior of polystyrene–glass-bead composites, J. Appl. Polym. Sci. 28 (1983) 3809–3815. doi:10.1002/app.1983.070281220.

[191] W.E. Warren, A.M. Kraynik, The linear elastic properties of open-cell foams, J. Appl. Mech. Trans. ASME. 55 (1988) 341–346. doi:10.1115/1.3173680.

[192] W.E. Warren, A.M. Kraynik, Linear elastic behavior of a low-density kelvin foam with open cells, J. Appl. Mech. Trans. ASME. 64 (1997) 787–794. doi:10.1115/1.2788983.

[193] H.X. Zhu, N.J. Mills, Modelling the creep of open-cell polymer foams, J. Mech. Phys. Solids. 47 (1999) 1437–1457. doi:10.1016/S0022-5096(98)00116-1.

[194] H.X. Zhu, N.J. Mills, J.F. Knott, Analysis of the high strain compression of open-cell foams, J. Mech. Phys. Solids. 45 (1997) 1875–1899. doi:10.1016/S0022-5096(97)00027-6.

[195] S. Yang, A. Tewari, A.M. Gokhale, Modeling of non-uniform spatial arrangement of fibers in a ceramic matrix composite, Acta Mater. 45 (1997) 3059–3069. doi:10.1016/S1359-6454(96)00394-1.

[196] L. Yang, Y. Yan, Z. Ran, Y. Liu, A new method for generating random fibre distributions for fibre reinforced composites, Compos. Sci. Technol. 76 (2013) 14–20. doi:10.1016/j.compscitech.2012.12.001.

[197] S.M. Park, J.H. Lim, M.R. Seong, D. Sohn, Efficient generator of random fiber distribution with diverse volume fractions by random fiber removal, Compos. Part B Eng. 167 (2019) 302–316. doi:10.1016/j.compositesb.2018.12.042.

[198] D. Sohn, Periodic mesh generation and homogenization of inclusion-reinforced composites using an element-carving technique with local mesh refinement, Compos. Struct. 185 (2018) 65–80. doi:10.1016/j.compstruct.2017.10.088.

[199] H. Qing, Automatic generation of 2D micromechanical finite element model of silicon-carbide/aluminum metal matrix composites: Effects of the boundary conditions, Mater. Des. 44 (2013) 446–453. doi:10.1016/j.matdes.2012.08.011.

[200] K.P. Babu, P.M. Mohite, C.S. Upadhyay, Development of an RVE and its stiffness predictions based on mathematical homogenization theory for short fibre composites, Int. J. Solids Struct. 130–131 (2018) 80–104. doi:10.1016/j.ijsolstr.2017.10.011.

[201] Y.H. Ma, H.X. Zhu, B. Su, G.K. Hu, R. Perks, The elasto-plastic behaviour of three-dimensional stochastic fibre networks with cross-linkers, J. Mech. Phys. Solids. 110 (2018) 155–172. doi:10.1016/j.jmps.2017.09.014.

[202] D.H.U. Kochanek, R.H. Bartels, Computer Graphics Volume 18, Number 3 July 1984 Interpolating Splines with Local Tension, Continuity, and, Comput. Graph. (ACM). 18 (1984) 33–41.

[203] M. Faessel, C. Delisée, F. Bos, P. Castéra, 3D modelling of random cellulosic fibrous networks based on X-ray tomography and image analysis, Compos. Sci. Technol. 65

(2005) 1931–1940. doi:10.1016/j.compscitech.2004.12.038.

[204] B. Delaunay, Sur la sph`ere vide. A la m´emoire de Georges Vorono¨, Bull. l'Acad´emie Des Sci. l'URSS. Cl. Des Sci. Math´ematiques Na. (1934) 793–800.

[205] G. Voroni, Nouvelles applications des parametres continus a la theorie des formes quadratiques. Deuxieme Memoire: Recherches sur les parallelloedres primitifs., Nachr. Ges. Wiss. Göttingen, Math.-Physik. Klasse. 2 (1908) 101–120.

[206] M. W. D. Van-Der-Burg, V. Shulmeister, E. Van-Der-Geissen, On the Linear Elastic Properties of Regular and Random Open-Cell Foam Models, J. Cell. Plast. (1997).

[207] S. Deogekar, R.C. Picu, On the strength of random fiber networks, J. Mech. Phys. Solids. 116 (2018) 1–16. doi:10.1016/j.jmps.2018.03.026.

[208] V. Negi, R.C. Picu, Mechanical behavior of cross-linked random fiber networks with inter-fiber adhesion, J. Mech. Phys. Solids. 122 (2019) 418–434. doi:10.1016/j.jmps.2018.09.027.

[209] S.P. Lake, M.F. Hadi, V.K. Lai, V.H. Barocas, Mechanics of a fiber network within a non-fibrillar matrix: Model and comparison with collagen-agarose co-gels, Ann. Biomed. Eng. 40 (2012) 2111–2121. doi:10.1007/s10439-012-0584-6.

[210] L. Zhang, S.P. Lake, V.K. Lai, C.R. Picu, V.H. Barocas, M.S. Shephard, A Coupled Fiber-Matrix Model Demonstrates Highly Inhomogeneous Microstructural Interactions in Soft Tissues Under Tensile Load, J. Biomech. Eng. 135 (2012) 011008. doi:10.1115/1.4023136.

[211] L. Zhang, S.P. Lake, V.H. Barocas, M.S. Shephard, R.C. Picu, Cross-linked fiber network embedded in an elastic matrix, Soft Matter. 9 (2013) 6398–6405. doi:10.1039/c3sm50838b.

[212] G. Li, F. Sharifpour, A. Bahmani, J. Montesano, A new approach to rapidly generate random periodic representative volume elements for microstructural assessment of high volume fraction composites, Mater. Des. 150 (2018) 124–138. doi:10.1016/j.matdes.2018.04.031.

[213] C.B. Barber, D.P. Dobkin, H. Huhdanpaa, The Quickhull Algorithm for Convex Hulls, ACM Trans. Math. Softw. 22 (1996) 469–483. doi:10.1145/235815.235821.

[214] X. Lin, H. Zhu, X. Yuan, Z. Wang, S. Bordas, The elastic properties of composites reinforced by a transversely isotropic random fibre-network, Compos. Struct. 208 (2019) 33–44. doi:10.1016/j.compstruct.2018.09.097.

[215] Z. Lu, Z. Yuan, Q. Liu, 3D numerical simulation for the elastic properties of random fiber composites with a wide range of fiber aspect ratios, Comput. Mater. Sci. 90 (2014) 123–129. doi:10.1016/j.commatsci.2014.04.007.